UNIVERSIDADE DE LISBOA
FACULDADE DE CIÊNCIAS
DEPARTAMENTO DE FÍSICA

Development and Characterisation of Soft Magnetic Iron-Silicon Alloys for Laser Beam Powder Bed Fusion Additive Manufacturing

Francisco Ramos Feliciano

Mestrado em Engenharia Física

Dissertação orientada por:
Profª. Drª. Guiomar Gaspar de Andrade Evans
Dr. Rodolfo Lisboa Batalha

2023

Acknowledgments

I would like to thank every single person that has been with me through this journey, which I can't only define as academic because I've learned so many nice things and met amazing people along the way.

First of all, I want to thank my amazing parents, Aida and Afonso, for their support and help, without them being here wouldn't be possible. In the good and bad moments, they were always there with nice words of courage.

Dr. Rodolfo Batalha, I would like to thank you for all the help during this work, that would not be possible without you and your support and advices along the way.

I also would like to thank Dr. Paulo Morais and all the people from ISQ for receiving me with open arms. It was a pleasure to meet you and work with you, I learned so much and enjoy being with you.

Profª. Drª. Guiomar Evans, thank you for the amazing help and advices through this journey and all the patience.

Profª. Drª. Maria Margarida Cruz, thank you for the support and days "lost" trying to solve measuring problems, that in the end and with your help worked just fine.

Last, but definitely not least, thanks to my family and friends. I can only say the best things about all of them. You were always present and never let me get depressed even in the most challenging times.

Thank you all!

Abstract

With the constant increase of global warming and the electric transition in the transportation industry, improving the efficiency and reducing the power losses of soft magnetic materials is mandatory. This work investigated the Fe-Si alloys production with the additive manufacturing technology Powder Bed Fusion - Laser Beam (PBF-LB). This soft magnetic material has many applications on electric machines. Like all the additive manufacturing techniques, layer-by-layer productions, the PBF-LB is characterised by melting a layer of powder with a laser beam in the desired regions, allowing a big design freedom.

The main objective is to produce samples of Fe-3.5Si and Fe-6.5Si with PBF-LB, optimising the process parameters for each alloy to obtain the highest relative density and less surface roughness. Every built sample is post-processed and prepared for microscopy observation. Several heat treatments are also applied to understand the effects of the stress relief and grain growth on the final properties. The final procedure is the measure of magnetic properties, hardness values and grain size and shape.

The magnetic properties and hardness values measured on Fe-3.5Si alloys indicate a dependence on the production scanning pattern and the posterior heat treatment applied in the samples. Samples with higher relative densities and less surface roughness are observed to reach higher magnetic permeabilities and inductions, and smaller coercivities, leading to fewer hysteresis losses. After a recrystallisation annealing heat treatment, the samples have improved their overall magnetic properties. It is observed that the hardness of the samples decreases with the heat treatments. The Fe-6.5Si alloys reach better magnetic properties than the previous alloy, being crack susceptible due to the formation of ordered phases. It is concluded that Fe-Si alloys produced with additive manufacturing achieve good results, but these materials could have even better magnetic properties (fewer losses and higher efficiencies) by removing the cracks and controlling the microstructure orientation. The changes in the production process or chemical composition of high silicon alloys can help reduce the cracking and reach denser samples.

Keywords

Additive manufacturing; Laser beam powder bed fusion; Soft magnetic materials; Iron-silicon

alloys; Magnetic properties.

Resumo

Com o sucessivo aumento do aquecimento global e com a transição energética observada na indústria dos transportes, novas fontes de energia sustentáveis são cada vez mais uma preocupação, pelo que a utilização de materiais magnéticos poderá ajudar a criar meios de energia ainda mais renováveis e eficientes. Os materiais ferromagnéticos macios têm uma grande importância na indústria elétrica. Estes materiais são conhecidos por conseguirem magnetizar e desmagnetizar de uma maneira mais fácil, no fundo acumulam baixa energia magnética. Um bom material ferromagnético macio é caracterizado por uma permeabilidade magnética elevada e uma coercividade baixa, permitindo atingir induções magnética elevadas, com perdas de potência reduzidas. As curvas de histerese dos materiais ferromagnéticos macios têm uma área bastante inferior aos restantes materiais ferromagnéticos, ajudando a diminuir perdas de potência em elementos de máquinas que utilizam ciclos de magnetização e desmagnetização. Materiais deste tipo podem ser usados em motores, geradores, inversores, conversores, transformadores, sensores, entre outros, visto que necessitam de materiais que não afetem os campos magnéticos variantes induzidos.

A produção deste tipo de materiais através de processos de fabrico aditivo dá-nos uma oportunidade de obter melhores eficiências em máquinas elétricas. As técnicas de fabrico aditivo, conhecidas por construir peças camada a camada permitem a obtenção de peças com uma grande liberdade nos seus desenhos 3D com fatores de preenchimento bastante elevados. A técnica de fusão em camada de pó com feixe laser, conhecida por Powder Bed Fusion - Laser Beam (PBF-LB) ou Selective Laser Melting (SLM) é atualmente a tecnologia mais usada no mundo para metais, sendo a tecnologia também selecionada para este trabalho, uma vez que permite a produção de modelos com qualquer tipo de geometria, sempre com perdas de pó muito reduzidas. Como o nome indica a tecnologia funciona colocando uma cama de pó sobre um substrato do mesmo material e um laser vai realizar um varrimento nas posições do pó que se pretendem fundir. Este processo é sucessivamente repetido, baixando sempre o substrato e preenchendo-se uma nova camada de pó sobre o material fundido. O processo termina quando o conjunto de todas as camadas estão fundidas nas regiões pretendidas e a peça final é obtida.

O trabalho foi desenvolvido no Instituto de Soldadura e Qualidade (ISQ) que possui um elevado conhecimento e experiência na área de fabrico aditivo. A juntar a isto dispõe de diversos equipamentos de processamento por fabrico aditivo (nomeadamente, uma máquina de PBF-LB da marca *Renishaw*), bem como variados equipamentos de pós processamento e de análise de peças produzidas.

Os materials magnéticos macios utilizados neste trabalho foram misturas de ferro e silício, com percentagens de silício de 3.5% e 6.5%. O baixo preço do silício e a sua elevada presença no mercado foram alguns dos fatores na escolha desta mistura. Pretende-se acima de tudo, obter materiais com coercividades bastante reduzidas, levando a perdas de potência mais baixas,

característica necessária para componentes ferromagnéticos de motores elétricos.

A primeira etapa a realizar neste trabalho é a otimização dos parâmetros da tecnologia de fusão em camada de pó com feixe laser para este tipo de materiais. Foram realizados diversos ensaios com a máquina *Renishaw RenAM 500S Flex*. Foram testadas diversas potências e velocidades de varrimento do laser, bem como distâncias entre passagens paralelas consecutivas do laser, para obter os melhores parâmetros que permitem obter peças com densidades relativas perto de 100% e rugosidades pequenas para cada uma das percentagens de silício. Após a obtenção de todos os parâmetros ótimos de produção para cada material, foi variado o padrão de varrimento do laser e o seu incremento angular entre camadas. Foram realizados dois tipos de padrão: *Meander* e *Stripe*. Sendo observado que o padrão em *Stripe* forma uma grande quantidade de poros na zona de junção das tiras de material fundido. Foram também testados três incrementos angulares: 0°, 67° e 90°. É importante notar que após a produção de todas as peças diversos tipos de pós processamentos são aplicados, começando sempre pelo corte da peça, separando-a do substrato usado na produção. A peça final para ficar totalmente pronta a ser analisada necessita de ser polida, facilitando a sua observação no microscópio. As imagens obtidas em microscópio por sua vez são analisadas com *software* apropriado que permite a obtenção do valor de porosidade. A rugosidade das peças também é medida usando um rugosímetro.

Dois tratamentos térmicos foram aplicados nas peças finais: um alívio de tensão e uma recristalização por recozimento, respetivamente, a 700 °C e 1000 °C. O alívio de tensão elimina muita da tensão interna causada pelo processo de impressão que ocorre com gradientes térmicos muito elevados, já a recristalização por recozimento permite o alívio de tensão e um crescimento dos grãos. Diversos testes às peças finais foram realizados com o intuito de medir várias propriedades. A observação das suas durezas foi realizada com indentações, seguindo o método de Vickers. As propriedades magnéticas por sua vez foram medidas com um magnetómetro vibrante, sendo obtida a curva de histerese da peça e todas as características que esta permita medir (coercividade, permeabilidade, indução máxima e perdas de histerese). Foi também realizada difração por raios X em diversas peças e pós para observar as fases geradas. O contraste químico, utilizando nital 2%, em diversas peças permitiu observar por microscopia os grãos formados durante a produção e após a recristalização. Todas estas propriedades foram analisadas tendo em conta as diversas estratégias de varrimento e incrementos angulares usados, sendo efetuada uma comparação entre estes.

Durante a realização do trabalho os dados obtidos apontam para uma grande relação entre as propriedades magnéticas das peças e o seu padrão de fabrico (estratégia de varrimento do laser e o seu incremento angular camada após camada). Diferentes padrões levam a diferentes densidades relativas e grãos formados com tamanhos e formatos diferentes, alterando as suas propriedades magnéticas. Por sua vez, verificou-se que peças com padrões de produção que levam a densidades maiores geram melhores propriedades magnéticas. Para as peças com incrementos angulares de Meander 67° e 90° são obtidas melhores propriedades magnéticas, quando comparado a 0°, que por sua vez gera grãos alongados e de tamanho elevado, dificultando a magnetização. Foi também observado que aplicar tratamentos térmicos nas peças tem o efeito de variar as propriedades magnéticas, bem como as suas durezas. Foi verificado que o tratamento de alívio de tensão piorou as propriedades magnéticas, nomeadamente aumentando as coercividades, tornando o material menos eficiente. Na generalidade é observado um decréscimo de dureza por Vickers com o aumento da temperatura do tratamento térmico. Nas ligas com maior percentagem de

silício apresentam melhores propriedades magnéticas, nomeadamente menos coercividade, mas o seu processo de fabricação é bem mais complicado, devido a fissuras originadas pela criação de fases ordenadas durante o processo de arrefecimento.

Este documento está dividido em quatro grandes capítulos. O primeiro capítulo é uma introdução onde são apresentados os objetivos e motivos da realização deste trabalho, sendo também apresentado o estado da arte do fabrico aditivo, materiais magnéticos macios e técnicas utilizadas para caracterizar as peças produzidas. O segundo capítulo apresenta os procedimentos realizados passo a passo, desde a preparação à impressão de peças, terminando com a metodologia usada na medição de diversas propriedades destas peças. São também apresentados todos os materiais e equipamentos usados para estes procedimentos. O terceiro capítulo foca-se nos resultados obtidos, sendo discutidos e comparados com resultados observados na literatura analisada. As conclusões deste trabalho são apresentadas no quarto capítulo, sendo também apresentado possível trabalho futuro acerca do tema. Em anexo, diversas imagens que não foram possíveis de colocar no texto são apresentadas.

Palavras Chave

Fabrico Aditivo; Fusão em camada de pó com feixe laser; Materiais magnéticos macios; Ligas de ferro silício; Propriedades magnéticas.

List of Contents

1 Introduction **1**
1.1 Motivation . . . 1
1.2 Objectives . . . 1
1.3 Document Organisation . . . 2
1.4 State of Art . . . 2
1.4.1 Additive manufacturing . . . 3
1.4.2 Powder Bed Fusion - Laser Beam . . . 6
1.4.3 Magnetic materials . . . 12
1.4.4 Soft magnetic materials . . . 16
1.4.5 Iron-silicon alloys . . . 16
1.4.6 Electric machines . . . 19

2 Experimental procedure **23**
2.1 Powder characterisation and mixture . . . 23
2.1.1 Powder sieving . . . 23
2.1.2 Microscopy . . . 24
2.1.3 Powder mixtures preparation . . . 26
2.1.4 Flowability . . . 27
2.2 Sample preparation . . . 27
2.2.1 Theoretical Volumetric Energy Density calculations . . . 27
2.2.2 Powder Bed Fusion - Laser Beam machine . . . 31
2.2.3 Preparation of Fe-3.5Si alloy samples . . . 32
2.2.4 Preparation of Fe-6.5Si alloy samples . . . 39
2.3 Sample characterisation . . . 41
2.3.1 Archimedes density measurement . . . 41
2.3.2 Sample etching . . . 42
2.3.3 Optical and electronic microscopy . . . 42
2.3.4 Roughness measurement . . . 43
2.3.5 Hardness test . . . 44
2.3.6 Magnetic Properties . . . 45
2.3.7 X-ray diffraction analysis . . . 49

3 Results and discussion **51**
3.1 Powder analysis . . . 51
3.1.1 Iron powder . . . 51

3.1.2 Silicon powder 52
3.1.3 Fe-3.5Si powder mixture 53
3.1.4 Fe-6.5Si powder mixture 54
3.1.5 Fe-6.5Si pre alloyed powder 55
3.1.6 Powder flowability 55
3.1.7 Boron addition 57
3.1.8 Fe-6.5Si + 0.05B powder mixture 57
3.2 X-ray diffraction analysis 58
3.3 Parameter optimisation 58
3.3.1 Fe-3.5Si alloy 58
3.3.2 Fe-6.5Si alloy 65
3.3.3 Chemical microanalysis with Scanning Electron Microscopy (SEM)-Energy-Dispersive X-Ray Spectroscopy (EDS) 67
3.4 Magnetic properties and hardness 67
3.4.1 Fe-3.5Si alloy 67
3.4.2 Fe-6.5Si alloy 74
3.5 Influence of grain size 76
3.6 Analysis of power losses 77

4 Conclusions **79**
4.1 Future work 80

References **90**

A Appendix A **91**

B Appendix B **97**

C Appendix C **105**

List of Figures

1.1 Steps of an Additive Manufacturing (AM) process, starting from the 3D design until the application, [5]. . . . 3

1.2 Some of metal AM processes available in the market, [5]. . . . 4

1.3 Block diagram of metal AM processes, with classification according to energy source and raw materials, [11]. . . . 5

1.4 Applications and markets for metal AM products, [7]. . . . 5

1.5 Schematic illustration of the powder bed fusion process, [15]. . . . 7

1.6 Powder Bed Fusion (PBF) methods with two different energy sources, laser **(left)** and electron **(right)** beam, [18]. . . . 8

1.7 Some of the parameters possible to be changed in the PBF-Laser Beam (LB) processes, [25]. . . . 9

1.8 **(a)** Schematic with the four main process parameters in PBF-LB, adapted from [17]. **(b)** Melt pool originated by the laser scan, [28]. . . . 10

1.9 Schematic of both welding regimes, conduction welding **(left)** and keyhole welding **(right)**, [31]. . . . 11

1.10 Schematic of several scanning strategies commonly used in PBF-LB. Respectively from left to right, Meander, Chessboard, Stripe and Spiral, [27]. . . . 11

1.11 Schematic hysteresis curve for a ferromagnetic material, representing the magnetisation **M** per magnetic field **H**. Also shown the evolution of the domains through the loop. [47]. . . . 14

1.12 Iron-silicon equilibrium phase diagram with detail of phases with weight percentages of silicon, around 5.5 to 9.5%, [75]. . . . 18

1.13 Unit cell of the $D0_3$ structure, [83]. . . . 19

1.14 **(a)** Full electric car and some of its components, [89]. **(b)** Example of a rotor and stator, [90]. **(c)** Schematic of a rotational electric motor, [91]. . . . 20

2.1 Mixer *RRM MINI II* from *J.Engelsmann AG*. . . . 26

2.2 Granular Material Flowmeter machine from *CREA* present in the laboratory. On the right is shown in detailed the plate with several apertures for the powder to pass through. . . . 28

2.3 **(a)** *Renishaw RenAM 500S Flex* PBF-LB machine. **(b)** Reduced Build Volume (RBV) of the machine. It is noted the powder tank (in orange), the building plate in darker grey at the bottom below the tank and the powder recoater at the top. 32

2.4 **(a)** Powder spreading problem, not reaching the part of the substrate closest to the viewer. **(b)** Several of the first cubes printed in the steel substrate. 33
2.5 Design used for the production done, cube with thin walls. Design given by *Renishaw*. Technical design in Figure A.2 of Appendix A. 34
2.6 3D plot of the laser power, scanning speed and hatch distance for the 13 samples of the Design of Experiment (DOE) for the Fe-3.5Si, with the Volumetric Energy Density (VED) correspondent. 35
2.7 Design used for the production done, boundary piece. Design recommended by Bassoli et al. [23]. Technical design in Figure A.3 of Appendix A. 36
2.8 Three hardness methods existing, with the different indentations, sphere, diamond pyramid and thinner pyramid, named respectively, **(A)** Brinell test, **(B)** Vickers test and **(C)** Knoop test, [120]. 44
2.9 **(Left)** Schematic of a Vibrating Sample Magnetometer (VSM) system with all the components necessary, [124]. **(Right)** Position of the cylinder to be measured in a simplified VSM schematic. 46
2.10 **Top row:** *Model SR830 DSP* lock-in amplifier from *Stanford Research Systems* and *Bruker B-MN C4* power supply, respectively. **Bottom row:** Electromagnet *Magnet B-M6* from *Bruker* and detail of the vibrating sample located in the middle of the electromagnet and pick-up coils, respectively. 47
2.11 Steps to measure the hysteresis losses, measure of several area to achieve the area inside the loop, [126]. 48

3.1 Size distribution of the iron powder, obtained with the sieving process **(left)** and with image analysis of the optical microscope images using *ImageJ* **(right)**. It is presented the relative mass and its cumulative, adding to 100%. 51
3.2 Optical microscope images of the iron powder, at different magnifications, 100× and 500×, respectively, from left to right. 52
3.3 Optical microscope images of the silicon powder, at different magnifications, 200× and 1000×, respectively, from left to right. 52
3.4 Size distribution of the silicon powder, with image analysis of the optical microscope images using *ImageJ*. 53
3.5 SEM microscope Backscattered Electrons (BSE) image of the Fe-3.5Si powder with 600× magnification **(left)** and representative EDS map **(right)** with the position of the iron **(Pink)** and silicon **(Green)** particles. 54
3.6 SEM microscope BSE image of the Fe-6.5Si powder with 100× magnification **(left)** and EDS map **(right)** with the position of the iron **(Pink)** and silicon **(Green)** particles. 54
3.7 Optical microscope images of the Fe-6.5Si m4p powder, at different magnifications, 200× and 1000×, respectively, from left to right. 55
3.8 SEM microscope BSE image of the Fe-6.5Si m4p powder with 100× magnification **(left)** and EDS map **(right)** with the position of the iron **(Pink)** and silicon **(Green)** particles. 56
3.9 Flowability of the Fe-3.5Si and Fe-6.5Si powders, mixture and m4p. The Fe-3.5Si flow rate is measured in three different conditions, with and without heating the powder, at 120°C for 1 hour, and the third case 1 hour after the heating. The Fe-6.5Si flow rates were only measured after the heating in the same conditions. . 56

3.10 SEM microscope BSE image of the Fe-6.5Si m4p + 0.05B powder mixture with 300× magnification **(left)** and EDS map with the position of the iron **(Pink)**, silicon **(Green)** and boron **(Yellow)** particles **(right)**. 57
3.11 X-Ray Diffraction (XRD) of the iron alloys with 3.5% and 6.5% silicon samples. . 58
3.12 Relative density vs VED of the bulk samples of Fe-3.5Si. 59
3.13 Sample with more and less pores in the bulk DOE's done, respectively from left to right. 59
3.14 Border relative density vs Surface Energy Density (SED) of the cube with thin walls and boundary samples form the first and second DOE. 60
3.15 Upskin and wall from the samples that achieve higher relative densities in the borders with two border scans. 60
3.16 Comparison between the bulk material from the Meander 0° sample and Stripe 0° sample, respectively. The dimension of the stripe is presented. 61
3.17 Relative density of the cubes in the building and scanning direction of the several scanning strategies build, Meander 67°, 0° and 90°. 62
3.18 **(a)** Crack density vs VED and **(b)** crack density vs relative density of the Fe-6.5Si samples with different building conditions. 66
3.19 Example of cracks observed in the Fe-6.5Si samples. 67
3.20 Magnetic hysteresis loop of cylinders of Fe-3.5Si alloy produced by PBF-LB with Meander 67° scanning strategy for different thermal-history conditions (as-built, Stress Relief (SR) and Recrystallisation Annealing (RA)). 68
3.21 Vickers hardness map of cubes of Fe-3.5Si alloy produced by PBF-LB with Meander 67° scanning strategy for different thermal-history conditions (as-built, SR and RA). Top row images are in building direction and bottom row images at scanning direction. 69
3.22 Magnetic hysteresis loop of cylinders of Fe-3.5Si alloy produced by PBF-LB with Meander 0° scanning strategy with different thermal-history conditions (as-built, SR and RA). 69
3.23 Vickers hardness map of cubes of Fe-3.5Si alloy produced by PBF-LB with Meander 0° scanning strategy for different thermal-history conditions (as-built, SR and RA). Top row images are in building direction and bottom row images at scanning direction. 70
3.24 Magnetic hysteresis loop of cylinders of Fe-3.5Si alloy produced by PBF-LB with Meander 90° scanning strategy with different thermal-history conditions (as-built, SR and RA). 70
3.25 Vickers hardness map of cubes of Fe-3.5Si alloy produced by PBF-LB with Meander 90° scanning strategy for different thermal-history conditions (as-built, SR and RA). Top row images are in building direction and bottom row images at scanning direction. 71
3.26 Magnetic hysteresis loop of cylinders of Fe-3.5Si alloy produced by PBF-LB with Meander 67°, 0° and 90° scanning strategies divided by thermal-history conditions (as-built, SR and RA). 73
3.27 Hardness Vickers average values of the Fe-3.5Si samples with Meander 67°, 0° and 90°, divided by thermal-history and direction of analysis. 74

3.28 Hysteresis loop of Meander 67° cylinders for Fe-6.5Si using the m4p powder and Fe-6.5Si-0.05B using also the m4p powder joined with boron. 75
3.29 Map of Hardness Vickers of Meander 67° cubes with thin walls for different pieces built, Fe-6.5Si mixture, Fe-6.5Si m4p and Fe-6.5Si-0.05B m4p in the building direction. 76
3.30 Average grain area, given in μm^2, of the etched Fe-3.5Si samples, with all the heat treatments done, measured in the scanning direction. 77
3.31 Hysteresis losses of the Fe-3.5Si samples, obtained from the area of the hysteresis loops. 77

A.1 Technical drawing design of the cube Computer-Aided Design (CAD) designed *SolidWorks*. 92
A.2 Technical drawing design of the cube with thin walls CAD designed *SolidWorks*. 93
A.3 Technical drawing design of the boundary piece CAD designed *SolidWorks*. . . . 94
A.4 Technical drawing design of the cylinder CAD designed *SolidWorks*. 95

B.1 Optical microscope images of the Fe-3.5Si powder, at different magnifications, 200× and 1000×, respectively, from left to right. 97
B.2 EDS map of each element of the powder Fe-3.5Si mixture with the position of the iron **(Pink)** and silicon **(Green)**. 98
B.3 Optical microscope images of the Fe-6.5Si powder mixture, at different magnifications, 200× and 1000×, respectively, from left to right. 98
B.4 SEM microscope BSE **(left)** and Secondary Electrons (SE) **(right)** image of the Fe-6.5Si powder mixture with 300× magnification. 99
B.5 EDS map of each element of the powder Fe-6.5Si mixture with the position of the iron **(Pink)** and silicon **(Green)**. 99
B.6 SEM microscope BSE **(left)** and SE **(right)** image of the Fe-6.5Si m4p powder with 300× magnification. 100
B.7 EDS map of each element of the powder Fe-6.5Si m4p with the position of the iron **(Pink)** and silicon **(Green)**. 100
B.8 Optical microscope images of the boron powder, at different magnifications, 500× and 1000×, respectively, from left to right. 101
B.9 SEM microscope BSE **(left)** and SE **(right)** image of the Fe-6.5Si m4p + 0.05B powder mixture with 300× magnification. 101
B.10 EDS map of each element of the Fe-6.5Si m4p + 0.05B powder mixture with the position of the iron **(Pink)**, silicon **(Green)** and boron **(Yellow)**. 102
B.11 EDS spectrum of the Fe-3.5Si M67 sample, with the percentages of each element considered. 103
B.12 EDS spectrum of the Fe-6.5Si M67 mix sample, with the percentages of each element considered. 103
B.13 EDS spectrum of the Fe-6.5Si M67 m4p sample, with the percentages of each element considered. 104
B.14 EDS spectrum of the Fe-3.5Si M67 sample, with the percentages of each element considered. 104

C.1 Sieve shaker *CISA Cedaceria Industrial 200 N Compact* with the sieves selected for the procedure (63, 45, 38 and 20 μm of grid aperture). 105
C.2 Vacuum oven *Thermo Scientific Vacutherm Vacuum Oven VT 6060 M.* 106
C.3 Equipment used for making epoxy samples. The three liquids observed are the *Buehler* Epoxy Resin, Epoxy Hardener, and Epoxy Release Agent, respectively from the bigger to the smaller recipient. At the right is shown the balance used to weight the liquids in the right proportions. In blue are shown the cups to fill with the epoxy mixture. 106
C.4 Rotating polisher *Buehler EcoMet 30.* 107
C.5 *MetaDi Supreme Crystalline Diamond Suspension* for 6 and 1 μm mats **(left)** and *MasterMet Colloidal Silica Polishing Suspension* **(right)**, both from *Buehler.* 107
C.6 Setup with optical microscope *ZEISS Axiotech 100* and detail from the analysis area with a mounted sample being observed. 108
C.7 Chamber furnace LH 30/14 from *Nabertherm.* Could heat up to 1400°C. 108
C.8 Injector blast cabinet *Normfinish DI12* using glass beads. 109
C.9 Balance used for density measurements, *Kern ABS 220-4N* **(a)**, mass measurement of one sample in air **(b)** and inside water **(c)**, using the same balance. . . . 109
C.10 SEM microscope *JEOL JSM-6500F* and detail from the EDS *Oxford Instruments X-Max*^{N}. 110
C.11 *Struers Labotom-5* cutting machine and detail from the disk and sample holder. . 110
C.12 Mounting machine *SimpliMetTM 4000 Compression Mounting System* from *Buehler.* 111
C.13 *Mitutoyo SJ-210* portable surface roughness tester and detail from the cantilever of the machine doing a calibration process. 111
C.14 Hardness measuring machine *EMCOTEST DuraScan 70 G5.* Possible to measure Hardness Vickers and Brinell. 112
C.15 *EMCOTEST DuraScan 70 G5* indentation with HV **(left)** and optical microscope **(right)**. 112

List of Tables

1.1 Comparison of the general characteristics of the two laser metal AM technologies using powders as raw material, adapted from [13]. 6

1.2 Common Soft Magnetic Materials (SMM) values obtained for several properties. Coercivity H_c, saturation induction B_s, permeability μ and electrical resistivity ρ, adapted from [1, 60]. 16

2.1 Values considered for theoretical Thermal Processability (TP) calculation for both elements, and Fe-3.5Si and Fe-6.5Si mixtures. 29

2.2 Values considered for theoretical VED calculation for both mixtures, Fe-3.5Si and Fe-6.5Si. 31

2.3 Parameters for the first DOE of the Fe-3.5Si alloy. 33

2.4 Values for the DOE of PBF-LB parameters of the bulk of the Fe-3.5Si with 13 samples, printed with cube with thin walls. 34

2.5 Parameters used in the second DOE for the Fe-3.5Si alloy. Presented only the changes from the first production done. Printed with the cube with thin walls. . 35

2.6 Parameters tested for the boundary scans used in the first border DOE, printed with the cube with thin walls and boundary piece. 37

2.7 Parameters used in the second border DOE, printed with the cube with thin walls and boundary piece. 37

2.8 Parameters used in the final Fe-3.5Si production, designed for cubes and cylinders. 38

3.1 Average shape factors of both powders, iron and silicon, obtained using *ImageJ* particle analysis of the higher magnification images from Figure 3.2 and 3.3. . . . 53

3.2 Final parameters optimised to achieve the highest relative density and lowest surface roughness for the Fe-3.5Si alloy using a Meander 67° scanning strategy. . 61

3.3 Surface roughness (R_a, R_q and R_z) measured in samples produced with Meander scanning strategy and different rotation between layers, M67, M0 and M90. . . . 62

3.4 All the etched figures of the M67 Fe-3.5Si samples with all the heat treatments done and presented in building and scanning direction. 63

3.5 All the etched figures of the M0 Fe-3.5Si samples with all the heat treatments done and presented in building and scanning direction. 64

3.6 All the etched figures of the M90 Fe-3.5Si samples with all the heat treatments done and presented in building and scanning direction. 65

3.7 Semi-quantitative EDS analysis of iron, silicon and boron in samples of the Fe-Si alloy. 67
3.8 Magnetic properties of the Fe-3.5Si alloys produced by PBF-LB with the Meander 67°, 0° and 90° scanning strategies. The magnetic parameters are saturation induction B_s, coercivity H_c and relative permeability μ_r. Important physical properties are also presented, such as the relative density ρ_{rel} and average roughness R_a. 71
3.9 Average Vickers hardness of the Fe-3.5Si samples produced with Meander 67°, 0° and 90° in several thermal-history conditions, considering both cross sections. . . 72
3.10 Magnetic properties of the Fe-6.5Si alloys produced by PBF-LB with the Meander 67° scanning strategy. The magnetic properties are saturation induction B_s, coercivity H_c and relative permeability μ_r. Important physical properties are also presented, such as the relative density ρ_{rel} and crack density ρ_{cracks}. 74
3.11 Hardness Vickers values for each of the Fe-6.5Si M67 samples built in the as-built state. 76

Acronyms

AM	Additive Manufacturing
ASTM	American Society for Testing and Materials
BSE	Backscattered Electrons
CAD	Computer-Aided Design
CW	Continuous Wave
DOE	Design of Experiment
EB	Electron Beam
EBM	Electron Beam Melting
EDS	Energy-Dispersive X-Ray Spectroscopy
GOSS	Grain-Oriented Silicon Steel
ISO	International Organization for Standardization
LB	Laser Beam
MW	Modulated Wave
NGOSS	Non-Grain-Oriented Silicon Steel
PBF	Powder Bed Fusion
RA	Recrystallisation Annealing
RBV	Reduced Build Volume
SE	Secondary Electrons
SED	Surface Energy Density
SEM	Scanning Electron Microscopy
SI	Système International
SLM	Selective Laser Melting
SMM	Soft Magnetic Materials
SR	Stress Relief
SQUID	Superconducting Quantum Interference Device
STL	Standard Triangle Language
TP	Thermal Processability

VED	Volumetric Energy Density
VSM	Vibrating Sample Magnetometer
XRD	X-Ray Diffraction

1

Introduction

1.1 Motivation

The principal motivation for this thesis resides in understanding how a soft magnetic material could be enhanced by the recent developments in additive manufacturing and particularly in the powder bed fusion - laser beam technology, which in recent years has emerged as one of the main and more sophisticated additive processes in the market [1]. The soft magnetic materials are present on important parts of electric machines and have a significant impact on society, giving many improvements in the transportation industry, being also important to the ambient [1]. Especially using additive manufacturing processes, soft magnetic materials reach fewer efficiencies and higher power losses when compared with other conventional production techniques, that already have high efficiencies [2,3]. For that reason, many studies are being developed with this type of materials expecting an improvement in the magnetic and physical properties [2]. This work aims to contribute to this discussion by developing materials with better properties for applications in the electric industry.

The Fe-Si alloys are the soft magnetic materials selected for this work because they have the potential to reach higher efficiency with smaller losses when the material is used in an electric machine, besides containing abundant and non-expensive elements such as iron and silicon. Other types of soft magnetics could be used (Fe-Co, Fe-Ni, etc) depending on the application necessary, being especially used for higher frequencies and smaller currents, due to relatively low magnetisations [4].

1.2 Objectives

The main objective of this work is to develop and analyse soft magnetic materials, based on iron and silicon, produced with powder bed fusion - laser beam additive manufacturing. The specific objectives are:

- Understand the concept behind soft magnetic materials and additive manufacturing technologies;
- Design parts suitable for additive manufacturing production and testing;
- Achieve printed parts of Fe-Si alloys without defects, following manipulation of several parameters of powder bed fusion-laser beam production;
- Optimise the post-processing of the produced material to facilitate the posterior analysis;
- Analyse the properties of the printed parts, with a special focus on the main magnetic and physical properties;
- Study the influence that the parameters of the production process and post-treatments applied to the parts have in the final properties;
- Repeat the previous workflow for several compositions of the elements used.

1.3 Document Organisation

This thesis is organised into four chapters. The introduction addresses the state of art of the subject. The next chapter presents the theoretical and experimental approach done in this work, presenting all the materials, techniques and devices used. Then, the results obtained and the discussion is presented in the third chapter. Finally, some conclusions are drawn based on the work done, pointing to possible improvements to be done in the future.

1.4 State of Art

Due to the different topics of this work, the state of the art of metal additive manufacturing and soft magnetic materials is presented. It is also referred some magnetic concepts and theory behind electric machines.

There are many additive manufacturing technologies dedicated to metals, but the focus will be in the powder bed fusion-laser beam process. In addition, soft magnetic materials will also be explained, focusing on the properties that demand improvements to reach even better efficiencies, compared with the machines used nowadays. It will be also mentioned some properties of the iron-silicon alloys used in the work.

1.4.1 Additive manufacturing

Additive Manufacturing (AM) can be defined as a manufacturing technology where the processes are controlled by a computer and consist of joining layer above layer of material to achieve a desired three-dimensional shape defined by a Computer-Aided Design (CAD) model. AM is also sometimes called 3D Printing or Rapid Prototyping by non-specialised media [5, 6].

In the last decades, many improvements have been developed in AM due to high investments and many investigations conducted in this area. All the interest on AM is based on its advantages compared to conventional manufacturing routes, like casting and machining [7]. The additive production technologies can also be defined as "bottom-to-top" methods because the printing starts from a fixed base to deposit the material above. This base is usually from the same material as the object to be produced [8]. Therefore, AM is based on material addition, instead of material removal, to produce the object with the required form and function. With this in mind, the main advantages of the technology are the design freedom (as long as the design is physically possible to print), the short development cycle, leading to fewer production times, and the material reutilisation [5, 9].

The AM process chain can be represented in Figure 1.1, where several steps in the process are observed, from the beginning design to the final object produced and used in an application.

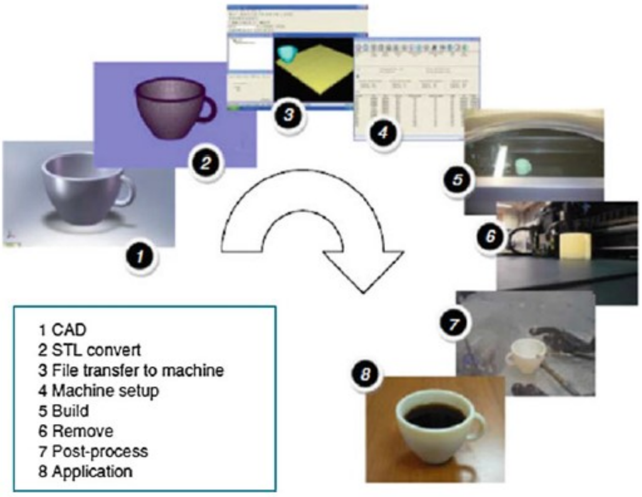

Figure 1.1: Steps of an AM process, starting from the 3D design until the application, [5].

Based on Figure 1.1 it is possible to see that the AM processes begin with a CAD model, which is a 3D design made by a modelling software. This model is usually saved in a Standard Triangle Language (STL) file format, recommended file to represent the geometry through several triangles. Importing the STL file is usually done with a dedicated software from the machine used for the printing. Once the STL file with the design is uploaded to the machine software, the next step is to define the printing parameters, including positioning and orienting the parts and setting process parameters like energy and velocity, between others [5]. With everything set, the building process starts, being this printing process mainly automated and unsupervised, although some errors and defects may occur and regular checking is still advised. Once the production is complete, the part is removed from the machine by the user (non-automated step). After inspecting the produced parts it is normal to apply post-processing operations, like cleaning or support removal [5]. When the part printed achieves the specified characteristics, it is ready to be used in the desired application. At the moment, AM have applications in many sectors of society [7]. But it is also important to mention that AM is not intended to substitute other manufacturing technologies, since some are still more feasible and cheaper in several cases, and that will remain in the future [10].

Classification of metal additive manufacturing processes

There are several types of metal additive manufacturing and the most common classification is based on International Organization for Standardization (ISO) and American Society for Testing and Materials (ASTM) standards. The ISO/ASTM 52900-18 Standard [6] defines the division and definition of all AM techniques, indicating six different types of methods for metal applications (powder bed fusion, direct energy deposition, material extrusion, binder jetting, material jetting and sheet lamination), each one with different divisions. Some specific metal AM production techniques more often used are presented in Figure 1.2, corresponding each to a type of metal AM classified by the standard.

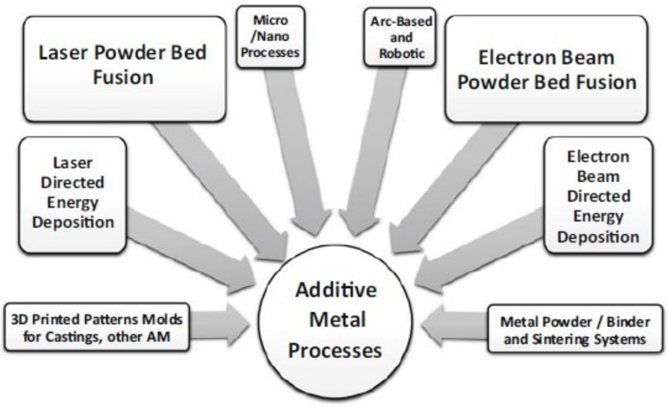

Figure 1.2: Some of metal AM processes available in the market, [5].

The metal AM processes usually require a heat source, a control system with a torch motion that allows the melting of the material and the raw material itself [11]. Figure 1.3 shows a classification of metal AM processes with their respective energy source and raw material.

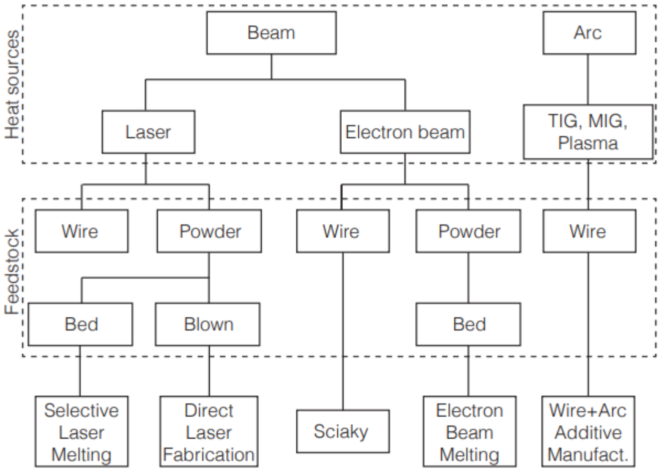

Figure 1.3: Block diagram of metal AM processes, with classification according to energy source and raw materials, [11].

Metal AM products can be found in several applications and many more will appear in the future. Figure 1.4 shows some of the current applications of metal AM, representing the industrial sections that have been adopting the technology.

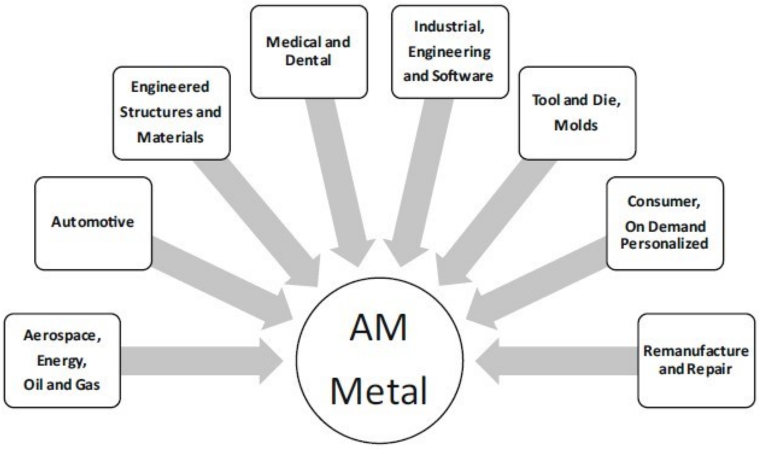

Figure 1.4: Applications and markets for metal AM products, [7].

From the six existing metal AM processes, the most used in the world is the Powder Bed Fusion (PBF) technique. As the name indicates, the process uses a laser or electron beam as the energy source to melt metallic powders, layer-by-layer [6].

Additive manufacturing with laser as energy source

Being one of the most frequently used energy sources in AM, the lasers are still relatively young (62 years [12]) and are still being developed in terms of power, efficiency, beam quality and reliability, apart from the growth and new applications in metal AM systems globally.

As presented in Figure 1.3, laser heating metal AM approaches involve wire or powder as feedstock. Usually, powder feedstock is spread in a thin layer onto a bed and melted by the laser into the desired places. The process is called selective laser melting or powder bed fusion-laser beam. But the powder could also be fed into the laser, melting the particles in the position where the laser-powder intersection occurs, in a process called laser metal deposition or direct energy deposition [13]. Table 1.1 presents a comparison between those two laser melting AM technologies, using powder as raw material.

Table 1.1: Comparison of the general characteristics of the two laser metal AM technologies using powders as raw material, adapted from [13].

	Powder-Fed	**Powder-Bed**
Materials	Large diversity	Limited diversity
Part dimensions	Limited by the handling system	Limited by the building chamber
Part complexity	Limited	Nearly unlimited
Deposition rate	High (10–80 cm^3/h)	Low (2–40 cm^3/h)
Build-up on	3D surface or on existing parts	Flat surface
Roughness	High (60–500 μm)	Low (10–50 μm)
Layer thickness	Thicker layers ($\geq$ 60 μm)	Thinner layers ($\leq$ 60 μm)

Although some advantages are observed for each process, the powder-bed produces parts with better surface finishing and more complex geometries [14]. On the other hand, the powder-bed is significantly slower than the powder-fed process and is limited by the size of the chamber and materials allowed.

1.4.2 Powder Bed Fusion - Laser Beam

From all the AM methods available the one that has been adopted the most lately due to its several advantages, and for that reason is used in this work, is the Powder Bed Fusion (PBF). According to ISO/ASTM 52900-18 [6] the process uses thermal energy to melt a desired region of a powder bed of a desired material. The energy is applied to the powder in the form of a laser or electron beam that scans the powder bed following the 2D cross-section of the model, building the 3D part layer-by-layer from bottom to top [7].

The process (Figure 1.5) occurs on a closed chamber under an inert atmosphere (argon or nitrogen). The powder is dosed and spread with a recoater or roller system that can systematically

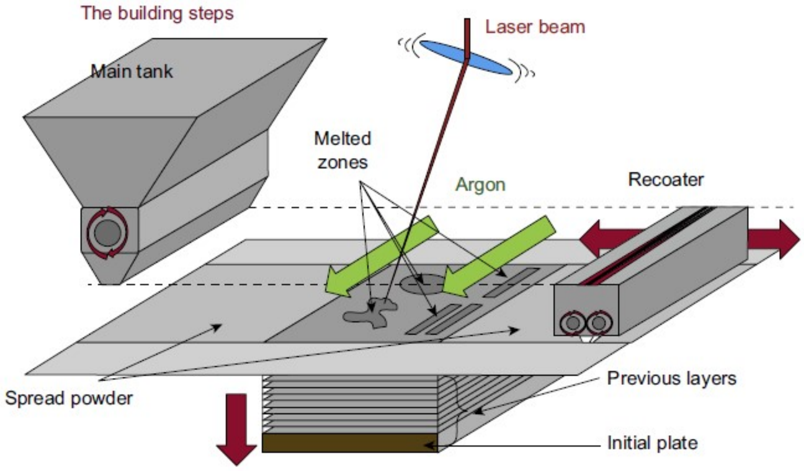

Figure 1.5: Schematic illustration of the powder bed fusion process, [15].

form thin layers of powder, with a desired thickness. The first layer of powder is placed onto a build plate. As the process occurs layer-by-layer, an elevator will lower the part and the next layer is melted above the previous melted layer [7]. Note that during the printing the energy source has enough energy to melt the powder and a part of the previous layer, creating a highly localised melt pool that solidifies very shortly after the melting. Therefore, the PBF process has a very quick melting and solidification cycle. The solidification of the melted material can achieve high cooling rates of 10^6 K/s, due to the high thermal gradients [16].

With PBF, it is possible to manufacture many types of materials, from metals to polymers and ceramics, although the current amount of materials available are still limited [17]. For metals, the melting of the powder feedstock is usually with a Laser Beam (LB) or an Electron Beam (EB), with the technique also being called Selective Laser Melting (SLM) (same as PBF-LB) or Electron Beam Melting (EBM), respectively, depending on which energy source is used. Both methods are represented in Figure 1.6.

Like all AM processes, allow the reutilisation of the powder not melted, reducing material losses. The process enables producing several types of metals as long as they can be supplied as a powder [19]. Some examples that could be used in the PBF-LB are titanium, aluminium, stainless and tool steels, cobalt and nickel super alloys [20]. In addition, it is possible to prepare some combinations of powders to achieve desired properties, as long as the resultant material is weldable [5]. Furthermore, the integration of several pieces of an assembly in one part is also possible, since it can simplify the production and mounting process, joining the fact that it can significantly reduce the weight of the parts [7].

The productivity is inversely proportional to the resolution, which is high in this process because of the thin layers, lowering the productivity [5]. When compared with other AM tech-

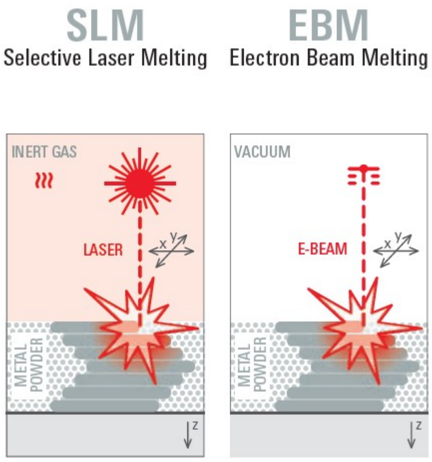

Figure 1.6: PBF methods with two different energy sources, laser **(left)** and electron **(right)** beam, [18].

niques, PBF-LB achieves small roughness (around 10 μm [13]) and a high accuracy. This happens because the melting is caused by a laser beam with a small spot size, that creates small melting pools. With that in consideration the process requires relatively less post-processes than other metal AM technologies [7].

Process parameters of Powder Bed Fusion - Laser Beam

There are many PBF-LB machines in the market, each one with specific operation features. Like in most AM technologies several parameters can be controlled during the 3D process, being possible to adjust the parameters for different geometrical features [17, 21–23]. The process reportedly has more than one hundred parameters that can be controlled, but the most important to consider are the laser power, laser scanning speed, hatching distance, scanning strategy, laser beam focus and layer thickness [24]. Figure 1.7 summarises several of the main PBF-LB process parameters possible to be controlled.

The four main parameters are:

Laser power

The laser, which is the energy source for the powder to melt, could variate its intensity by changing the power P(W). The higher laser power, the greater the energy input in the powder bed, resulting in bigger and deeper melting pools [26].

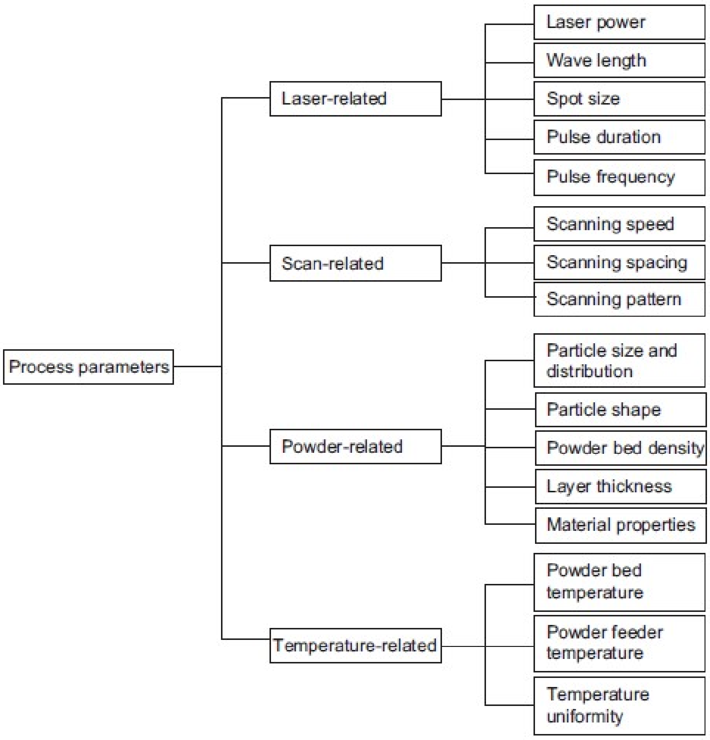

Figure 1.7: Some of the parameters possible to be changed in the PBF-LB processes, [25].

Laser scanning speed

The laser beam scanning speed v(mm/s) passing through the layer of powder is another important parameter to consider. Slowing the laser scan, more time the laser stays to transfer energy to powder particles, increasing the energy input. In PBF-LB the laser can be in continuous or modulated modes where the layer melted in a defined point distance, P_d, and exposure time, E_t, being the melting in pulses to complete a scanning. In another words, the scanning speed is expressed by the ratio between the distance P_d and the time E_t(s) [23]. Usually, two values of E_t are used, 20 and 40 μs, for the Continuous Wave (CW) and Modulated Wave (MW), respectively [27].

Hatching space

Hatch space or distance h(mm), is the distance between the passage of two consecutive laser scans in the powder layer. It is important to optimise this parameter for each material to avoid lack of fusion and pore formation between scanning tracks. It is usually recommended to set the hatch distance with an overlap of one third of the melting pool [27].

Layer thickness

The size selected for the layer of powder is an important factor in the sense that the thickest the layer is, the more energy is required to melt the layer of powder [26]. The layer thickness, L(mm), is inversely proportional to the energy input. If the powder layer is too thick, the melting pool may not join the previous melted layer, resulting in a lack of fusion and production of defects [7].

Figure 1.8 shows the parameters explained above for the PBF-LB process and also the effects that they have on the obtained structure, especially in the melt pool.

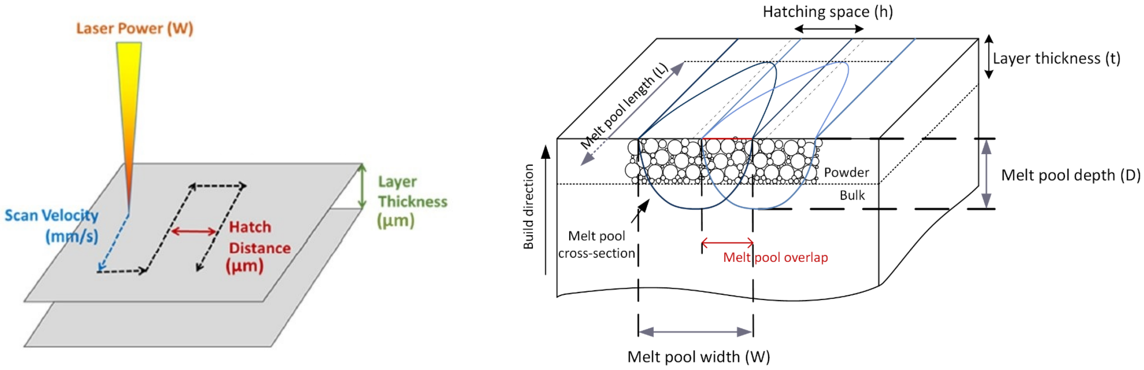

Figure 1.8: **(a)** Schematic with the four main process parameters in PBF-LB, adapted from [17]. **(b)** Melt pool originated by the laser scan, [28].

Other important parameters

Based in all the mentioned parameters, the Volumetric Energy Density (VED) is the energy input per unit of volume of powder [23]. The VED is given in J/mm^3 and is expressed by the equation [29]:

$$VED = \frac{P}{h \cdot v \cdot L} \tag{1.1}$$

In AlMangour et al. [30] it is seen that at lower energy values, the temperature of the melt pool is reduced, increasing the cooling rate. According to the authors, this leads to reduced grain growth and may also induce the formation of large and connected pores that are responsible for cracks and even delamination (separation of the layer printed after solidification). On the other hand, high VED values result in continuous molten scan tracks and high-quality bonding between adjacent layers [23]. But it may also induce high thermal stresses and the appearance of spherical pores because of the vaporisation of the powder feedstock material [31]. In very high VED values, it is observed a switch from conduction welding to keyhole welding, which creates a deeper melting pool and with a keyhole, consequence of the vaporisation, like is observed on the right in Figure 1.9 [31].

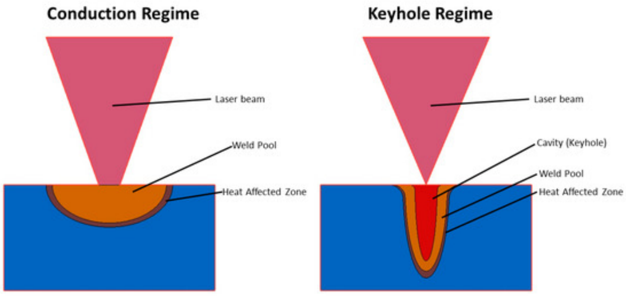

Figure 1.9: Schematic of both welding regimes, conduction welding **(left)** and keyhole welding **(right)**, [31].

Another important parameter responsible for the optimisation of a material in PBF-LB is the scanning pattern or strategy. The scanning strategy describes the pattern that the laser beam will follow in each layer of powder [32]. Depending on the strategy some advantages and disadvantages will appear. Among the most known strategies, the Meander, Stripe and Chessboard are the most used ones, but others like Radial or Spiral have been also reported [33]. Some examples are observed in Figure 1.10.

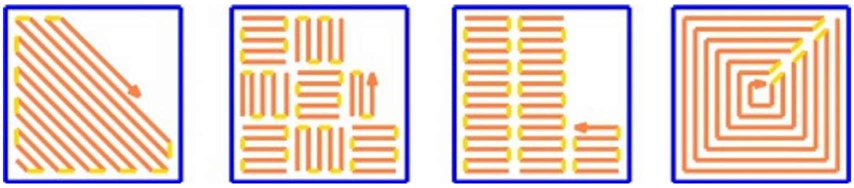

Figure 1.10: Schematic of several scanning strategies commonly used in PBF-LB. Respectively from left to right, Meander, Chessboard, Stripe and Spiral, [27].

When a desired type of scanning strategy is selected, other parameters must be defined, such as the orientation and size of features in the pattern, as well as the angle and angle increment in the pattern [27]. This angle increment is the scan rotation in the pattern of each layer and defines when the laser beam will be melting the spot again. Currently, 67° is considered the best angle increment since it takes 180 layers to rescan the same exact position [27]. On the other hand, 0° means that every layer is going to be scanned identically, without rotation.

The laser beam focus is another parameter that can be changed. The laser focus position affects the melting area and the intensity of the beam, and consequently changes the energy transmitted to the powder [34].

As important as the fabrication process is the material itself. Therefore, this work is focused on soft magnetic materials. In the next sections, a short review of terms and definitions applied to magnetic materials are presented.

1.4.3 Magnetic materials

Magnetic materials are defined as materials that can be affected by external magnetic fields in their surroundings. They are able to be magnetised in the presence of a magnetic field and in the ferromagnetic materials case, in absence of those magnetic fields they remain magnetised [35].

Magnetic field

The magnetic field **H** is responsible for magnetising the materials and the consequent magnetic effects. The field is represented by vectors around magnets, electric currents or changing electric fields [36]. The field intensity can be measured in Newton per Weber or Ampere per meter (A/m), following the Système International (SI).

Magnetic induction or magnetic flux density

Denoted by the symbol **B**, the magnetic induction represents the magnetic flux Φ (number of magnetic lines that pass through a surface of an object) passing a unit of area A, usually denoted by $\mathbf{B} = \Phi/A$ [37]. The units used, in SI, are Weber per square meter (Wb/m^2) or Tesla (T).

Magnetisation

The magnetisation intensity, **M**, is defined as the magnetic moment per unit volume. The magnetic moment depends on the composition of the material and on the orientation and strength of the external magnetic field. Normally, magnetic materials are in the demagnetised state. When an external magnetic field **H** is applied to a metal, they magnetise in different ways and with different intensities. This process of magnetising the material is called magnetisation. The opposite process is the demagnetisation, corresponding to reducing the magnetisation of a material to zero. Magnetisation sometimes is also known as magnet polarisation or vector field that describes the density of the induction caused by a magnetic dipole moment [38].

Magnetic permeability

The magnetic permeability (μ) is defined as the ability of a material to acquire a magnetic moment in an applied magnetic field. For alternate magnetic fields it is related to the degree the magnetic field can penetrate through the material. The higher the permeability, the easier it is for the magnetic field to magnetise an object. For small magnetic fields, the magnetic induction intensity and the intensity of the magnetic field are directly proportional, for an isotropic material, being the relation defined by the permeability, μ [39].

$$\mathbf{B} = \mu \;\; \mathbf{H} \qquad \Leftrightarrow \qquad \mu = \frac{\mathbf{B}}{\mathbf{H}} \tag{1.2}$$

It is possible to see that the ratio allows the calculation of the permeability, in that case, the absolute permeability. This absolute permeability is the product of the permeability in vacuum μ_0 by the relative permeability μ_r of the considered medium [39].

Remanence and Coercivity

When an external magnetic field applied to a magnetic material is removed, the magnetic material will not lose all its magnetisation completely. This remaining magnetisation is called residual magnetism or retentivity or remanence, M_r [40].

To remove completely the remanence, a reverse magnetic field should be applied. Hence the coercivity in a magnetic material is defined as the strength of the magnetic field (H_c) applied reversely which is necessary to completely demagnetise the material, in other words, to set the magnetisation equal to zero [41].

Magnetic domains

A magnetic domain is defined as a region inside a magnetic material where the magnetisation has a defined direction [42]. For a ferromagnetic material, inside each domain, individual magnetic moments of the atoms are aligned together in the same direction. But different domains could have several different directions [43]. Between two different domains of different orientations, the individual atomic dipoles rotate between two orientations, in a region called the domain wall [44].

The domain formation occurs when the ferromagnetic state appears, below a defined temperature called the Curie temperature T_C. Below this temperature, different oriented domains minimise the magnetic energy stored inside the material, while the state with all domains pointing to the same direction will have much higher magnetic energy [43].

Hysteresis curve

Hysteresis curve or loop is the name given to the magnetic cycle of magnetisation and demagnetisation of a defined sample under an applied magnetic field [45]. A plot of the magnetisation **M** versus the magnetic field **H** represents how a specific sample reacts to the field stimulus [46]. An example of a hysteresis curve is shown in Figure 1.11.

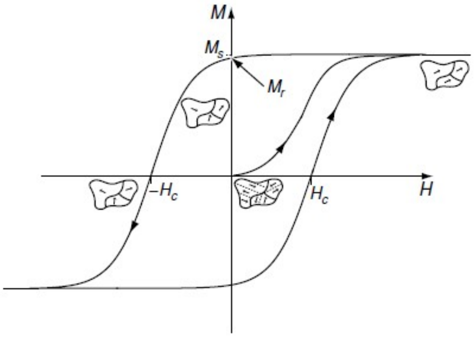

Figure 1.11: Schematic hysteresis curve for a ferromagnetic material, representing the magnetisation **M** per magnetic field **H**. Also shown the evolution of the domains through the loop. [47].

Considering Figure 1.11 it is observed that at the initial state, located in the origin, the material is not magnetised (compensating domain orientations) but the magnetisation **M** appears when a magnetic field **H** is applied. The microstructure of ferromagnetic domains changes until the saturation is reached and all the domains are aligned [47]. The reduction of **H** to zero leads to the remanence M_r. H_c marked in the figure is the reverse field necessary for the magnetisation to become zero. The cycle continues until saturation is reached but with the domains with opposite orientations. Reducing the reverse field and switching the field would originate the same process from one orientation to another, always passing through the remanence and coercivity, being an endless loop, as long as the field is being varied. The Figure 1.11 shows the magnetisation $\mathbf{M(H)}$, but sometimes the induction $\mathbf{B(H)}$ is also used, which are correlated using the Equation:

$$\mathbf{B} = \mu_0(\mathbf{H} + \mathbf{M}) \tag{1.3}$$

The permeability of the material will influence the slope of the curve, the higher the slope in the initial region the easier is to magnetise and achieve higher **M** values.

Types of ferromagnetic materials

Ferromagnetic materials can be divided into two different categories, soft and hard, depending on their capability of magnetise and demagnetise [48–50]. This property depends on the permeability and coercive field. Hard magnetic materials are materials difficult to magnetise and demagnetise, characterised by a large hysteresis loop and a big coercivity (H_c). For that reason, they can retain stored magnetic energy [51].

Unlike hard magnetic materials, soft magnetic materials do not store high magnetic energies, a property confirmed by the high permeability, low coercivity and small hysteresis loop area.

Another difference between hard and soft magnetic materials is in the power losses: soft magnetic materials have smaller losses than the hard magnetic materials, due to the high resistivity. Hard magnetic materials are especially used in speakers and electrical measuring instruments, among others and AM productions are in a very early stage [51, 52]. On the other hand, the main applications for soft magnetic materials are electric motors, generators, transformers, relays, telephone receivers and radars, among others [53].

For soft magnetic materials there are several types of power losses and the major ones are the hysteresis loss (P_h), Eddy current losses (P_e) and residual losses (P_r) [54]. In electric machines, the losses could be associated to heat or sound waves production, reducing the efficiency of the equipment.

Hysteresis losses

Hysteresis loss (P_h) are the losses associated with the hysteresis process, due to the magnetisation and demagnetisation of the material in the alternate magnetic field. These losses are related to the area contained in the hysteresis loop and also depend on the frequency of magnetic field f used, being possible to calculate using the following equation [55]:

$$P_h = f \oint H \, dB \tag{1.4}$$

Eddy current losses

Eddy currents or Foucault's currents, are electrical currents in conductors in the form of closed loops that are created by the variation of the magnetic field in the conductor. Eddy current losses (P_e) are related to these currents and the associated resistive losses are [56]:

$$P_e = \frac{C(Bfd)^2}{\rho} \qquad \text{with} \qquad C = \frac{\pi^2}{6\gamma} \tag{1.5}$$

Where f is the frequency, d the thickness of the material, ρ the specific electric resistivity and γ the density of the material [57]. Increasing the resistivity has the effect of reducing these Eddy currents and its correspondent losses.

Residual losses

The residual losses (P_r) are not too well understood and some different equations are used to characterise this type of losses in the Soft Magnetic Materials (SMM) [58]. They are associated with magnetic relaxations and resonances in the material. Many authors don't consider these type of losses, because as the name says, are residual when compared with the other two loss sources [59]. For that reason, the total core loss of a magnetic material is considered the sum of the hysteresis and Eddy current losses [55].

1.4.4 Soft magnetic materials

The present work is focused on the SMM. There are several SMM, being the most commonly used: iron-silicon, iron-nickel, iron-cobalt, low carbon steels and soft ferrites [50]. A good SMM, especially for electric motors applications, is characterised by the following properties [50,60,61]:

- High magnetic permeability, μ: allows the material to achieve high inductions B at small external magnetic fields H, increasing the efficiency of the machine;
- High saturation magnetisation, M_s: allows the material to achieve high B. A higher B produces higher torque, for the same magnetic conditions and shapes;
- Low magnetic coercivity, H_c: this is mandatory in order to reduce the hysteresis-related losses, which is equal to the area of the B-H hysteresis loop;
- High electrical resistivity, ρ: this is required in order to limit the propagation of the Eddy currents induced by a time-varying B and therefore reduce power losses.

Typical values of these properties are presented in Table 1.2 for some examples of SMM. It is observed that each one has a specific property where is better than the others. Therefore, for different purposes a different alloy should be selected.

Table 1.2: Common SMM values obtained for several properties. Coercivity H_c, saturation induction B_s, permeability μ and electrical resistivity ρ, adapted from [1,60].

	Fe-3.5Si	**Fe-6.5Si**	**Fe-50Ni**	**Fe-50Co**
H_c **(A/M)**	$30-80$	$15-18$	4	40
B_s **(T)**	2.03	1.81	1.6	2.35
μ	1000	1500	$10-10^3$	$15-10^3$
ρ **($\mu\Omega$·cm)**	47	85	48	65

1.4.5 Iron-silicon alloys

Iron, cobalt, nickel and gadolinium are the only elemental ferromagnets at room temperature [62]. Iron and nickel are materials with cubic unit cell and used as soft ferromagnets because of their high symmetry, low magnetic anisotropy and domain restrictions [63]. These properties can be improved by alloying the material with other elements. In this work a SMM alloy with two elements will be made, by mixing them and produced parts in the PBF-LB. Those two elements are iron (Fe) and silicon (Si). In separate, iron and silicon have different properties and react to external conditions in very distinct ways. Magnetically, iron is a ferromagnetic, being very attracted to magnets and their poles [35,64]. On the contrary, silicon is a diamagnetic material [65]. Adding silicon to iron also has the effect of reducing the magnetostriction and magnetic anisotropy [66].

Iron-silicon alloys have the potential to achieve several magnetic properties that enhance the efficiency of motors and other electric machines [67,68]. The aim is to achieve a small hysteresis area, in $B(H)$ behaviour, with low coercivity and high inductions, resulting in lower power losses and higher permeability [69]. This type of materials has several names such as electrical steels or silicon steels, although it is not a steel alloy since there is practically no carbon and manganese in the composition [70]. On the other hand, the lack of these two elements in the Fe-Si alloys reduces the strength and toughness of the material. If the percentage of Si is from 0 to 6.5%, the material is called Electrical Steel, being the usually commercial value around 3.2% of silicon [60]. But if the percentage is from 15 to 90%, it is called ferrosilicon, representing a material much richer in silicon, which is the second element more present in the Earth's crust [71].

The electrical resistivity of iron increases about 5 times with the addition of silicon, resulting in a narrow hysteresis loop and decreasing the Eddy currents on the material. Therefore, when compared to a conventional steel the power losses are about three times lower [72, 73]. The increase of silicon has also the particularity of generating a grain structure that hardens and embrittles the alloy, being more liable to crack formation and, therefore, affecting the workability of the alloy [74]. Using conventional production methods is difficult to produce alloys with silicon content above 4% because of its poor ductility and cracking associated [75].

The production method influences the magnetic properties and the hardness of the SMM, being observed a decrease in coercive and power loss with the annealing temperature [76, 77]. Garibaldi, M. et al. [77] also indicates that with an annealing of 1150 °C the lowest coercivity obtained is 16 A/m with a power loss as low as 2.2 W/kg. Above 900 °C, it is noted a constant increase in resistivity, being reflected in the magnetic properties and losses.

Iron silicon alloys may also be classified in terms of grain structure as Non-Grain-Oriented Silicon Steel (NGOSS) or Grain-Oriented Silicon Steel (GOSS), regarding their domain directions, representing two completely different application sections [66]. Non-oriented Fe-Si alloys have applications in rotating machines while grain-oriented alloys are used in transformers, for example [78]. When preparing the alloys, contaminants are normally present in small concentrations, leading to the formation of carbides, sulfides, oxides and nitrides, with an effect of increasing coercivity and decreasing permeability [79]. Carbon is the element that causes more problems, since it precipitates as carbide and results in higher power loss over time. For this reason, carbon levels are kept below 0.005%. This carbon content is normally achieved with annealing in a controlled reducing atmosphere [60, 80].

Figure 1.12 shows the Fe-Si phase diagram with the temperatures and corresponding composition of the phases of the materials, for all the percentages of each element. For the present work the considering area of the Fe-Si phase diagram is located between 3.5 and 6.5 wt.%Si (weight percentage of silicon).

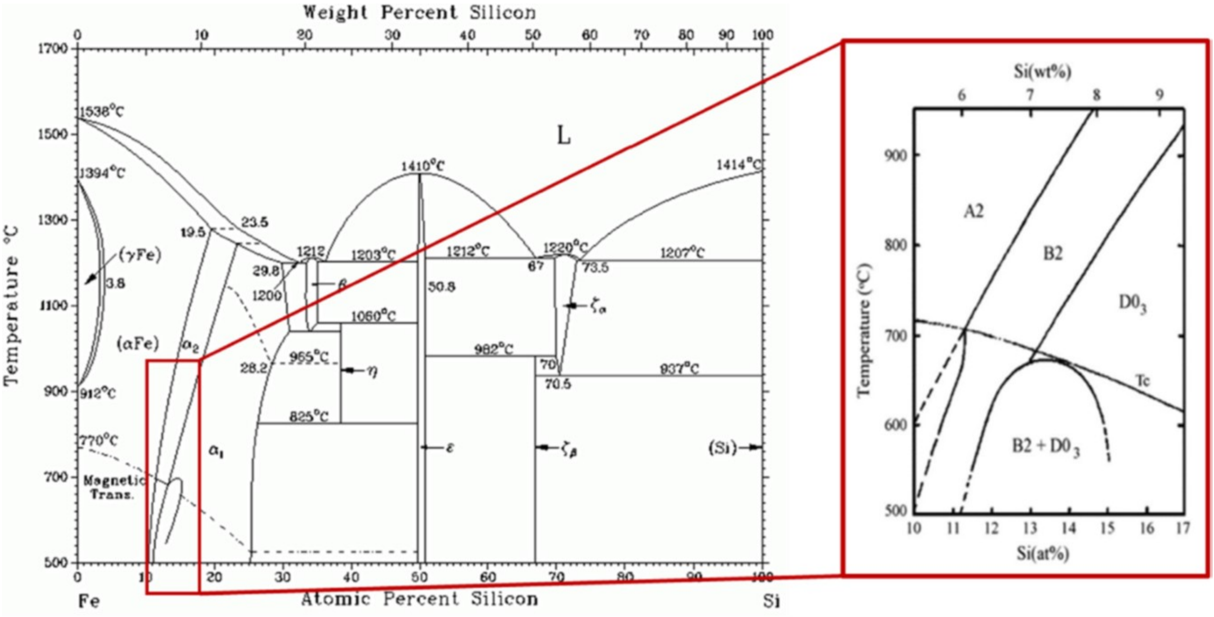

Figure 1.12: Iron-silicon equilibrium phase diagram with detail of phases with weight percentages of silicon, around 5.5 to 9.5%, [75].

From Figure 1.12 it is possible to observe for the two silicon percentages phase formation and also the Curie temperature (in dashed). Considering the 3.5%Si, only one solid phase is formed at room temperature, $\alpha - Fe$ or ferrite, represented also as $A2$ and has a body-centred cube crystal structure (bcc) [81]. With a higher Si percentage of 6.5% different phases are formed: at higher temperatures the disordered ferrite phase is formed but with the cooling two highly ordered phases could occur, α_1 and α_2, also known as $D0_3$ and B_2 (sometimes also called CsCl), respectively [82]. The CsCl structure is similar to the body-centred cubic, but with two elements, and the centred one being different from the other elements in the cell. A two-phase field with B_2 and $D0_3$ appears for lower temperatures, being responsible for low ductility in this alloy [75, 81]. The high tendency for cracking in the Fe-6.5%Si is due to the low ductility of the phase $D0_3$, which is under high tensile stress during production, as induced in PBF-LB due to high thermal gradients [61]. In the $D0_3$ crystal structure, the silicon atoms maximise the distance between them, as shown in Figure 1.13 [83]. This structure is made of bcc- and CsCl-type cells. Random occupancies of dots B and C, or all three sites, lead to CsCl or bcc cells, respectively [84].

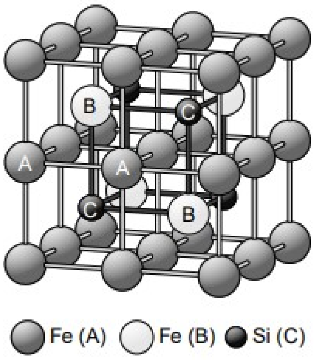

Figure 1.13: Unit cell of the $D0_3$ structure, [83].

1.4.6 Electric machines

Most of the SMM are used in generating electric power devices [61, 67]. For the last decades the generation of electric power has increased with a growth rate of over 7% per year [54]. The range of applications for electrical power is very wide, from huge accelerators to small relays or transformers. Electric and hybrid cars represent a major example of an application of this type of motors, like is possible to see in Figure 1.14 (a), where several components of an electric car are presented. The electric traction motor and the DC/DC converter are the two main elements that use SMM in electric vehicles [85]. On electric motors, SMM usually are used in rotors [86]. Stators are also made of SMM, being the part that surrounds the rotor, both of this parts (Figure 1.14 (b)) are recommended to be soft magnetics to allow an easier magnetisation in different directions [50]. These electric motors can work with DC or AC currents (bigger electric vehicles uses AC), with the following principle: a current in the presence of a field a mechanical force is generated, following the Lorentz Force, $\mathbf{F} = q(\mathbf{E} + v \times \mathbf{B})$, where q is the current charge at a given velocity v, $\mathbf{E}$ the electric field and $\mathbf{B}$ the magnetic field [87]. In the electric motors a rotation is obtained when a magnetic field is applied in the stator by electromagnets and a current is passed through wires or coils around the rotor [88]. Figure 1.14 (c) shows the electric motor principle. It is possible to see that the current is passing in different directions, making the conductor rotate upward next to the north pole (in red) and downward in the south pole (in blue), generating the rotational movement of the wires [91]. Placing more wires around the rotor could help the rotation creating more torque in the motor. It is important to note that after the first rotation for DC motors it is necessary to invert the current, otherwise the Lorentz force

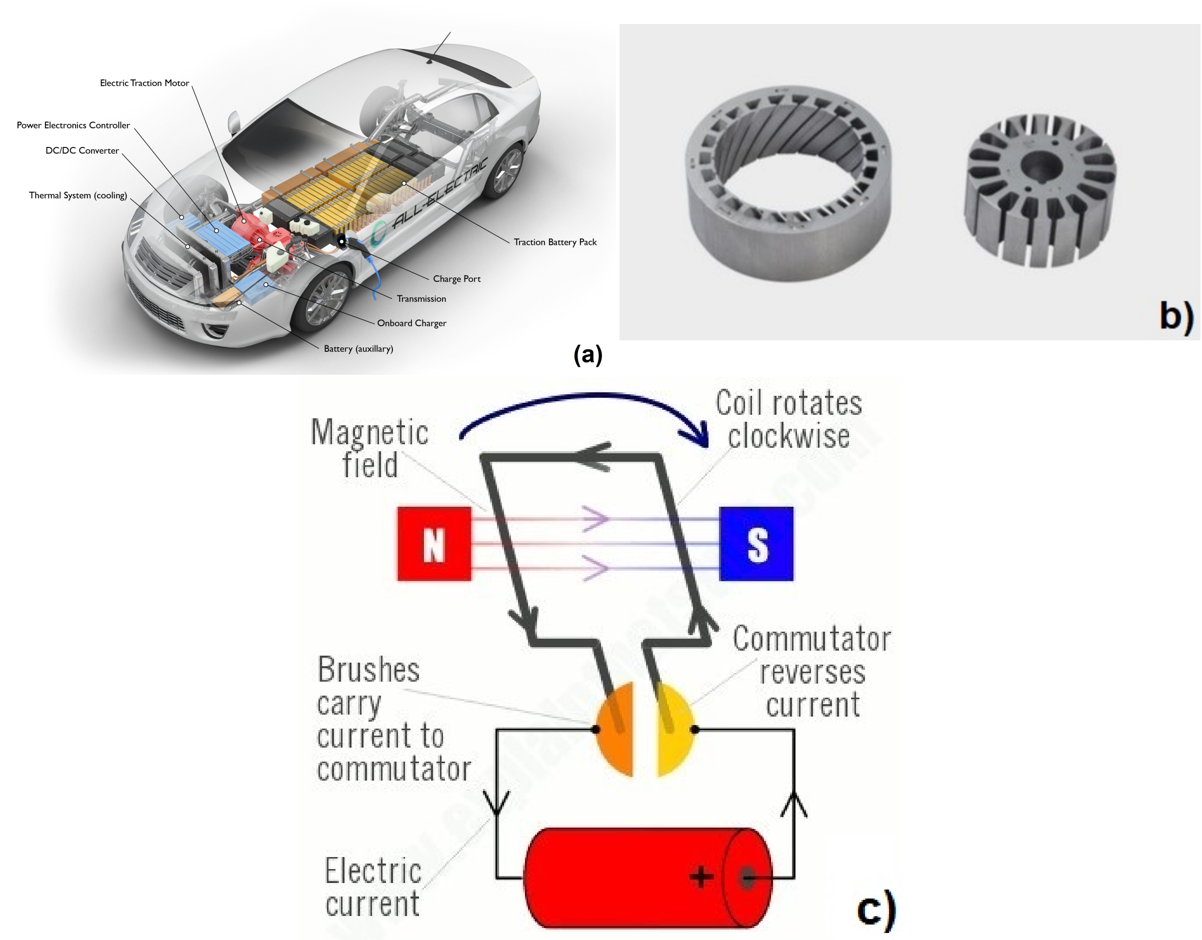

Figure 1.14: **(a)** Full electric car and some of its components, [89]. **(b)** Example of a rotor and stator, [90]. **(c)** Schematic of a rotational electric motor, [91].

would be pointing in the opposite direction and the rotation would stop [88, 91]. AC motors do not require this type of current inversion because the inversion occurs in the electromagnet, as the field is changing from one direction to another at the same speed as the rotation of the rotor [91]. Using SMM in the components of this type of motor has the purpose of quickly adapt their orientation of magnetisation to the field applied, facilitating the movement by not creating opposite polarisations [1, 61].

Additive manufacturing of electric machines

Contrary to the traditional production of SMM, like sheet lamination, AM processes like PBF-LB result in epitaxial grain growth, which could result in enhanced performance of electrical machines, especially because the grains will have a preferred orientation along the building direction, and also randomly shape in the scanning direction, better for rotational machines

[61,78]. Also AM techniques may produce denser infills ratios when compared with conventional techniques, which could help the material to reach higher efficiencies and bigger resistivity, decreasing Eddy currents and the power losses associated [61, 67].

2

Experimental procedure

This chapter will present the process followed to produce the samples, as well as the equipment used and procedures adopted from the powder preparation to the final parts analysis.

2.1 Powder characterisation and mixture

It is important to note that for a PBF-LB process the raw material is in the form of powder. Therefore, analysis of the powder's properties is made. The technique spreads the powder horizontally and the more circular the particles are, the easier it is for the recoater in the machine to spread evenly. The pure iron and pure silicon powders, selected for this work, were supplied by *Sigma-Aldrich*, with the specification of particles with a maximum size of 60 μm and a purity higher than 99%.

2.1.1 Powder sieving

To measure the size of the powder particles present in each element it was used the sieving technique. For sieving, sieves with varying openings are used, basically with the apertures decreasing from the coarser to finer, to let the powder pass through, and a fraction is retained. With all the powder in the top sieve and creating a vibration, in the end the particles will be separated by sieve, which means that they are separated by size. Knowing the weight of the powder in each sieve, it is possible to characterise the particles size distribution. This analysis is done following the ISO/ASTM 52907-19 [92]. The device used for this procedure is a sieve shaker *CISA Cedaceria Industrial 200 N Compact*, presented in Figure C.1. At first, was tested the iron powder with a vibration of 1.5 mm for 15 minutes. The powder in every sieve was then weighted to observe the percentage of powder with the size within the range of the apertures of the sieves. The powder that passed through the last sieve was also weighted. The percentage was calculated by the ratio between the weights measured in each sieve for the sum of all the sieves and passing powder.

The same process was attempted for the silicon powder. After the procedure ended, it was noted that all the powder remained in the top sieve. Looking at some of the characteristics of the silicon, it is seen that silicon is a hydrophilic element, with high tendency to agglomerate. That could be a reason for the powder not to go through the sieves, even in the maximum vibration. One of the ways tried to prevent this was heating the powder in a vacuum oven, *Thermo Scientific Vacutherm Vacuum Oven VT 6060 M* (Figure C.2). The powder was heated for 1 hour at 120 °C to remove as much humidity as possible, having in consideration that 100 °C is the normal boiling point of water. Quickly after the drying process, the sieving was attempted in the same conditions. Although the heating process was done and the vibration in the machine was at the maximum value it was still not possible to measure the particle size, due to the agglomeration.

2.1.2 Microscopy

Optical and electron microscopy have been used in this work. Optical microscope uses light and lenses to obtain a magnified image. Electron microscopy utilises accelerated electrons in vacuum as source of illumination for the sample [93]. An electron could have a wavelength 10^5 times smaller than the wavelength from a photon, so for that reason the Scanning Electron Microscopy (SEM) gives a better resolution and could better represent small objects [94].

A SEM microscope works by focusing a fine electron beam with electromagnetic lenses until they reach the surface of the sample. The result is a magnified image of the interaction captured between the electron beam and the sample. The interaction between the electron beam and the sample creates Secondary Electrons (SE), Backscattered Electrons (BSE) and X-rays. SEM gives 3D black and white topography and element composition of the sample of several sizes. The energies of X-rays identifies the different elements present in the sample. This technology is called Energy-Dispersive X-Ray Spectroscopy (EDS) and it allows semi-quantitative identification of elements present in the samples based on the measured energies. This method is based on the known principle that each element has an unique atomic structure and a defined set of peaks in the electromagnetic emission spectrum [95]. BSE are reflected back after elastic interactions between the electron beam and the sample. In contrast, SE are originated from inelastic interactions. In other words, the BSE give a deeper image inside the sample and SE gives images from the surface region only [93].

Each powder was mounted in epoxy resin and metallography prepared. As well as observing the size and comparing it with the iron powder sieving values obtained before, microscopy allows us to understand other shape properties. The equipments used are presented in Appendix D, Figure C.3. After the epoxy deposition above the powder, located in the bottom of the cup, at least three cycles with vacuum and argon atmosphere are done to remove some air that could be caught in bubbles and the samples are left on air to solidify (around 6 hours). For these cycles is used the transfer chamber of a glove box.

Before optical microscopy analysis, the samples need to be polished, to get no marks or risks on the observation area of the samples. For this process is used the rotating polisher *Buehler EcoMet 30* (Figure C.4). The first process to prepare the samples for the microscope observation is grinding or sanding. It consists in placing the observation area of the sample in the rotational plate with a constant rotation of 300 rotations per minute (rpm). The silicon carbide (SiC) papers used for the grinding are successively decreased in roughness, reducing the size of the scratched observed.

The next step is polishing in polishing cloths with 6, 1 and 0.06 μm abrasive solutions. The plate rotation used for polishing was 150 rpm. Specific abrasives are required for each mat, being used *MetaDi Supreme Crystalline Diamond Suspension* from *Buehler* and Oxide Polishing Suspension (OPS), *Buehler MasterMet Colloidal Silica Polishing Suspension*, all presented in Figure C.5. The polishing is done by placing the sample in the cloths for 5, 3 and 2 minutes, respectively. Every 30 seconds detergent (lubricant) and abrasive suspension is added to the polishing cloths. After polishing, the prepared surface of the samples are cleaned and dried with alcohol. This process is fundamental because the Fe-Si samples oxidise shortly after.

The optical microscope observation was done using the microscope from Figure C.6, which is a *ZEISS Axiotech 100.* Among several optical features and filters the microscope allows five different magnifications, 50×, 100×, 200×, 500× and 1000×. Several pictures were taken, for each magnification, for both powders, observing the shapes and confirming the size values obtained in the sieving.

Image analysis

With the images obtained in the different microscopes, it is possible to do several measurements such as: the aspect ratio, roundness, circularity, solidity and Feret diameters values, could be calculated with a 2D image of separated particles. The Feret diameter is considered the furthest distance between any two parallel tangents of the particle [96]. In the literature, saying Feret diameter is considered the maximum value, but other distances are measured, like the smallest distance. A value that used these measures is the aspect ratio, which is defined as the ratio between the maximum Feret diameter per the minimum one [97]. The roundness and the circularity usually are confused, but in reality both measure different properties. The circularity is defined as the degree in which the particle is similar to a circle with base on the smoothest of the perimeter, the ISO 9276-6 recommends $C = \sqrt{4\pi A/P^2}$ to calculate the circularity C, using the area A and the perimeter P. The roundness is considered the property that analyses if the particle is elongated or not, being very similar to the inverse of aspect ratio. It is possible to calculate the roundness with $4A/\pi Feret^2$ [98]. To end, solidity is the ratio between the area of the particle per the convex area, which is the area that covers all the particle area, being convex. The closer this two areas are the more solid the particle is [96].

The analysis of the images obtained is done with the software *ImageJ*, which could apply thresholds and measure shapes and sizes. This software has an automatic function that measures characteristics explained above, as well as the areas of the particles and features. With those values, several calculations could be done, like the circular equivalent diameter that gives the diameter that a particle would have if it was a sphere, a circle in the image. This value could be calculated using $\sqrt{4 \times Area/\pi}$ only using the area of each particle.

2.1.3 Powder mixtures preparation

The Fe-Si alloys were first prepared from pure iron and silicon powder mixtures with the specific mass properties in drum mixer *RRM MINI II* from *J.Engelsmann AG* (Figure 2.1). The mixing was performed for 30 minutes at 35 rpm, but before the process, the powders were dried in the vacuum oven (Figure C.2) for 1 hour and at 120 °C to prevent agglomeration of silicon particles.

Figure 2.1: Mixer *RRM MINI II* from *J.Engelsmann AG*.

Two different mixtures were prepared, one with 96.5% of iron and 3.5% of silicon, called Fe-3.5Si, and another with 93.5%Fe and 6.5%Si called Fe-6.5Si. Once both mixtures are prepared, optical and electronic microscopy analysis of the powder mixtures can be done in metallographically prepared samples.

2.1.4 Flowability

The flowability test was done in the powder mixtures to observe if the powders can easily spread in the PBF-LB process. This characteristic represents the capability of a powder to flow through small apertures and it is very important to the property of the metallic powder used as feedstock of the PBF-LB process. There are several ways to analyse this property and compare with other materials, such as the Hall flow meter, described in ASTM B213 and ISO 4490. The adopted technique of the present work is described on United States Pharmacopeia number 1174, "Flow Through An Orifice" method. It is similar to the Hall meter, but it measures the mass of powder flowing over time through several standardised apertures. Doing that to several hole sizes and observing the slope of the values of mass along time, it is possible to achieve a curve with the flowability values, depending on the aperture [99]. The mass flow rate of a circular orifice with diameter D is defined by the Beverloo's Law, which is the multiplication of the mean velocity of the powder coming out of the orifice $< v_{out} >$, the bulk density ρ and the aperture area, like seen in the following equation:

$$FlowRate = \rho < v_{out} > \frac{\pi D^2}{4} \tag{2.1}$$

The equipment used can be seen in Figure 2.2. The process consists of placing the powder in the vertical cylinder in a region where the circular plate has no holes underneath. Below the cylinder, a cup is set above the machine balance, which measures the weight of the cup over time. With appropriate software from *GranuTools* is possible to measure the weight in the cup, which varies over time with the powder falling inside. This variation is set by the rotation of the circular plate with several apertures sizes (2, 4, 8, 12, 18, 22 and 28 mm), falling the powder in different grades depending on the aperture, bigger the aperture, bigger the flow rate of the powder.

2.2 Sample preparation

In this section, it will be explained the process followed in the PBF-LB productions.

2.2.1 Theoretical Volumetric Energy Density calculations

Before starting printing with the PBF-LB process an estimation of the theoretical Volumetric Energy Density (VED) was performed, following the methodology presented by Bassoli et al. [23]. It is important to note that because the material used is a mixture of two different elements, obtaining theoretical values for this type of material is difficult, for that reason a weighted

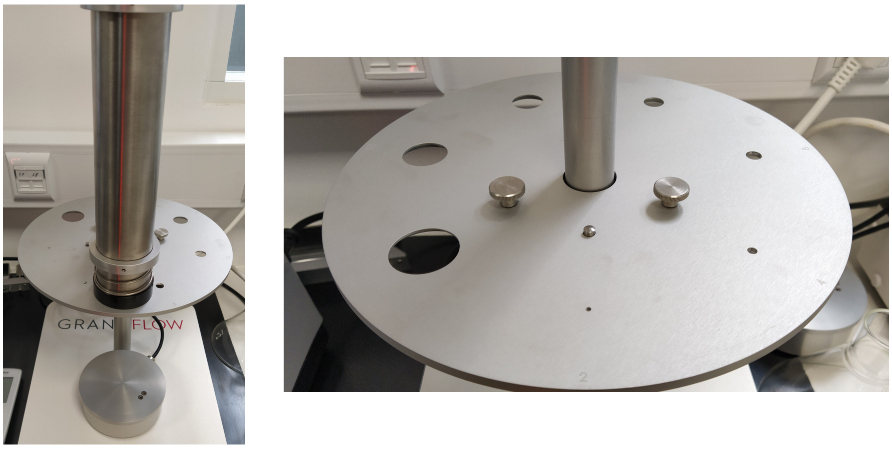

Figure 2.2: Granular Material Flowmeter machine from *CREA* present in the laboratory. On the right is shown in detailed the plate with several apertures for the powder to pass through.

average using the percentages of each element present is used. For example, for the Fe-3.5Si material, the weighted average for the density is: $\rho_{Fe-3.5Si} = 0.965 \times \rho_{Fe} + 0.035 \times \rho_{Si}$. This type of calculation considers the physical properties for the volumetric energy density.

The better range of VED for a PBF-LB production process depends on two basic features of the material:

- The optical properties of the powder feedstock, with a special focus on the reflectivity to the laser beam;
- The thermal properties of the solidified material, especially the thermal conductivity as well as the shrinkage that occurs during the cooling process.

Due to empty spaces between particles in the powder bed, the surface reflectivity R_{powder} of the feedstock can be assumed to be around 70% of the reflectivity R_{bulk} of the corresponding material in his solid bulk form [100]. In some cases, if the laser wavelength is not appropriate for a specific material, in several positions the laser beam could be reflected back, not causing the suitable melting and possibly damaging the equipment if coming back directly to the source.

Thermal processability

The Thermal Processability (TP) of the iron-silicon alloy, given in $\mathrm{Wm^{-1}K^{-1}}$, can be calculated as the ration between the thermal conductivity, k ($\mathrm{Wm^{-1}K^{-1}}$) and the linear shrinkage that the material experiences between the melting and room temperature, in the cooling process. This shrinkage can be estimated by the multiplication of the linear coefficient of the thermal expansion of the solid state material, α ($\mathrm{K^{-1}}$), for the difference between the melting temperature of the material, T_m (K), and room temperature, T_0 (K). Considering $\Delta T = T_m - T_0$, the thermal processability can then be expressed by the following equation:

$$TP = \frac{k}{\alpha \cdot \Delta T} \tag{2.2}$$

Bassoli et al [23] recommends T_0 to be 20 °C ≈ 293 K. TP is used as a preliminary evaluation for the processing of these new materials by PBF-LB, because the process depends on other relevant properties, like weldability. It is seen that if the thermal conductivity is low, the melted state of the metal will remain for more time. Also, if the shrinkage is high, several deformations or even cracks are likely to occur, thus causing job failure in the process [101]. Concluding, for high values of TP, the material will be considered easily printable from a thermal point of view.

For both Fe-Si alloys the theoretical values of TP obtained, using the values of Table 2.1, were 4528 and 4847 $\mathrm{Wm^{-1}K^{-1}}$, for Fe-3.5Si and Fe-6.5Si, respectively. These values are considered high, being considered easy alloys to process thermally with PBF-LB.

Table 2.1: Values considered for theoretical TP calculation for both elements, and Fe-3.5Si and Fe-6.5Si mixtures.

Property	Iron	Silicon	Fe-3.5Si	Fe-6.5Si
T_m (K) [Figure 1.12 [102]]	1538	1414	1778	1728
k ($\mathrm{Wm^{-1}K^{-1}}$) [102]	78.2	138.5	80.3	82.1
α ($\mathrm{K^{-1}}$) [102]	12.0×10^{-6}	4.0×10^{-6}	11.9×10^{-6}	11.8×10^{-6}

Primary bulk parameters

To achieve the parameters to get the best bulk properties, the main strategy is to evaluate the VED necessary to melt the material. Bassoli et al. [23] indicate an estimation of the VED that must be provided for consolidation through melting and subsequent solidification mechanisms can be based on the heat per unit volume, q ($\mathrm{Jmm^{-3}}$). This is calculated using the following equation:

$$q = [c \cdot \Delta T + l_f]\rho \tag{2.3}$$

Where c ($\mathrm{Jkg^{-1}K^{-1}}$), l_f ($\mathrm{Jkg^{-1}}$) and ρ ($\mathrm{kgmm^{-3}}$) are the specific heat capacity, specific latent heat of fusion and density of the material, respectively. The VED is proportional to q, being the relation given by the inverse of an efficiency coefficient η, which represents some dissipative events in the PBF-LB [103–107]. Those dissipative events include losses from the powder's reflectivity, the cooling of the melting pools, a result of the heat spread through the powder bed, due to the heat conduction and additional losses. The efficiency η in this process could be represented with the multiplication of these three factors, therefore the VED is obtained using the equation:

$$VED = \frac{q}{\eta} = \frac{q}{(1 - R_{powder}) \cdot (1 - k_{rel}) \cdot \eta^*} \tag{2.4}$$

Where R_{powder} is the reflectivity of the powder used, is estimated that this reflectivity is 70% of the metal reflectivity. k_{rel} is the relative thermal conductivity and η^* is the additional efficiency factor. Bassoli et al. [23] recommend this value to be assumed as around 20%. Observing Equation 2.4 is seen that the denominator, η, has three terms, the first represent an attempt to estimate the losses due to reflection, the second the losses from the thermal conduction and the third, η^*, the losses from the complex dissipative effects happening inside the melting pools. It is important to note that the two first efficiency terms of η are assumed for an ideal PBF-LB process, ignoring possible interferences, like melt pool splatters or dust interferences in the laser path. If this happens several effects could be occurring in the laser behaviour, like power attenuation or slight change in the laser beam focus [108]. Even if they are unwanted some additional losses will occur due to this. The relative thermal conductivity of the powder k_{rel} is calculated with the fraction between the thermal conductivity of the powdered feedstock and of the pure silver, $k_{rel} = \frac{k_{powder}}{k_{Ag}}$, considering k_{Ag} equal to 425 $\mathrm{Wm^{-1}K^{-1}}$. The k_{powder} value could be approximately calculated with a classical rule of mixtures [109] assuming the volume fraction of powder is 50% of the layer of powder, as seen in the next equation:

$$k_{powder} = k_{metal} \cdot V_{metal} + k_{gas} \cdot (1 - V_{metal}) = 0.5 \cdot (k_{metal} + k_{gas}) \approx 0.5 \cdot k_{metal} \tag{2.5}$$

Being the k_{metal} the thermal conductivity of the bulk material and k_{gas} the thermal conductivity of the gas present in the build chamber. Due to the layer-by-layer scanning the melting will happen in a powder part as well as the previous solidified layer, for that reason, two different models should be considered to represent the effects of the thermal conduction [110]. Mainly because we are looking for a first approximation, only the thermal conductivity in the powder will be considered, simplifying a lot the model and still giving results close to reality, due to the solidified area remelted being significantly smaller than the powder layer. With this in consideration, the main equation for the VED calculations is $VED = P/(h \cdot v \cdot L)$ (Equation 1.1 from the previous chapter), instead of the theoretical VED from Equation 2.4, which is only used here to achieve a theoretical range estimation of energy. The values used for this theoretical VED calculation for both mixtures are observed in Table 2.2. Considering the values of Table 2.2 is possible to achieve the values for the theoretical VED of 71.64 $\mathrm{J/mm^3}$ for the Fe-3.5Si and 71.94 $\mathrm{J/mm^3}$ for Fe-6.5Si.

Table 2.2: Values considered for theoretical VED calculation for both mixtures, Fe-3.5Si and Fe-6.5Si.

Property	**Iron**	**Silicon**	**Fe-3.5Si**	**Fe-6.5Si**
ρ (kgmm^{-3}) [102]	7.87×10^{-6}	2.33×10^{-6}	7.68×10^{-6}	7.51×10^{-6}
c (Jkg^{-1}K^{-1}) [102]	456	729	465.55	473.75
l_f (Jkg^{-1}) [102]	247×10^3	1787×10^3	300.9×10^3	347.1×10^3
R (at 1000 nm) [111, 112]	0.6	0.3	0.59	0.58

A Design of Experiment (DOE) is a way used to test and evaluate a set of parameters, usually to observe which are the most suitable or significant to achieve the best parameters from VED, from Equation 1.1 and obtain highest relative density and border surface finishing quality. It is recommended to keep every energy value within 30% of the theoretical VED calculated, being considered this value the medium point. Approximately every piece printed should have a VED between 50 and 94 J/mm^3. A common theme in PBF-LB energy DOE's is fixing a parameter from Equation 1.1, being selected for that purpose the layer thickness L, being choosed $L = 30$ μm. Usually this value is bigger, around 40 or 60 μm but the used powder size is relatively small compared with other PBF-LB powders. Considering the size of the layer fixed, the remaining three parameters are undefined, the power, speed and hatch, and several DOE's will be done to observe the best value for each parameter. The geometry selected for the first DOE productions, recommended by Bassoli et al. [23], is a bulk cube $10 \times 10 \times 10$ mm^3. The design drawing is present in Figure A.1 from Appendix A. Note that the height of the cube is higher than 10 mm (15 mm) to compensate the substrate cut. The size is ideal for mounting in resin, facilitating the polishing, being a bulk material with no thin features helps the observation.

2.2.2 Powder Bed Fusion - Laser Beam machine

The PBF-LB machine used in this work is a *Renishaw RenAM 500S Flex* (Figure 2.3 (a)), with 500 W ytterbium fiber laser ($\lambda = 1070$ nm) in continuous or modulated laser mode and a spot size of 80 μm with dynamic laser focusing. The machine has a building volume of $250 \times 250 \times 350$ mm^3 and works under an argon atmosphere. The maximum build rate is 150 cm^3/h and the layer thickness may be varied from 20 to 100 μm. The maximum scanning speed is 10 m/s. It has a total loss powder management system, which allows an easy change of materials. Besides the standard building, there is also the possibility to use the Reduced Build Volume (RBV), which allows producing smaller builds, with a maximum build volume of $78 \times 78 \times 50$ mm^3. The RBV, seen in Figure 2.3 (b), is a tool mainly used to help testing new materials and machine parameters. The RBV enables users to quickly change over between different materials, as all powder is contained within the RBV unit. Once satisfactory results

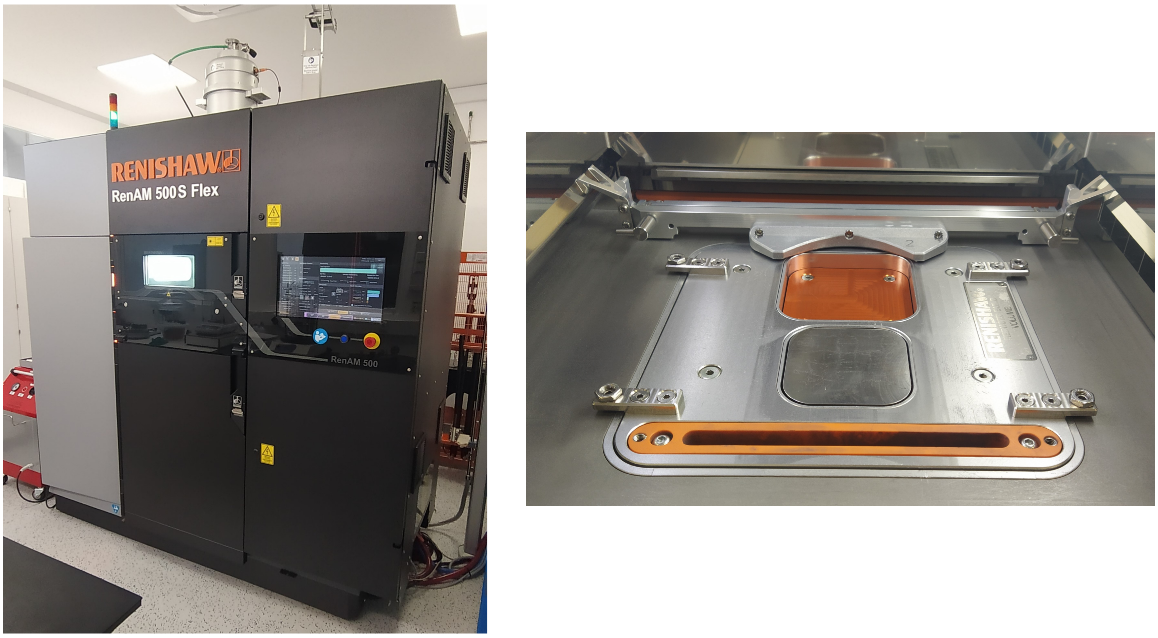

Figure 2.3: **(a)** *Renishaw RenAM 500S Flex* PBF-LB machine. **(b)** Reduced Build Volume (RBV) of the machine. It is noted the powder tank (in orange), the building plate in darker grey at the bottom below the tank and the powder recoater at the top.

have been achieved, the parameter sets can be further developed using the full machine build volume, allowing bigger productions. This smaller build volume uses significantly less material compared to a standard build volume and reduces the time taken to prepare and remove the build. A key benefit of the RBV is the ability to utilise the *RenAM 500S Flex* system further, by being able to complete builds with as little as 0.25 litres of powder, whilst not contaminating its primary powder system. In this work, mainly because of small powder stock at disposition, will only be used the RBV. This decision will help with the production times and pieces removal.

2.2.3 Preparation of Fe-3.5Si alloy samples

The first material studied is the Fe-3.5Si, being done several DOE's, to achieve optimal parameters for the bulk and boundaries. The first DOE's were done with the help of the software *Minitab*, which could define the best positions for the parameter values, spreading them and experimenting a bigger area of energy. But the first production instead of being done with the software was tested using an empirical approach, testing parameters that would fit the theoretical energy range calculated before. It was done a cube DOE of 3^3, which means that was selected three values for a parameter and this value is combined with every value from the other parameters, with all the combinations. The values used were the ones observed in Table 2.3. Knowing that the thickness of the layer will be the fixed parameter the other parameter were

Table 2.3: Parameters for the first DOE of the Fe-3.5Si alloy.

Parameter	Value
Layer thickness	30 μm
Laser power	250 – 300 – 350 W
Laser scanning speed	750 – 1000 – 1250 mm/s
Hatch distance	0.112 – 0.124 – 0.136 mm
Scanning strategy	Meander 67°

tested with every other, for example, one piece was printed with the laser at 300 W, 1000 mm/s and 0.136 mm of hatch. Giving a total of 27 pieces each one with different parameters and, consequently, energy.

It is important to note that substrates with the same chemical composition as the Fe-3.5Si were not available, being used steel substrates that have similar compositions and properties. It is also observed that many of the samples could not be built during one production, that happens because the recoater of the machine could not spread the powder over all the scanning area above the substrate, like is observed in Figure 2.4 (a). This problem only allows the production to be 100% guaranteed successful in the top part of the substrate, like seen in Figure 2.4 (b) with the correct parts only at the top. More prints and substrates than expected have to be used to build all of the 27 pieces. For that reason, from now on the DOE's will be done to 13 samples of different VED values, being choose 3 values for each parameter to vary between those 13 samples. This selection is done with *Minitab*, on which is only asked to combine the values for a wider standard deviation of VED values. With the number of samples reduction, the DOE's done is shorter, reducing the number of prints.

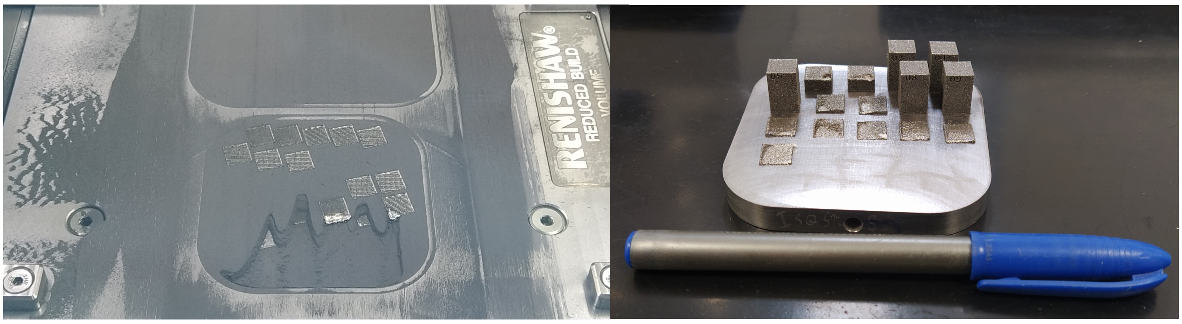

Figure 2.4: **(a)** Powder spreading problem, not reaching the part of the substrate closest to the viewer. **(b)** Several of the first cubes printed in the steel substrate.

Bulk development

It was seen that a DOE with 27 samples would take a lot to produce and analyse. A different approach was followed, one using fewer pieces for each DOE. 13 samples with several combinations of the parameters were processed. Like in the previous DOE's, three values for each main parameter were selected using the *Minitab* software.

Another change made was in the geometry used for the prints, instead of a bulk cube, a cube with thin walls of different sizes was selected, allowing the prints to have different scanning areas in the powder. The geometry has a bulk part in the bottom, similar to the previous cube, but the smaller scanning areas of the walls could help assess the parameters for producing smaller objects. The geometry is shown in Figure 2.5 (A.2 from Appendix A). Considering the best parameters the ones who create a higher relative density and smaller porosity, in another words, the parameters who create a better bulk material. The analysis of the pieces is based on measuring the density and observing in the optical microscope a section cutted (building direction), and consequently analysing the bulk pores observed. According to Bassoli et al. [23], the theoretical value for VED (calculated in subsection 2.2.1) and the *Minitab* software the parameters selected for the first 13 sample bulk DOE are the ones present on Table 2.4.

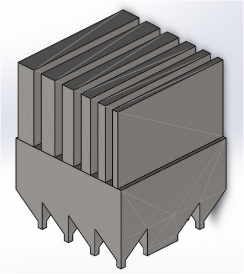

Figure 2.5: Design used for the production done, cube with thin walls. Design given by *Renishaw*. Technical design in Figure A.2 of Appendix A.

Table 2.4: Values for the DOE of PBF-LB parameters of the bulk of the Fe-3.5Si with 13 samples, printed with cube with thin walls.

Parameter	Value
Layer thickness	30 μm
Laser power	200 – 250 – 300 W
Laser scanning speed	500 – 750 – 1000 mm/s
Hatch distance	0.09 – 0.11 – 0.13 mm
Scanning strategy	Meander 67°
Laser mode	CW ($E_t = 20\mu$s)

Figure 2.6 shows a 3D plot of the parameters and the VED of the 13 Fe-3.5Si samples. This

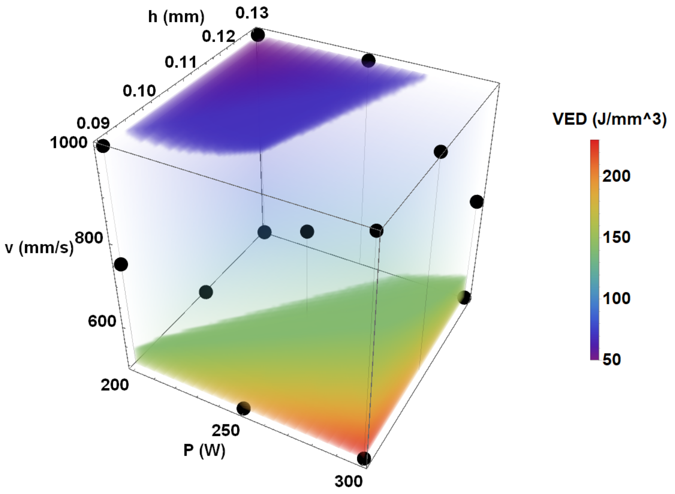

Figure 2.6: 3D plot of the laser power, scanning speed and hatch distance for the 13 samples of the DOE for the Fe-3.5Si, with the VED correspondent.

production would have a minimum VED of 51.3 J/mm^3, that would be inside the theoretical range. The maximum energy would be 222.2 J/mm^3, which is well above the theoretical maximum, around 90 J/mm^3.

To all the parts printed the same procedure like in the first cube production will be followed, from the substrate removal to the microscope observation. After analysing the data from the relative density and the porosity obtained with an optical microscope the best sample from this DOE was sample number 1 (VED = 102.6 J/mm^3, P = 200 W, v = 500 mm/s and h = 0.13 mm). To approximate even more from the optimal combination of parameters is done another DOE but this time centred in 102.6 J/mm^3, again with 3 values for each main parameter. Doing this selection with the help of *Minitab* and using values closer to the best one from the previous DOE, the values used are present in Table 2.5.

Table 2.5: Parameters used in the second DOE for the Fe-3.5Si alloy. Presented only the changes from the first production done. Printed with the cube with thin walls.

Parameter	Value
Laser power	170 – 200 – 230 W
Laser scanning speed	300 – 500 – 700 mm/s
Hatch distance	0.12 – 0.13 – 0.14 mm

The densities of all samples built are measured, with the Archimedes principle (see below) and with image analysis being selected the best sample with the parameters that reach better densities, and for other words, best bulk material. It was observed that the density obtained in the previous DOE reach better values than in all new combinations of the second DOE, for that reason, the best sample was maintained, sample 1. From this point on, Archimedes density was not considered, because several measurements of the same samples were done with this method giving distinct results, leading to completely different relative density values and also not being similar to the densities obtained with the imaging analysis.

Border development

With the main goal of obtaining a better finishing in the surfaces of the parts printed, another two DOE's were developed. In this case, the better bulk parameters obtained above will be maintained, only changing the border parameters, in two laser scans done along the boundary region. The analysis of the properties of the pieces printed will be the relative density, porosity (using only optical analysis), now with a special focus on the boundary area and the surface roughness. New pores could be formed in the border region when new scans are done along the surface, being important to test this region. As well as the thin walls cube, from Figure 2.5, is used another geometry to analyse the border parameters, being used the part shown in Figure 2.7 (also represented in Figure A.3 of Appendix A). This design is appropriate to test these parameters because was upskins and downskins, angled surfaces without solid support.

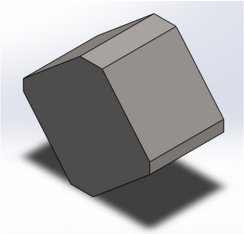

Figure 2.7: Design used for the production done, boundary piece. Design recommended by Bassoli et al. [23]. Technical design in Figure A.3 of Appendix A.

Several parameters of the borders scans were varied, the power and scanning speed of the laser beam for each border. The distance between the inner border scan and the boundary of the bulk scans, called hatch offset and the border distance (distance between each border) were also changed. The difference between the borders are in their location, the main border (volume border) is the outside one, being considered the additional border the ones located to the inside, that in our case is just going to be one for each type, but could exist more than one or no additional borders. Note that the border distance values should always be bigger than the absolute value of the hatch offset. The hatch offset values are usually negative to create an overlap between the bulk and border scans. The parameters tested are the present in Table 2.6. Observing with special focus the border of the samples obtained, for the thin walls cube and border piece produced with equal parameters, there is a combination of values from Table 2.6

Table 2.6: Parameters tested for the boundary scans used in the first border DOE, printed with the cube with thin walls and boundary piece.

Parameter	**Value**
Volume border power	200 – 300 – 400 W
Volume border scanning speed	100 – 300 – 500 mm/s
Additional border power	200 – 300 – 400 W
Additional border scanning speed	100 – 300 – 500 mm/s
Hatch offset	−0.01; −0.03; −0.05 mm
Border distance	0.05 – 0.07 – 0.09 mm

associated to the best sample from each geometry, this is also based on the pores on that region and the roughness measured in the surfaces.

Like in the bulk development, a second DOE was done, with the values of the varied parameters closer to the best sample, using the software *Minitab* to locate the values in the desired positions centring on the better sample values. For this second DOE the border distance was fixed as 0.09 mm and the volume border scanning speed as 500 mm/s, mainly because the less rough samples all had this values in common. In this production the main bulk parameters selected before were again used, being the new values tested for this production presented in Table 2.7. Analysing this samples was selected the better sample, in terms of roughness and porosity located in the borders, having in consideration both geometries.

Table 2.7: Parameters used in the second border DOE, printed with the cube with thin walls and boundary piece.

Parameter	**Value**
Volume border power	200 – 250 – 300 W
Additional border power	200 – 300 – 400 W
Additional border scanning speed	100 – 300 – 500 mm/s
Hatch offset	−0.01; −0.03; −0.05 mm

In the last border analysis was reduced the number of borders to only one. Using the better parameters obtained before, two samples (thin wall cube and boundary piece) were produced with the additional border scan removed. For these samples, the porosity and roughness were analysed and compared with the values from the better sample with two borders. It is observed that these final samples do not achieve better characteristics. For that reason, further production will use two borders, which achieves a better finishing.

Cylinder and cube samples production

After achieving the optimised parameters for the printing with this material, bulk and border, by achieving almost 100% of relative density and reasonable low roughness, those are used to print several new parts of two different shapes, cubes like the first production, Figure A.1 and small cylinders with 5 mm of diameter and 10 mm of height (Figure A.4 from Appendix A). This cylinders are used to measure the magnetic properties using the Vibrating Sample Magnetometer (VSM) technology. The cubes, for other hand, are printed to easily observe their microstructure and allow the hardness measurement, being possible because of the bigger bulk area. This production will use again the Meander strategy and also the Stripe (with a size of 2 mm), present in Figure 1.10. Three angle increments will be tested with each scanning strategy: 0°, same scan every layer; 90°, from one layer to other the scanning is perpendicular; and 67°, considered the best increment parameter because is needed 180 layers to the scan be in the same exact position. The nomenclature used for each scanning strategy is the following: M67, M0, M90, S67, S0 and S90, using M and S, for Meander and Stripe, and the number after is the angle increment.

For this six scanning strategies, two heat treatments were done for each one (stress relief and recrystallisation annealing [1]), being needed three samples to each scan, considering the as-built state, giving in total 18 samples. Considering that from those samples, one have to be cutted in the building direction and other in the scanning direction to allow different microstructure observations, 36 samples will be needed. Note that the cylinder samples require an intact sample, for magnetic properties measurement, so, more 18 samples are necessary, increasing the total sample number to 54. It is also known that from the several changes made in the samples, only the scanning strategy will influence the relative density. The PBF-LB parameter values used for the cube and cylinder production are presented in Table 2.8, which are the final parameters by the bulk and border development.

Table 2.8: Parameters used in the final Fe-3.5Si production, designed for cubes and cylinders.

Parameter	Value	Parameter	Value
Layer thickness	30 μm	Volume border power	300 W
Laser power	200 W	Volume border scanning speed	500 mm/s
Laser scanning speed	500 mm/s	Additional border power	400 W
Hatch distance	0.13 mm	Additional border scanning speed	500 mm/s
Hatch offset	−0.01 mm	Border distance	0.09 mm

---

[1] These heat treatments will be explained in the next pages.

Heat treatments

With the cylinders and cubes printed with the final parameters, the heat treatments were applied with the chamber furnace from *Nabertherm* (Figure C.7). The first heat treatment is the Stress Relief (SR) treatment, that allows a removal of the stress in the samples, which is enhanced by the quick cooling rates of PBF-LB. The temperature selected for the procedure was 700°C [76], with the heating done for 1 hour and the cooling in the furnace without assistance until the room temperature. Before the procedure, three vacuum/argon cycles were done to create an inert atmosphere. The same conditions were used for the high temperature treatment, the Recrystallisation Annealing (RA), that like the name indicates the high temperatures generates a recrystallisation, reforming of the existing grains, and in some cases enhancing a grain growth in the material. The temperature used for the treatment was 1000°C [113], with the cooling being again in the furnace until the room temperature. After the heat treatments to remove the oxide layer that is generated in the surface of the pieces is used the glass blast cabinet *Normfinish DI12* (Figure C.8) to leave the pieces with a better finishing and also helps to reduce slightly the roughness. After this procedure the pieces are ready for the magnetic and hardness measurements, and grain observation with etching.

2.2.4 Preparation of Fe-6.5Si alloy samples

Increasing the silicon content from 3.5% to 6.5% in an iron alloy is known to be difficult to produce with conventional technologies due to high cracking susceptibility of the Fe-6.5Si alloys. But once this problem is surpassed, the material has better magnetic characteristics. The same preparation method is applied to the samples of the Fe-6.5Si alloy produced with PBF-LB. It will be again used the *Renishaw* PBF-LB machine with steel substrates. With the help of the *Minitab* software a new range of VED parameter values was selected for the first production. Because the theoretical VED calculated is very close to the Fe-3.5Si alloy, the first production will be equal to the one done for the previous material, using a M67 scanning strategy in the thin walls cube geometry. The first two DOE's, following the Fe-3.5Si methodology, did not reach success values, with many pores and a large number of cracks being observed. The Fe-6.5Si powder mixture and the pre-alloyed Fe-6.5Si gas-atomized powder from m4p was used as raw material.

Crack problems and cooling rate analysis

Theoretically, this Fe-6.5Si alloy is extremely sensitive to cracks due to a ordering of the crystalline structure [75, 81, 82]. The crack density (mm^{-1}) is calculated with Equation 2.6. This parameter is the ratio between the sum of the length of the cracks and the area of the sample in the image, representing the number of cracks present in the observed sample.

$$CrackDensity = \frac{\sum CracksLenght}{ObservationArea} \tag{2.6}$$

PBF-LB has one of the highest cooling rates among the several metal AM techniques, achieving rates of 10^6 °C/s [16]. The cooling rate may be controlled by changing the main parameters, which has an effect on the energy input. For example, increasing the laser power or decreasing the laser scanning speed, which has the consequence of raising the VED, makes the cooling rate decrease. A quicker cooling rate could be a solution to avoid the ordered phase transformations. For that reason, several strategies were tested to reduce the energy input and achieve a faster cooling rate.

Modulated laser

The first approach tested was a change in the laser wave. Instead of the continuous laser beam, with an exposure time E_t of 20 μs, the modulated laser will be used, which uses $E_t = 40$ μs. The best samples from the first DOE were tested with this change in exposure time. Increasing the time of exposure, inputs more energy into the powder bed, decreasing the cooling rate.

Laser beam focus

Another parameter tested to observe if the cracking on the samples is reduced, is changing the focus position of the laser beam. This change is automatically done by the machine, being possible to place the focus of the laser, before and after the powder layer, this increases the area melted but deposits less energy, because the laser is unfocused, increasing the cooling rate. The focus positions tested were z equal to $+5$ and -5 mm, considering z perpendicular to the layer plane and $z = 0$ the position where the focal point is exactly in the powder layer. Again the best samples from the previous DOE's are tested with these different parameters to observe the effect on cracking.

Double melting

Another technique used to try to eliminate the cracking was the double melting, which is the melting of the same layer two times. This layer melts could be in two different strategies or angle increments, but could also remelt in the exact position twice, which was the case tested, being used the M67 strategy. This remelting eliminates possible pores still existing in the sample but also could help with the cracking by melting the alloy produced from the powder, lowering the tensions accumulated.

Fe-6.5Si-0.05B production

Another approach studied was the addition of a small amount of boron to try to eliminate the cracking formation in the Fe-6.5Si by change its chemical composition. Boron was the element chosen because could prevent the formation of the phases that lead to cracks (B_2 and $D0_3$). The percentage of boron could be considered almost residual, being only 0.05 wt.%. Alloying with boron also has the effect of increasing the strength and ductility of the iron alloy [114]. Several samples, including cylinders and cubes, were built to investigate the effect of the boron addition on the hardness and magnetic properties of the Fe-6.5Si alloy.

2.3 Sample characterisation

2.3.1 Archimedes density measurement

When the produced samples have been removed from the substrate, one of the properties which could express the densification is the relative density. The density ρ is defined as the mass per the volume, $\rho = m/V$. This looks at first sight a relatively easy property to measure, but in the presence of materials with strange shapes, could be a difficult job to correctly measure the volume and density. The Archimedes technique could provide the measure of the density without the measure of the volume of the object. This principle is based on the comparison of two different mass measurements, one in air and one with the piece inside a liquid [115]. This liquid is traditionally water, but could be alcohol or even acetone, being important to known what liquid it is because this method will use his density. In this process, it is also important to know the temperature of work, mainly because the liquid density is temperature dependent. The Archimedes density could be calculated with:

$$\rho_{part} = \frac{m_{air}}{m_{air} - m_{liquid}} \times \rho_{liquid} \tag{2.7}$$

Where m_{air} and m_{liquid} are the mass of the sample in air and in the liquid, respectively, and ρ_{liquid} is the density of the fluid, at a given temperature. Knowing those three values, the density of the part, ρ_{part} could be calculated [115]. With this density and knowing the theoretical density, the relative density ρ_{rel} is possible to calculate with ρ_{part}/ρ_{teo}, giving a percentage, corresponding this value to the filling of the piece.

The porosity is defined as the inverse of the relative density, which would mean, $Porosity_{part} = 1 - \frac{\rho_{part}}{\rho_{teo}} = 1 - \rho_{rel}$. Therefore, a part with a density of 95.6% have a porosity of 4.4%. That porosity value is not linear and other defects in the part could change this value, like remaining powder inside the pores for example. Other way to measure this value is by image analysis, making a ratio between the area of the pores and measuring area.

For this procedure was used the analytical balance from *Kern* shown in Figure C.9. The calculation of density is totally done in the balance, being only responsibility of the user to measure the mass in air and inside a liquid, like observed in Figure C.9. The type of liquid used is indicated in the machine to be considered in the final density calculations, being water selected for this work. After the two different measurements the balance indicates the density in g/cm^3. To calculate the relative density the ratio between the value measured and the theoretical density value for Fe-Si alloys is done (Table 2.2).

2.3.2 Sample etching

The etching, technique used to highlight the grains of the samples printed, is a technique that is used to remove material with chemical reactions, generally using acids. To etch the Fe-Si alloys was used nital which is a solution of nitric acid and alcohol (could be ethanol or methanol). For the work is selected the nital 2% with ethanol, recommended for steels grain observation. This solution is typically explosive for a high percentage of nitric acid, so for that reason the preparation and application in the samples were done inside a glove box with a controlled atmosphere, rich in argon, that would prevent explosions. After mixing all the components to reach the nital 2% the application in the mounted sample, previously polished, is done by submerging the surface to etch in the nital. The time inside the nital was an iterative process because it needed to be perfect to allow the visualisation of the grains, less time than necessary would not etch enough and too much time inside the nital would etch to the point where no grains are observed, being the range of time very small. After several attempts the time stipulated for the Fe-Si alloys etching was 10 seconds inside the nital. After this process alcohol is passed in the surfaces and dried, being ready for the grain observation.

2.3.3 Optical and electronic microscopy

After the etching, the grains from all the samples were observed in the optical microscope, and the densest sample, M67, was observed in the SEM microscope to observe the composition (EDS) and structure. For the procedure was used the SEM microscope *JEOL JSM-6500F* and EDS *Oxford Instruments X-Max*^{N} (Figure C.10). Note that before the etching all the samples were observed with the optical microscope to calculate the relative density and observe the presence of pores.

Preparing the sample to be observed on the optical microscope is done by mounting the sample in epoxy. But before is important to cut the samples to have a bulk section to observe. The cutting machine *Struers Labotom-5* (Figure C.11) is the equipment used. The samples are cut along two different directions, the building and scanning directions, vertical and horizontal planes, respectively.

The mounting of solid parts is done with the hot mounting machine *Buehler SimpliMetTM 4000 Compression Mounting System* (Figure C.12). The mounting machine allows to mount several samples in the same mount at a quick time. The machine works by applying recommended pressure and heat to the epoxy above the samples, placed with the observation face down and the mounting material covering them. For this work is selected the transparent epoxy, *TransOptic*, and the conductive epoxy, *PhenoCure*, when the samples are going to be observed with SEM, both from *Buehler*.

After the mounting, the polishing process starts with the main objective being getting an observation area without scratches. The followed procedure is the same described for the powder samples.

Finally, the analysis was done using the same optical microscope from Figure C.6, being taken photos with several magnifications. With those images and using the software *ImageJ* is possible to measure the density of the sample by calculating the porosity, which is the percentage of area that the pores occupy when compared with all images. With this value, the relative density (inverse of porosity) is obtained and a relation to the VED is possible to define. From image to image it is important that a previous threshold is applied, differentiating in binary the holes and bulk material.

2.3.4 Roughness measurement

An important feature that influences the properties of the samples, especially soft magnetic materials, is the surface roughness [67]. Surface Roughness measurement is considered the measurement of the small scale variations in the height of a physical surface [116]. This contrasts with larger scale variations such as form and waviness which are typically part of the geometry of the surface. There are two types of roughness measurement, the contact-based and non-contact-based, being the first usually done with a dragging tip and the second with an optical approach [117]. Among other values of roughness that can be measured there is the R_a that indicates for the length of the measurement, the arithmetic average surface roughness, basically indicating the average difference between peaks and valleys of the surface [118]. The R_q is the root mean square average of the profile heights. R_z is the average of maximum peak to valley height of the profile for several lengths [119].

The equipment used to measure the roughness in the surface of the sample was the shown in Figure C.13. It is a portable surface roughness tester *Mitutoyo SJ-210*. The equipment consists on a tip (cantilever) dragging above a surface, measuring the highs and lows of the tip, measuring automatically the several roughness values, R_a, R_q and R_z. The process always starts with a calibration, with a standard surface, with $R_a = 3$ μm, doing the system the adjustment to that value. Note that some surfaces are not possible to measure because the roughness is high, not allowing the cantilever to move correctly. This measurement will be done to every sample, but will be more important once the focus is in the boundaries building parameters.

2.3.5 Hardness test

One property that will be study in this work will the hardness of the materials used. For this analysis several techniques are possible to use, being chosen the Vickers hardness, which ideally creates a rotated square indentation in the material [121]. The average length of those two diagonal (seen in Figure 2.8 (B)) gives the hardness value of the material.

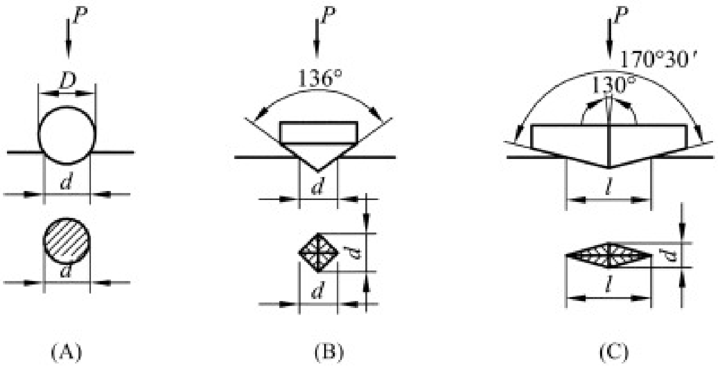

Figure 2.8: Three hardness methods existing, with the different indentations, sphere, diamond pyramid and thinner pyramid, named respectively, **(A)** Brinell test, **(B)** Vickers test and **(C)** Knoop test, [120].

To measure the hardness of the samples, it was used the machine *EMCOTEST DuraScan 70 G5* shown in Figure C.14. The machine allows the measurement with Hardness Vickers (HV). The measuring process starts by placing the sample with the surface to be analysed upwards, as seen in Figure C.15, below the indentation seen. Usually is recommended that the sample is mounted in resin, making sure that the analysed surface is horizontal. With the microscope of the machine, on the right in Figure C.15, it is possible to focus the microscope image, to have the focus point exactly in the sample surface, defining its position and achieving a better quality image. Using the *EMCOTEST* software, the weight to be applied as well as the 2D locations for each indentation in the surface are defined. Being memorised by the system, allowing to know the location of each hardness value.

After this preparation with the software, the measuring process consists in making an indentation with the defined weight and after, in that same position, the machine takes a picture of the spot, measuring the size of the indentation (his diagonals), continuing this cycle until every point selected in the software is analysed.

To this work Hardness Vickers with 1 kg, or HV1, was selected for the measurements, being characterised by the pyramid indentation. The measurement consists of a relation between the average length of each diagonal of the indentation with the hardness for the weight selected. For a defined weight the software uses a corresponding table, between the diagonals and the hardness, giving the final hardness value. The problem with the measurement of the diagonals is that sometimes, automatically, the software can not find the corner and, consequently, calculates a wrong hardness value. Even being an automatic procedure, is necessary to verify each indentation. This process was followed to measure the hardness in every single sample printed of both alloys.

2.3.6 Magnetic Properties

The materials printed need an evaluation of their magnetic properties, mainly to observe if they will reach the desired parameters. An equipment would have to be selected to measure properties like the coercivity and permeability, for other words, achieve the hysteresis curve. At first, the Superconducting Quantum Interference Device (SQUID) was the chosen option for the measurement because is one of the most sensitive magnetometer sensors, being able to measure very small magnetic fields, voltages and currents [122]. But being the materials studied strong ferromagnetics and the samples mass higher than a few mg, they would easily saturate the magnetometer. Alternatively, another technique was selected, using a Vibrating Sample Magnetometer (VSM), with smaller resolutions that could still measure the properties desired. As the name indicates VSM is a magnetometer where the sample vibrates in the presence of a constant external magnetic field. The left Figure 2.9 shows a schematic of the VSM, also presenting some of the necessary components. VSM uses Faraday's Law of Induction, to induce an electromotive force in the pick-up coils that is proportional to the magnetisation of the sample [123].

To define the hysteresis curves the external magnetic field is varied in intensity and direction with an electromagnet. If the sample is magnetic, the field will magnetise the sample by starting to align its domains with the field. The stronger the field is, the higher the magnetisation will be. The magnetic dipole of the sample will also create a magnetic field around the sample,

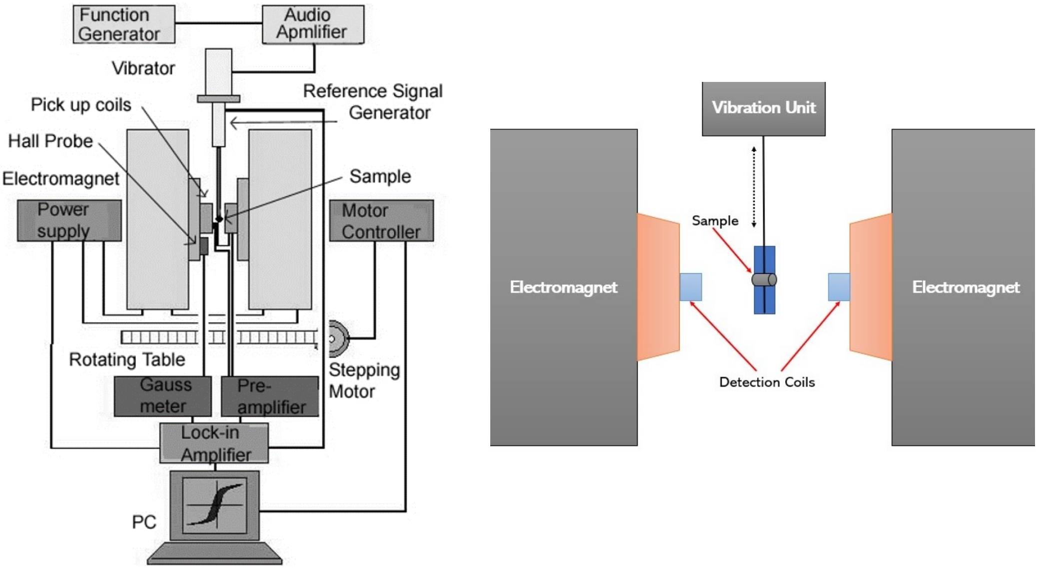

Figure 2.9: (Left) Schematic of a VSM system with all the components necessary, [124]. **(Right)** Position of the cylinder to be measured in a simplified VSM schematic.

called demagnetising field or magnetic stray field. This field has an opposite direction to the external field applied by the electromagnet. The greater the magnetisation, the greater the induced electromotive force.

Previous calibrations between the current/magnetic field and voltage/magnetisation are required to convert the current passing through the electromagnet and the voltage measured in the pick-up coils in the applied field H and magnetisation M. An important factor to consider in this measurement is the demagnetising field, which does not affect the coercivity, but changes the permeability calculated for the sample. This field is associated with the magnetisation and decreases the internal field in the sample. Different material shapes and sizes will create different demagnetising fields. The sample internal magnetic field is the result of the external magnetic field and the demagnetisation field $-D \cdot M$, where D is the demagnetisation factors (depending on the direction and shape of the sample).

$$H_{int} = H_{ext} - D \cdot M \tag{2.8}$$

The measurement of the hysteresis of the printed cylinders is done with the VSM technology, Figure 2.9 on the right, placing the cylinder with the building direction parallel to the applied field, which is directed between both poles. The VSM system is controlled by a lock-in connected to the other equipments: the vibration unit, responsible for the vertical sample vibration, two detection coils, which detect the field around the sample and one current source that powers the electromagnet, which applies the external field. After increasing and decreasing the current/field the magnetisation of the sample is measured by the pick-up coils. The equipments used for this measurement are the ones present in Figure 2.10.

Figure 2.10: **Top row:** *Model SR830 DSP* lock-in amplifier from *Stanford Research Systems* and *Bruker B-MN C4* power supply, respectively. **Bottom row:** Electromagnet *Magnet B-M6* from *Bruker* and detail of the vibrating sample located in the middle of the electromagnet and pick-up coils, respectively.

The measurements were done from a range of applied field between −15 and 15 A of current in the electromagnet, with an increment of current of 0.1 A. The stabilisation time was used as 2 seconds, which is the time after the applied field change and a new field is applied. The frequency of sample vibration used for all the measurements was 20 Hz. The relations obtained for the current/magnetic field and the voltage/magnetisation were obtained using a calibrated nickel sample and a Hall sensor, giving the following equations:

$$H_{ext}(\mathrm{A/m}) = -3.7 \cdot I^3 - 3.2 \cdot I^2 + 27500 \cdot I + 594 \tag{2.9}$$

$$M(\mathrm{A/m}) = 4.7 \times 10^8 \cdot V \tag{2.10}$$

To calculate the induction B is multiplied the magnetisation M for μ_0 or $4\pi \cdot 10^{-7}$, giving the induction in Tesla. It is ignored the field H since this value is much smaller than M. Note that like Equation 2.8 indicated, the internal field will be smaller than the external field, being the relation done with the demagnetising field. The demagnetising field factor for a cylinder with a fraction between the length and diameter, $L/2R$, is defined in Crabtree [125]. The factor D, for the cylinders built, that have a fraction of 2, is 0.181. This value will be multiplied with the magnetisation and then subtract from the external field from the electromagnet, to achieve the internal magnetic field of the cylinders.

When the whole hysteresis curve is obtained several properties could be measured, for this type of materials the main ones are the coercivity, saturation induction and permeability. The coercivity will be calculated by measuring the magnetic field in both intersections with the x axis, $B = 0$ T, not considering the initial point which begins in the origin. With those values, one positive and other negative, a sum of both absolute values will be done, dividing by 2, for other words, an average will be done to achieve the coercivity. The same procedure will be done for the saturation induction or maximum induction. But instead of just observing the maximum, it will be considered the maximum and minimum value (which is negative) and will be done an average with the absolute values.

The calculus for the permeability is done by measuring the slope of the initial 25 points of the loop, being done a linear regression. It is important to note that both axis should be in the same units, in this case, A/m, because the permeability measures the proportionality of the magnetisation and the field. For that reason, the y axis B is changed from Tesla to A/m, in other words, change to M values (B/μ_0). Another property possible to measure with the B-H loop is the hysteresis losses. This characteristic could be measured by the area inside the loop, the bigger the area of the curve, more losses will be felt during the magnetisation processes of the material. The strategy followed to measure the interior of the curve is based on Figure 2.11, measuring the left area until the B axis from the left side of the curve (ii) and from the right side (i), when the field is first decreasing and when is last increasing to complete the hysteresis loop, respectively. The difference between those two areas, (i) minus (ii), will equal the area inside the loop (iii), being this value considered the losses due to the hysteresis of the material. Conventionally, the power losses are presented in W/kg, in other words, will be considered the weight of each sample. This procedure was done to every sample printed in the work, being only considered to analyse the final pieces that achieved a higher relative density, and where the scanning strategies and heat treatments are varied.

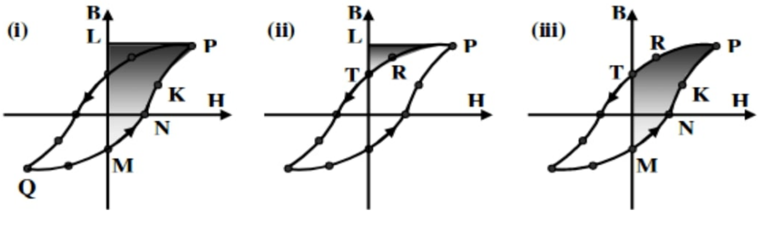

Figure 2.11: Steps to measure the hysteresis losses, measure of several area to achieve the area inside the loop, [126].

2.3.7 X-ray diffraction analysis

X-Ray Diffraction (XRD) is used to identify the phase composition of the samples. XRD works with base on the Bragg's law equation: $n\lambda = 2d\sin\theta$ [127, 128]. The samples of the Fe-Si alloys, including the powders of the pure Fe, pure Si and powder mixtures were submitted to an X-ray diffraction. From the 3.5%Si content pieces were selected the M67 samples, with every heat treatment done, as-built, SR and RA. From the Fe-6.5Si alloy, two samples with and without double melting were tested. For this procedure was used an X-ray diffractometer *Miniflex* from *Rigaku*.

3

Results and discussion

In this chapter, the results obtained in the work done are presented with analysis and discussion.

3.1 Powder analysis

The size and shape of the powders are analysed with sieving and microscopy.

3.1.1 Iron powder

The first powder analysed was the iron powder (99.0% purity), which was sieved and the particle size distribution is presented in Figure 3.1. It is possible to see that the biggest percentage, 38.7% of the particles, shows a size range of 20 to 38 μm, with base on the sieving. The previous result is confirmed with optical microscopy and image analysis. Some images of the iron powder are observed in Figure 3.2. Comparing the iron diameter sizes measured with optical analysis with the aperture size of the sieves, Figure 3.1, it is seen that both maximum values are near each

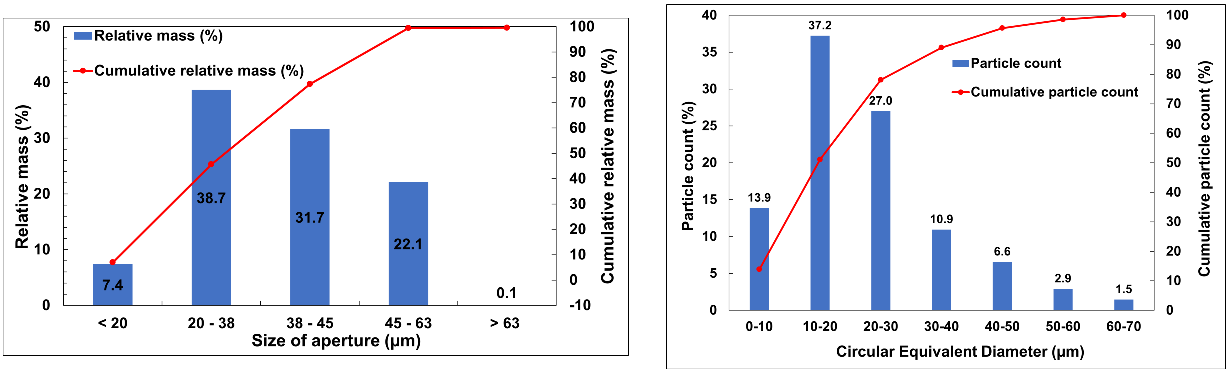

Figure 3.1: Size distribution of the iron powder, obtained with the sieving process **(left)** and with image analysis of the optical microscope images using *ImageJ* **(right)**. It is presented the relative mass and its cumulative, adding to 100%.

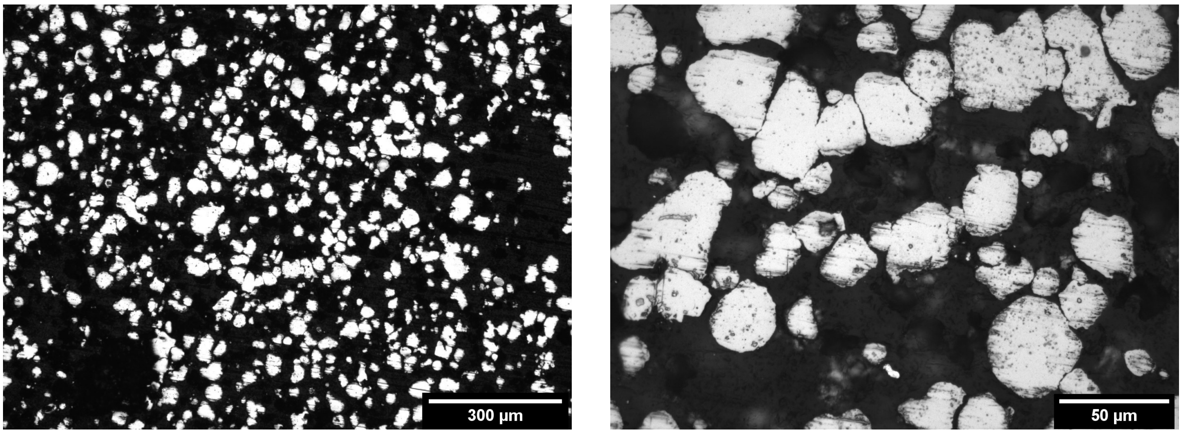

Figure 3.2: Optical microscope images of the iron powder, at different magnifications, 100× and 500×, respectively, from left to right.

other. The sieving indicates between 20 and 38 μm and the microscopy indicates 10 to 20 μm as the bigger percentage of particles within that diameter. Could be interpreted that around 20 μm is the average size of the particles in the pure iron powder.

3.1.2 Silicon powder

The silicon powder was observed in the optical microscope (Figure 3.3) and it could not be dry sieved due to agglomeration. It is noted in the images that the particles are very fine, with a size below 10 μm. Another observation from Figure 3.3 is the shape of the particles, where it may be seen that they are irregular and non-spherical. Some particles are elongated (high aspect ratios), which could be difficult to spread the powder during the printing process.

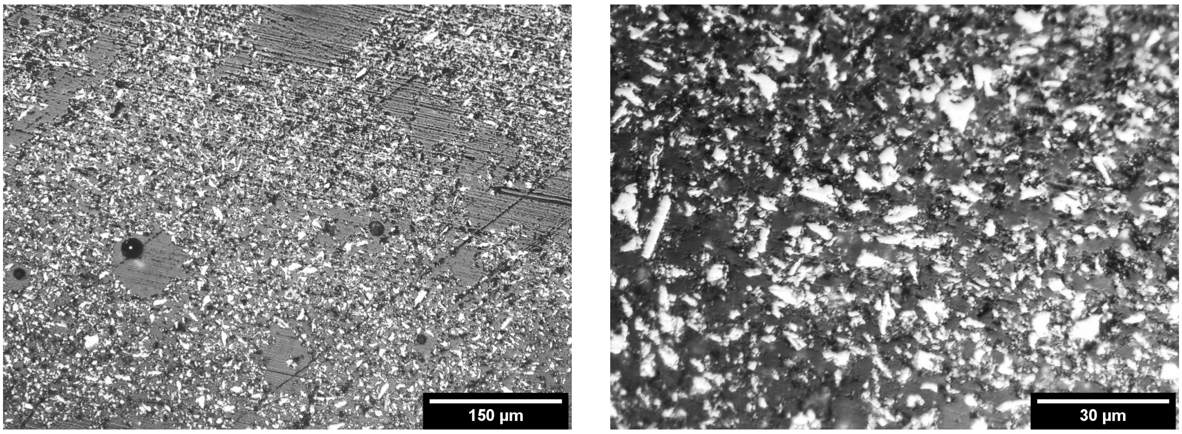

Figure 3.3: Optical microscope images of the silicon powder, at different magnifications, 200× and 1000×, respectively, from left to right.

Figure 3.4 shows the results of image analysis of the optical microscopy of the silicon powder, where is counted the number of particles observed within the equivalent diameter indicated. Note that this value is only possible to calculate by approximation every particle to a sphere. Most of the diameters of the silicon particles are located between 2 and 3 μm, with a huge difference from the iron particles. Table 3.1 presents other parameters calculated with image analysis of the optical microscopy. The shape observed in the microscope images show that the silicon powder is not spherical, due to the low circularity and roundness, being more elongated (high aspect ratio), properties that could difficult the PBF-LB process. The iron particles despite being slightly more round, still are not a perfect sphere (aspect ratio of 1.43), but its shape and size, being more circular and bigger is more recommended for powder spreading. The Feret diameter confirms the size difference between Fe and Si powders.

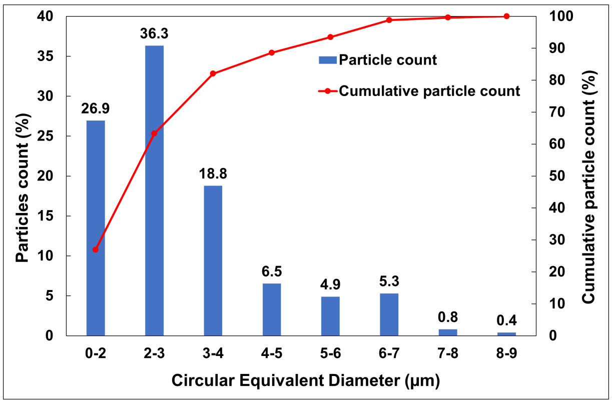

Figure 3.4: Size distribution of the silicon powder, with image analysis of the optical microscope images using *ImageJ*.

Table 3.1: Average shape factors of both powders, iron and silicon, obtained using *ImageJ* particle analysis of the higher magnification images from Figure 3.2 and 3.3.

Parameter	**Iron**	**Silicon**
Aspect ratio	1.43	2.51
Circularity	0.76	0.54
Roundness	0.73	0.48
Feret diameter (μm)	38.33	9.29
Solidity	0.91	0.84

3.1.3 Fe-3.5Si powder mixture

After mixing pure iron with 3.5 weight percentage (wt.%) of silicon, the Fe-3.5Si powder mixture was prepared. It is possible to identify both elements using the SEM and the identification of each element performed with the EDS analysis. The EDS map is presented in Figure 3.5 indicating

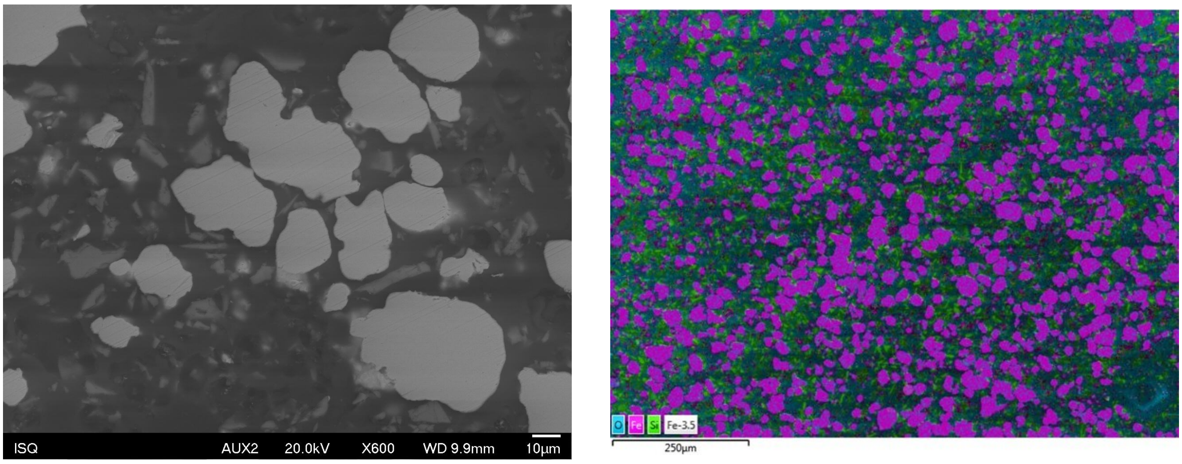

Figure 3.5: SEM microscope BSE image of the Fe-3.5Si powder with 600× magnification **(left)** and representative EDS map **(right)** with the position of the iron **(Pink)** and silicon **(Green)** particles.

that both elements were correctly mixed, not being observed zones with less presence of some element. The BSE image confirms the observation of both elements, being noted the difference in sizes and especially shapes, and noted the elongation of the silicon particles. Figure B.2 on Appendix B have the separated position of each element of the sample.

3.1.4 Fe-6.5Si powder mixture

The same process was done but with 6.5 wt.% of Si to prepare the Fe-6.5Si powder mixture. Following the methodology, the sample was observed in the SEM and the images are presented in Figure 3.6. In the figure, it is observed a coarse iron particle that may be considered an outlier. The EDS map shows that the mixture was successfully made with both elements evenly

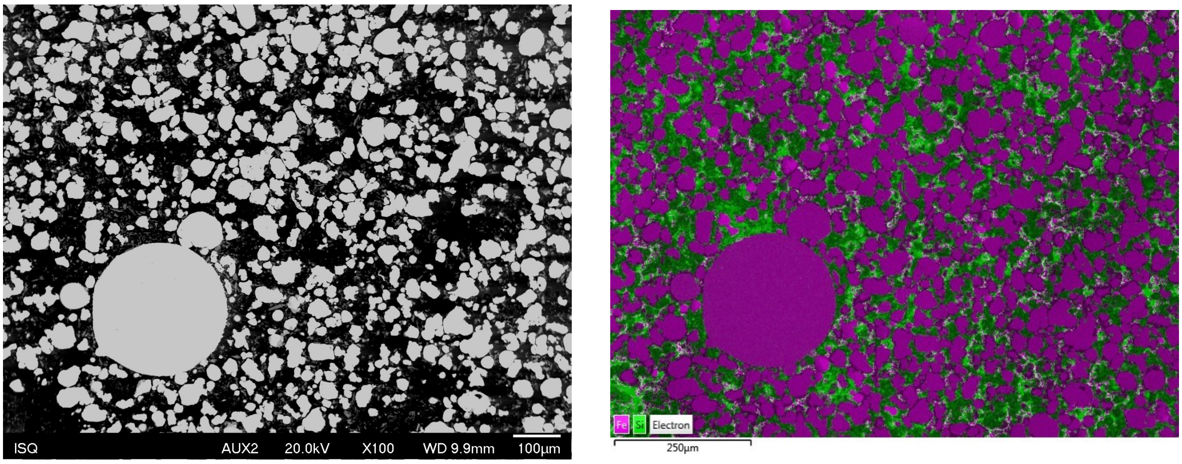

Figure 3.6: SEM microscope BSE image of the Fe-6.5Si powder with 100× magnification **(left)** and EDS map **(right)** with the position of the iron **(Pink)** and silicon **(Green)** particles.

distributed. To easily observe the element position Figure B.5 of Appendix B shows the position of each element. Also in the appendix are presented bigger magnifications of the BSE and SE images, Figure B.4.

3.1.5 Fe-6.5Si pre alloyed powder

Alternatively, the Fe-6.5Si pre-alloyed and gas-atomized powder was supplied by m4p, specified for the PBF-LB process. Figure 3.7 shows the m4p powder at two magnifications. It is observed a big difference to the mixed powders, with all the particles spherical, even achieving circularities of 1 in some cases. In addition, the particles size distribution of the Fe-6.5Si m4p powder shows that a higher layer thickness of the PBF-LB may be selected, compared to the 30 μm used when the Fe-Si powder mixtures were processed, increasing the PBF-LB productivity. This is due to the average circular equivalent diameter measure of 31.2 μm. The SEM image (Figure 3.8) confirms that the powder is smoother and rounder than the previous powders used, apart from the fact the Fe-6.5Si is alloyed in each powder particle. Each particle observed contains the exact specified quantity of Fe and Si. In Appendix B, Figure B.7 shows the position of each element without overlapping and also has the 300× magnification BSE and SE images (Figure B.6).

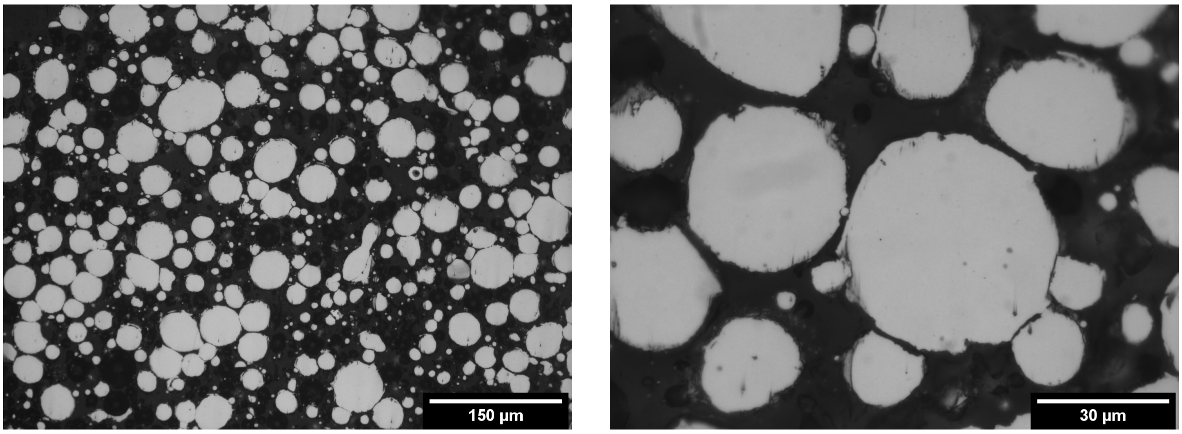

Figure 3.7: Optical microscope images of the Fe-6.5Si m4p powder, at different magnifications, 200× and 1000×, respectively, from left to right.

3.1.6 Powder flowability

The flow rates of the powders used for printing are presented in Figure 3.9. Powders in several heating conditions and with different silicon percentages are presented, along with the pre-alloyed, Fe-6.5Si m4p powder. During the process was seen that for small apertures, the powder mixture were not passing through, which a characteristic of powders that do not spread easily.

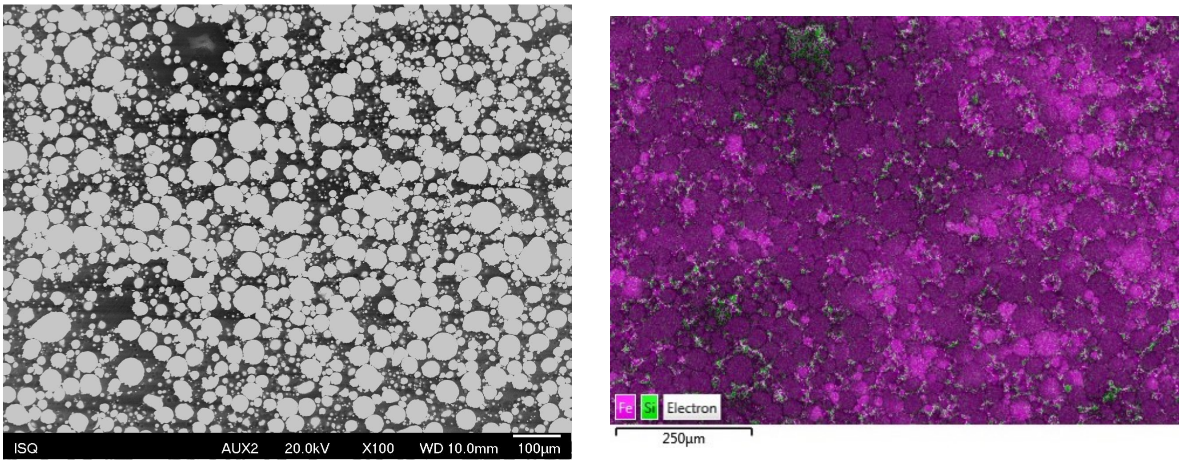

Figure 3.8: SEM microscope BSE image of the Fe-6.5Si m4p powder with 100× magnification **(left)** and EDS map **(right)** with the position of the iron **(Pink)** and silicon **(Green)** particles.

This could happen due to the hydrophilic properties of silicon. To prevent this the procedure was attempted in different conditions: one without heating, one right after heating the mixture and one dried or 1 hour after the mixture heating process was done. The heating process is done at 120°C. It is observed that the powder that achieves the highest flowability is the heated Fe-6.5Si m4p, followed by the dried Fe-3.5Si, showing a clear improvement to the same mixture without the heating. For that reason, before every PBF-LB production the powder was heated in the same conditions to enhance the flowability. Predictably, the higher percentage silicon alloy has a smaller flowability, mainly for the hydrophilic characteristics of silicon, even with the previous heating. The Fe-6.5Si m4p powder is the powder with the higher flowability especially

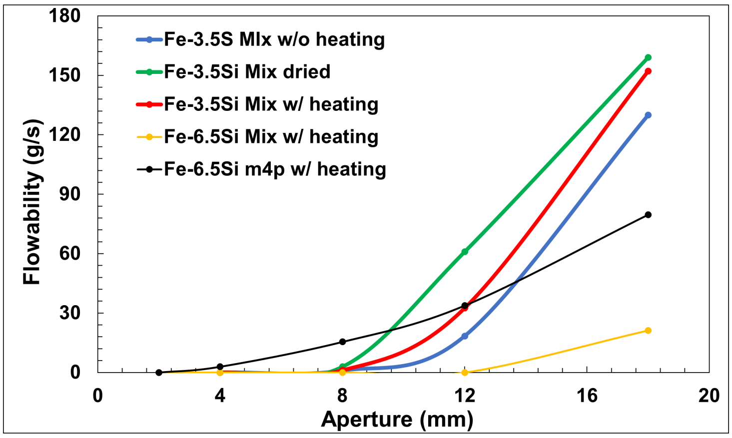

Figure 3.9: Flowability of the Fe-3.5Si and Fe-6.5Si powders, mixture and m4p. The Fe-3.5Si flow rate is measured in three different conditions, with and without heating the powder, at 120°C for 1 hour, and the third case 1 hour after the heating. The Fe-6.5Si flow rates were only measured after the heating in the same conditions.

at smaller apertures because the powder is already atomized and more spherical, as observed in Figure 3.7. This plot indicates the difficulty of processing the Fe-Si powder mixtures in the PBF-LB process, since a low flowability is observed, especially for small apertures.

3.1.7 Boron addition

The addition of pure boron was also considered to the Fe-6.5Si alloy in a tentative to decrease the cracking formation during the PBF-LB process. Therefore, 0.05 wt.% of pure boron in powder form was mixed with the Fe-6.5Si m4p powder. Figure B.8 shows that the boron powder was very fine, being difficult to observe in the optical microscope. Small particles as observed in the right image of Figure B.8 are easier to mix with the alloy under the right strategy of mixing.

3.1.8 Fe-6.5Si + 0.05B powder mixture

The alloy created using the boron powder was a mixture of the Fe-6.5Si m4p powder with the boron powder (0.05 wt.%B). The mixture obtained is very similar to the pure Fe-6.5Si m4p powder because the boron addition is in a residual percentage and could barely be detected with EDS (Figure 3.10). In Appendix B, Figure B.10 shows the position of each element without overlapping. It is noted that the mixture is correctly done, not existing a locating with higher or less concentration of boron. In Appendix B, the BSE and SE images of the powder mixture with higher magnifications are also presented (Figure B.9).

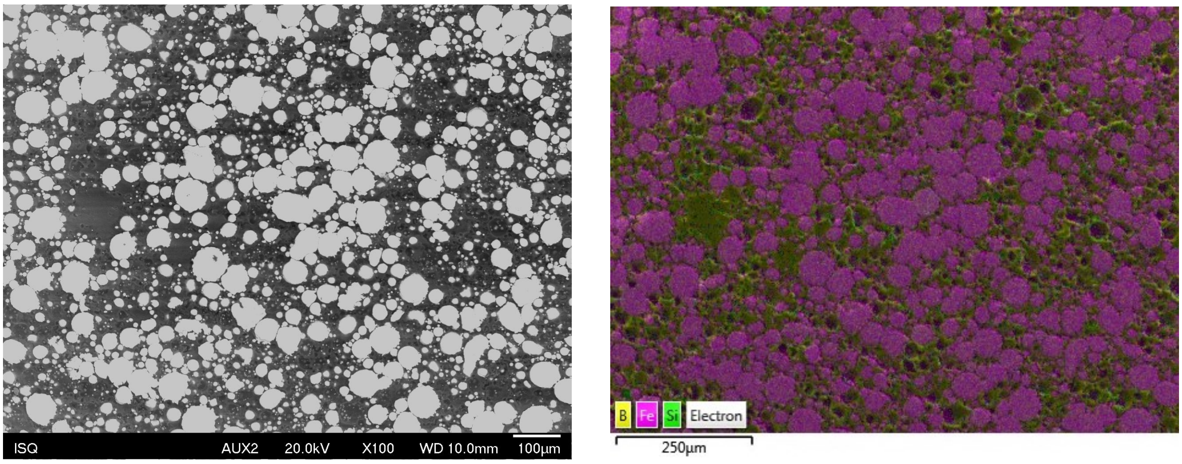

Figure 3.10: SEM microscope BSE image of the Fe-6.5Si m4p + 0.05B powder mixture with 300× magnification **(left)** and EDS map with the position of the iron **(Pink)**, silicon **(Green)** and boron **(Yellow)** particles **(right)**.

3.2 X-ray diffraction analysis

Figure 3.11 shows the XRD patterns of the Fe-3.5Si and the Fe-6.5Si alloys.

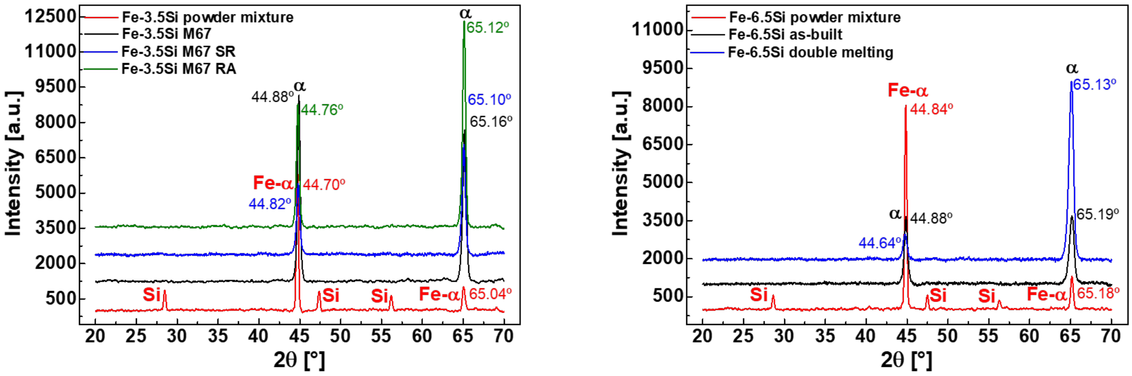

Figure 3.11: XRD of the iron alloys with 3.5% and 6.5% silicon samples.

The analysis is focused in the diffraction angle of the peaks. In the powder mixtures is observed the characteristic peak of the pure iron and pure silicon, in separated, with the iron structure being located in $\alpha - Fe$ with body-centred cubic. This region is also the angle peak location of every peak of the Fe-Si alloys. Therefore, the structure of the samples are constituted of ferrite, as expected from the phase diagram of Figure 1.12.

3.3 Parameter optimisation

The PBF-LB process parameters were optimised for each powder mixture and alloy composition. Some important results like relative densities and surface roughness are present in this section.

3.3.1 Fe-3.5Si alloy

Parameters for the bulk development

As result of the DOEs deployed to obtain the optimised parameters for the Fe-3.5Si alloy, a graphic of VED for the relative density measured using the Archimedes method is presented in Figure 3.12. A peak of the relative density is seen for energies around 100 Jmm^{-3}, being achieved smaller densities in higher and smaller energies. In the first DOE the relative density shows an increase for higher VED values, but this is contradicted by the second DOE where the increase in energy decreases the bulk relative density of the samples. This could be related to the formation of keyholes due to the high energies applied. It was used the Archimedes density values, but a high deviation was observed for these measurements. Therefore, the relative densities were

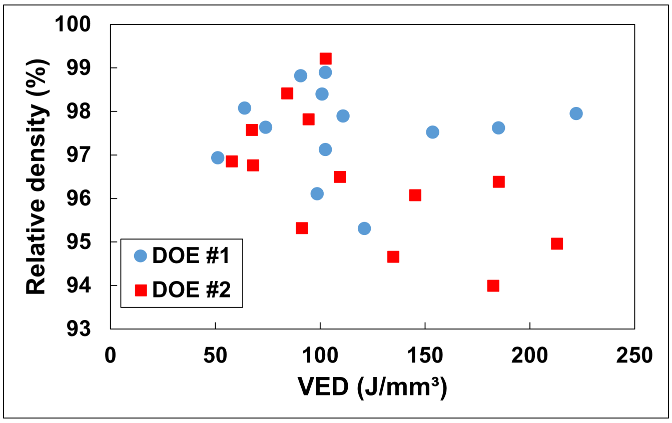

Figure 3.12: Relative density vs VED of the bulk samples of Fe-3.5Si.

calculated with image analysis. For comparison, the sample with the highest relative density with 102.6 Jmm^{-3} presented a relative density of 99.21% as measured with Archimedes. On the other hand, same sample with image analysis showed 99.98% of relative density. Figure 3.13 shows the worst and best samples in terms of relative density from Figure 3.12. The sample with lowest relative density of 93.99% (on the left) is obtained with a VED of 182.5 Jmm^{-3}.

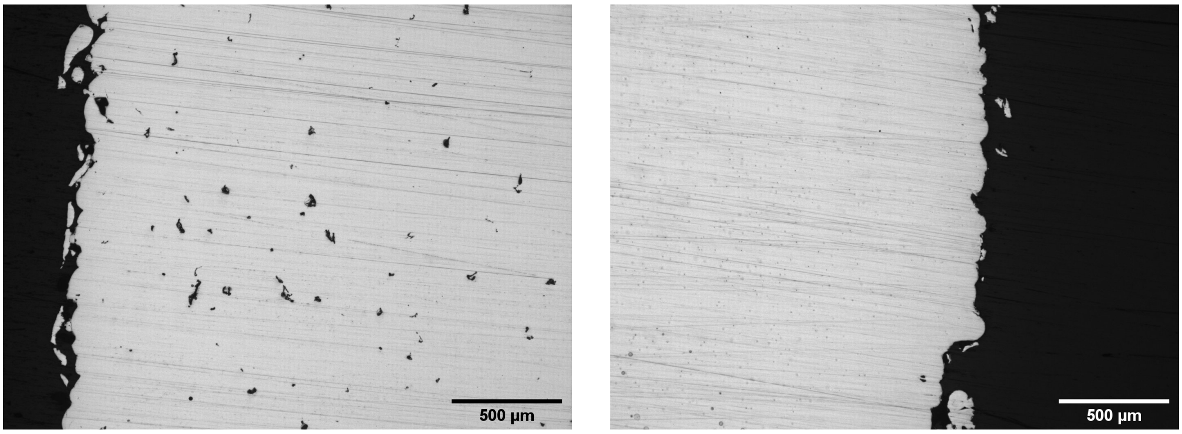

Figure 3.13: Sample with more and less pores in the bulk DOE's done, respectively from left to right.

Parameters for the border development

A similar value to the VED was used to optimise the border of the samples. But this time, the parameter is the Surface Energy Density (SED). This property is a derivation of the VED but considering the laser power used in the border and without the hatching space. Therefore, the SED is given in Jmm^{-2}. Figure 3.14 represents the relative density of the boundaries of the samples (cube with thin walls and boundary piece). In the second DOE for each sample is observed only the region of higher densities, around 17 Jmm^{-2}. The value of 20 Jmm^{-2} is

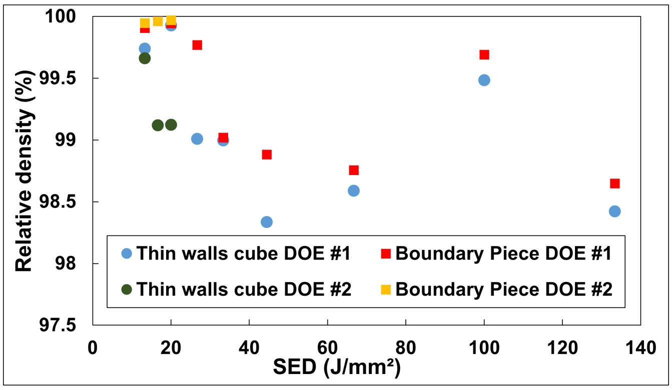

Figure 3.14: Border relative density vs SED of the cube with thin walls and boundary samples form the first and second DOE.

considered the optimised SED for the border of samples of the Fe-3.5Si alloy, since it achieves the higher relative density. The borders in both geometries of the sample with the highest relative density are possible to see in Figure 3.15. Comparing with the borders from Figure 3.13 these borders have a better finishing and lower roughness. The average roughness measured was as low as 4 μm. It was also compared samples with one and two border laser scans and was observed that the relative density did not change significantly. On the other hand, the surface roughness is improved with a second border scan. Therefore, a two border strategy was adopted. For comparison, the best relative density and roughness of the samples with one border are $\rho = 99.96\%$ and $R_a = 7.36$ μm. On the other hand, samples with two border scans achieved relative densities of 99.96% and roughness of 4.92 μm. The optimised PBF-LB process parameters of the Fe-3.5Si alloys was obtained and is summarised in Table 3.2.

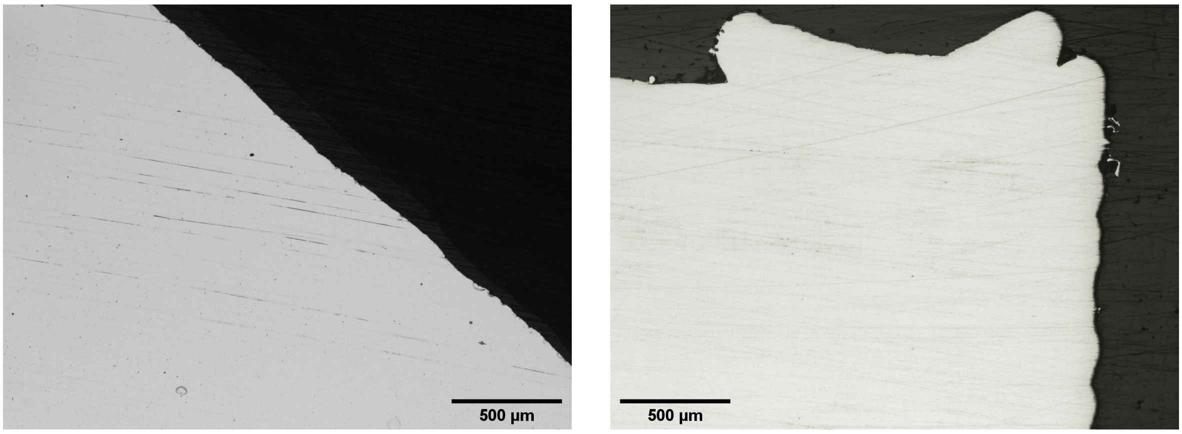

Figure 3.15: Upskin and wall from the samples that achieve higher relative densities in the borders with two border scans.

Table 3.2: Final parameters optimised to achieve the highest relative density and lowest surface roughness for the Fe-3.5Si alloy using a Meander 67° scanning strategy.

Parameter	Value	Parameter	Value
Layer thickness	30 μm	Hatch offset	-0.01 mm
Laser power	200 W	Border distance	0.09 mm
Laser scanning speed	500 mm/s	Number of borders	2
Hatch distance	0.13 mm	Volume hatch	"1"
Volume border power	300 W	Laser mode	CW
Volume border scanning speed	500 mm/s	VED	102.6 Jmm^{-3}
Additional border power	400 W	SED	20 Jmm^{-3}
Additional border scanning speed	500 mm/s		

Scanning strategy

Figure 3.16 shows the difference between the Meander (M0) and Stripe without rotarion (S0), with Stripe size of 2 mm. There are no angle increment and the scanning is in the same position in every layer. It is seen that the Stripe strategy originated more pores, along the separation between Stripes.

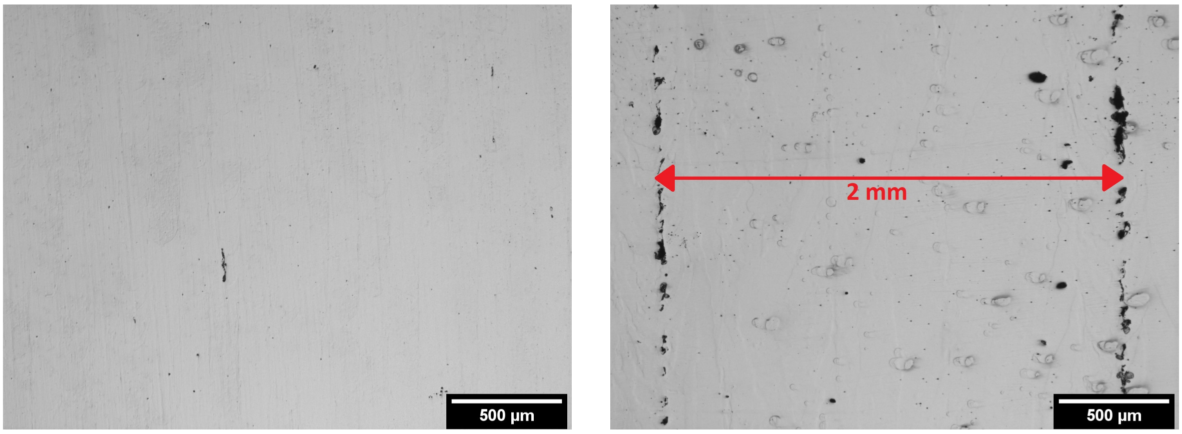

Figure 3.16: Comparison between the bulk material from the Meander 0° sample and Stripe 0° sample, respectively. The dimension of the stripe is presented.

Furthermore, comparing the Meander strategy with 67° (M67), 0° (M0) and 90° (M90) rotation between layers, respectively, it is seen that the M90 in the scanning direction achieve the highest density, 99.98%. This analysis is observed in Figure 3.17. The roughness of these samples was also analysed and the results are presented in Table 3.3.

The microscope images of the etching obtained for the M67 samples are presented in Figures 3.4. It is observed that the grains look very similar in size, being slightly elongated along the building direction, due to the epitaxial growth. In the scanning direction the grains are

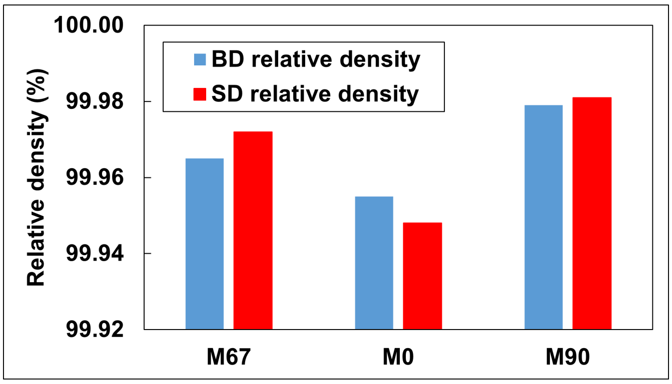

Figure 3.17: Relative density of the cubes in the building and scanning direction of the several scanning strategies build, Meander 67°, 0° and 90°.

Table 3.3: Surface roughness (R_a, R_q and R_z) measured in samples produced with Meander scanning strategy and different rotation between layers, M67, M0 and M90.

Scanning strategy	R_a **(μm)**	R_q **(μm)**	R_z **(μm)**
M67	4.84	6.35	34.06
M0	6.17	7.82	36.75
M90	5.43	7.01	30.80

observed to be formed randomly, in terms of shape, this property could help the alignment of the magnetic domains in the presence of a magnetic field. Between the different heat treatments, no big difference is observed in the grain size and shape.

The next strategy analysed was the M0, Figures 3.5. The main differences observed in this microstructure to the M67 structure reside in the orientation of the grains, observing the scanning direction is seen that the grains follow only the laser strategy, Meander, being observed parallel stripes, caused by the laser melt only in this direction. Along the building direction, the grains are very long, especially with RA. Even with the other heat treatments, this vertical elongation is still observed, due to the epitaxial growth in the melting pool always in the same position.

The last etching samples observed in the microscope were the M90 (Figures 3.6). In the scanning direction, these samples generate mainly grains in the shape of squares because the angular increment of the scanning is perpendicular layer to layer, being the grains formed by the perpendicular scan passage of the laser. In the building direction, like the other strategies, the grains are very elongated, this happens because the angle increment generates a laser scan in the same orientation every two layers, helping the epitaxial growth in those positions. Again, comparing all the heat treatments grains, look similar in shape and size.

Table 3.4: All the etched figures of the M67 Fe-3.5Si samples with all the heat treatments done and presented in building and scanning direction.

	Building Direction	**Scanning Direction**
as-built	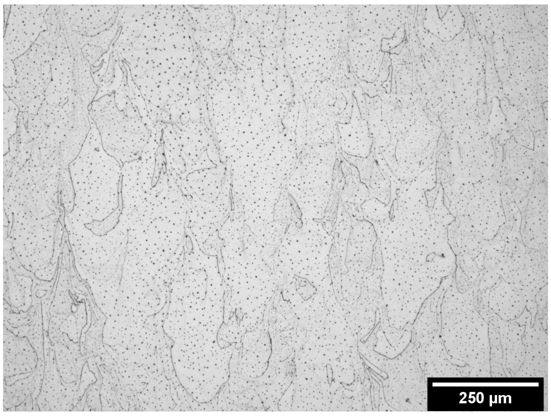	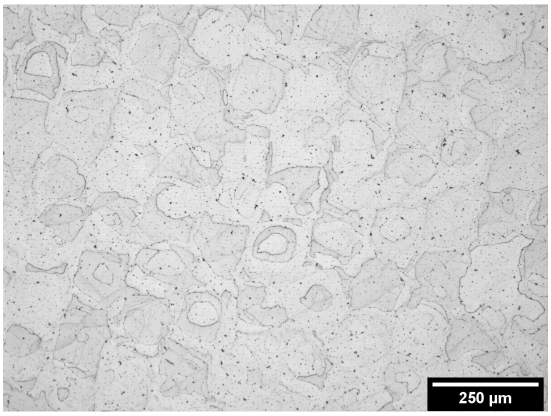
SR	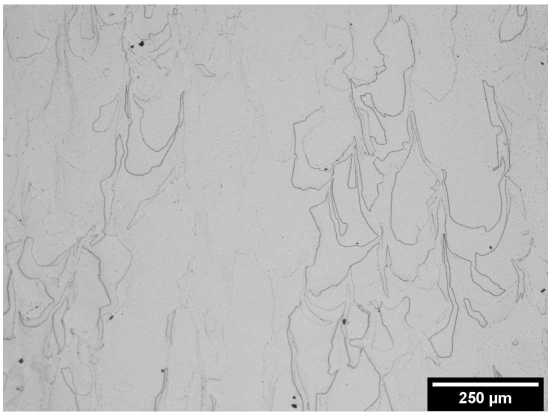	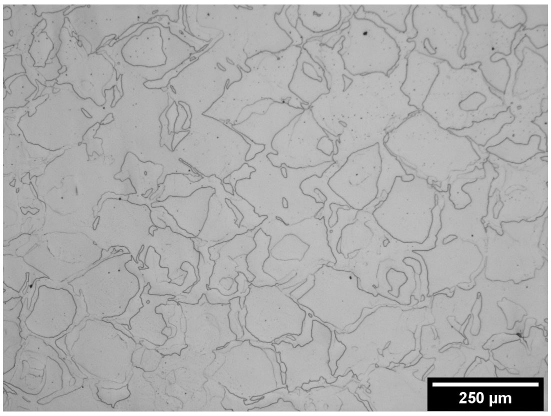
RA	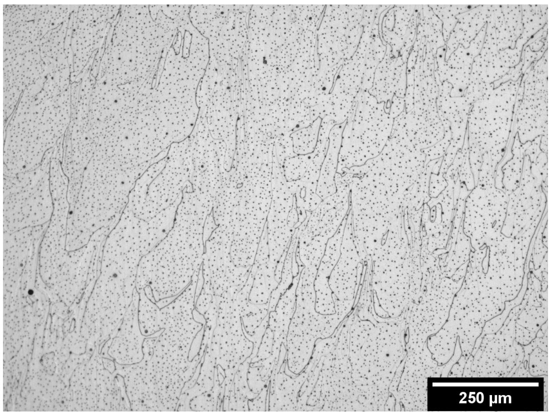	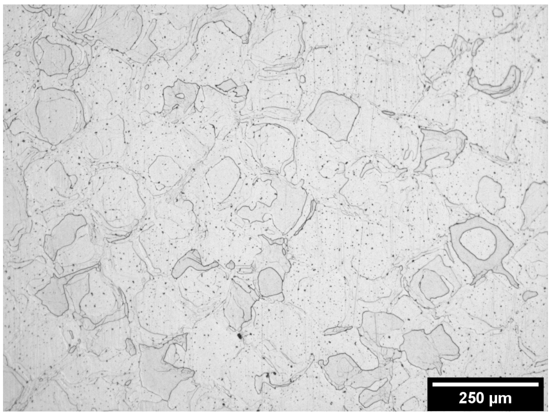

Table 3.5: All the etched figures of the M0 Fe-3.5Si samples with all the heat treatments done and presented in building and scanning direction.

	Building Direction	**Scanning Direction**
as-built	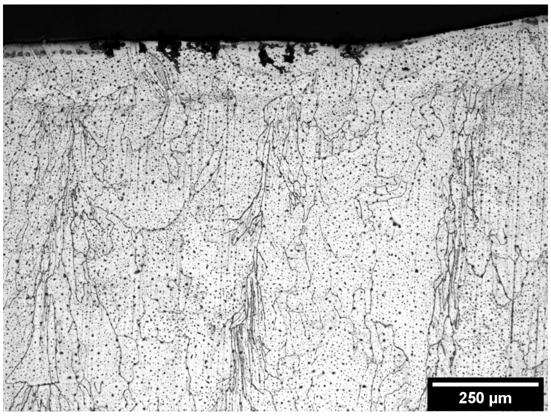	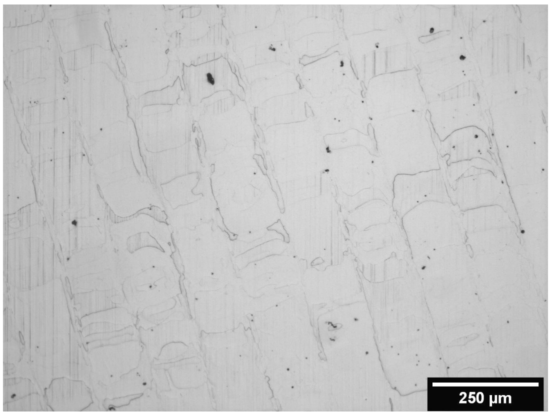
SR	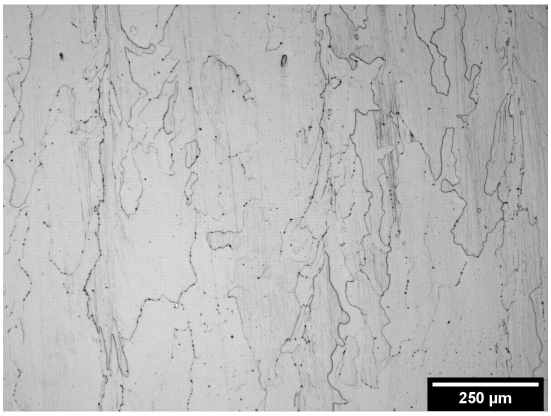	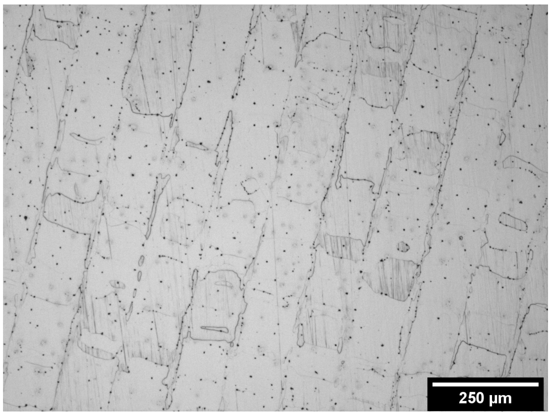
RA	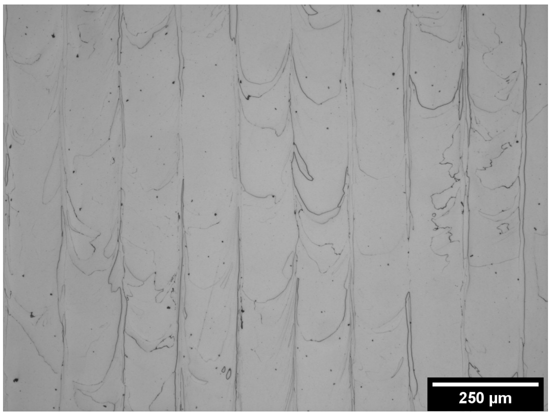	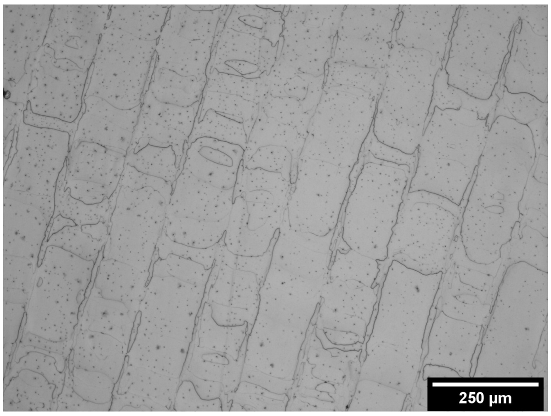

Table 3.6: All the etched figures of the M90 Fe-3.5Si samples with all the heat treatments done and presented in building and scanning direction.

	Building Direction	**Scanning Direction**
as-built	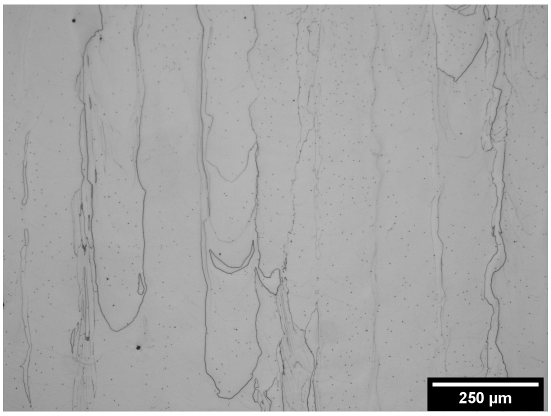	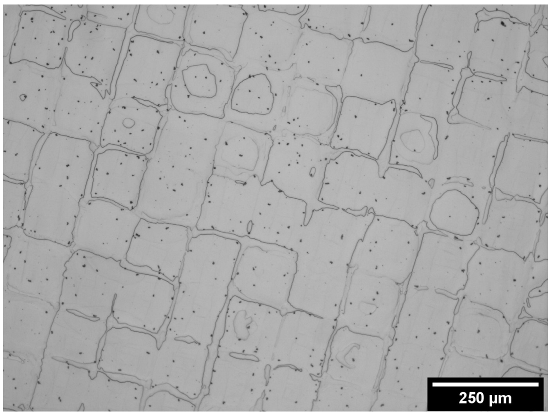
SR	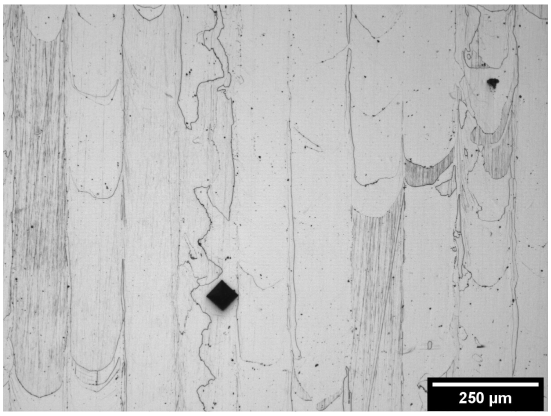	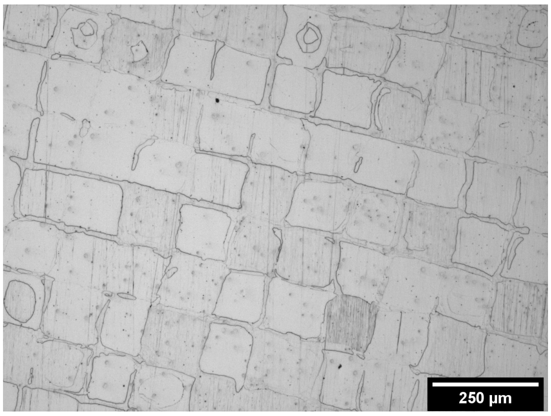
RA	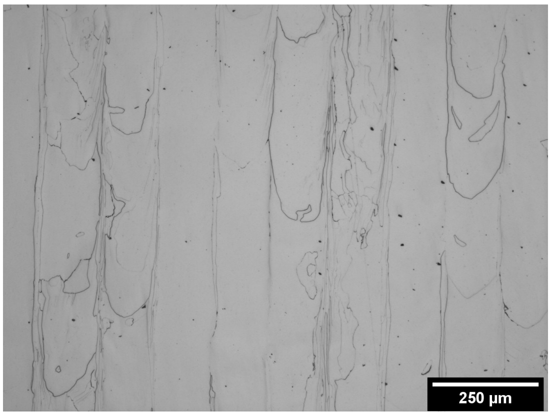	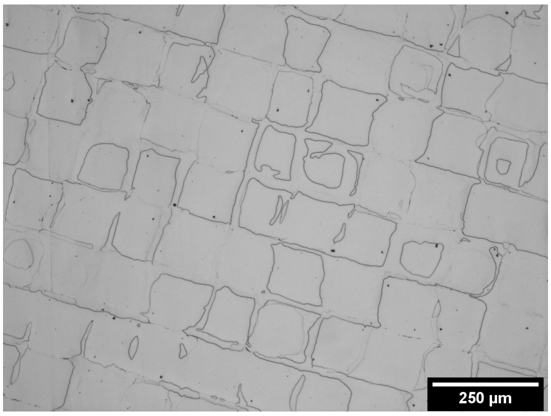

3.3.2 Fe-6.5Si alloy

With a special focus on eliminating the characteristic cracking of this Fe-6.5Si alloy a similar strategy was followed to obtain the optimised PBF-LB parameters for the Fe-6.5Si alloy. The best parameters in this alloy would mean a small crack density and high relative density, something that couldn't be fully achieved. As was explained, several methods were tested to observe their influence on the cracking, namely trying to reduce the energy density applied and, consequently, increasing the cooling rate trying to prevent the formation of the ordered phases. Figure 3.18 shows the relation between the crack density and the energy input (Figure 3.18 (a)) and the relative density (Figure 3.18 (b)) for the samples with CW and MW, with different focus position such as, F+5 and F-5 and with double melting strategy (DM). The optimised PBF-LB process parameters for the Fe-6.5Si was obtained in sample 23: VED = 83.3 J/mm^3, P = 175 W, v = 500 mm/s and h = 0.14 mm, continuous wave with the focal point in the powder layer ($z = 0$) and no double melting.

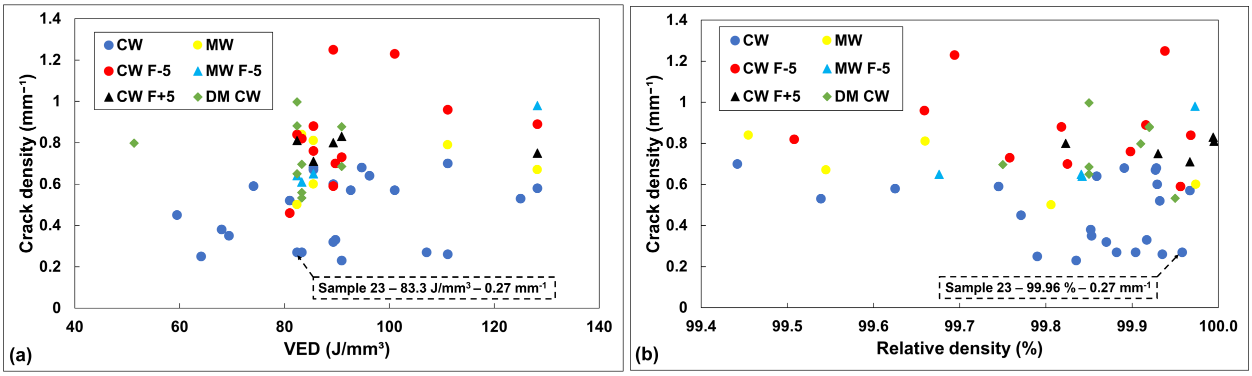

Figure 3.18: **(a)** Crack density vs VED and **(b)** crack density vs relative density of the Fe-6.5Si samples with different building conditions.

Samples were also produced with the Fe-6.5Si pre-alloyed powder (m4p) and with 0.05 wt.% addition of boron. These samples achieved a crack density of 0.31 and 0.29 mm^{-1}, respectively, being noticed that the change in powder help with the building process, but the crack density remained similar to the obtained with the powder mixture prepared from the pure elements.

Furthermore, Figure 3.18 shows that the attempt to reduce the energy and change the production process didn't improve the crack density of the Fe-6.5Si alloy. Instead, the cracking increased with several of these techniques. The double melting strategy increase the energy input and probably resulting in even more condition for the brittle ordered phases to form. The defocused laser, a characteristic that decreases the energy input also generates more cracking than the original production with a focus laser. In a general way, it is observed that increasing the VED increases the crack density of the samples for the Fe-6.5Si alloy. On the contrary, lower energies, which increase the already high cooling rates of PBF-LB, did not prevent the formation of the ordered phases and the correspondent cracking. The samples showed diverse types of cracks and in every direction, some along the building direction others in the scanning direction. Figure 3.19 shows some examples of cracks observed in these Fe-6.5Si alloy.

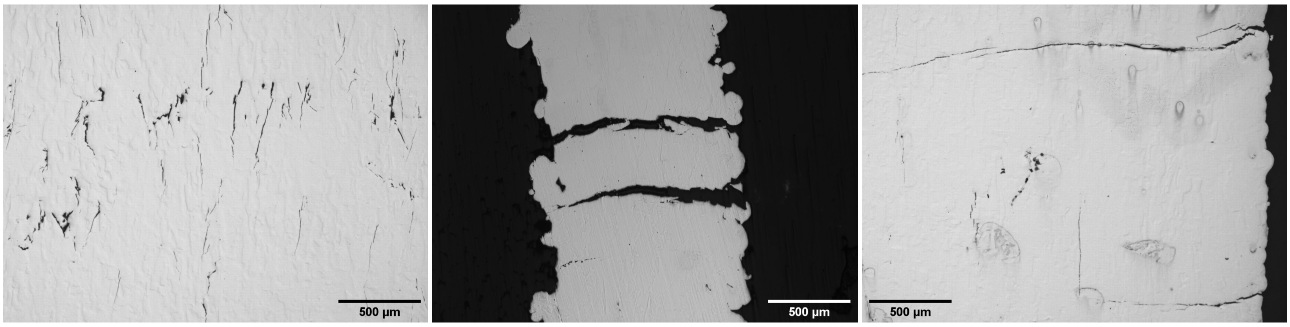

Figure 3.19: Example of cracks observed in the Fe-6.5Si samples.

3.3.3 Chemical microanalysis with SEM-EDS

The chemical composition of produced samples of Fe-3.5Si, Fe-6.5Si and Fe-6.5Si-0.05B were performed in the SEM with the EDS technology. Table 3.7 presents the weighted percentages of each element for the denser M67 sample of each type. The content of silicon are all slightly above the intended. In addition, the boron content is different than the one expected and cannot be considered correct due to the limited resolution of the EDS technique to detect light elements [129]. The spectrum of each sample measured is presented in Appendix B, Figures B.11, B.12, B.13 and B.14, respectively.

Table 3.7: Semi-quantitative EDS analysis of iron, silicon and boron in samples of the Fe-Si alloy.

Element	**Fe-3.5Si**	**Fe-6.5Si Mix**	**Fe-6.5Si m4p**	**Fe-6.5Si-0.05B**
Fe	95.74%	92.44%	92.30%	90.58%
Si	3.58%	6.73%	7.03%	6.75%
B	-	-	-	2.07%

3.4 Magnetic properties and hardness

The magnetic properties of the Fe-3.5Si and Fe-6.5Si alloys are described by their hysteresis loops. The relative density, roughness R_a and the crack density (for high Si content samples) will be presented for each of the samples used for the measurements. Note that the results presented are for sample produced by PBF-LB with the optimised parameters using the Meander scanning strategy.

3.4.1 Fe-3.5Si alloy

The first scanning strategy of the Fe-3.5Si alloy analysed was the M67, which achieve the highest relative density of this cylinder samples and the hysteresis curve is presented in Figure 3.20.

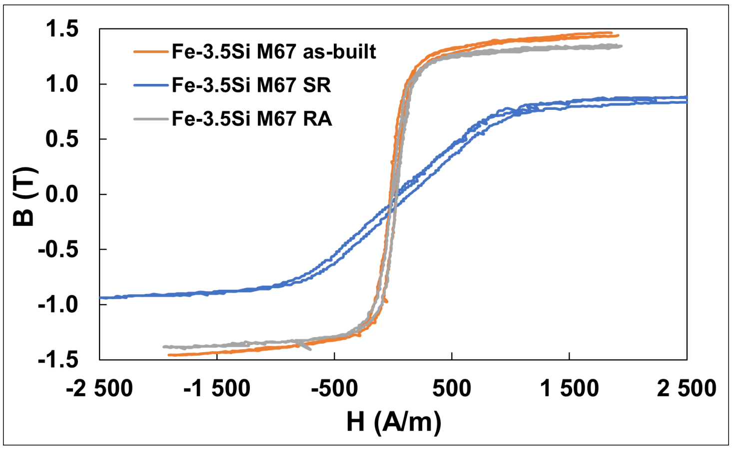

Figure 3.20: Magnetic hysteresis loop of cylinders of Fe-3.5Si alloy produced by PBF-LB with Meander 67° scanning strategy for different thermal-history conditions (as-built, SR and RA).

SR sample showed the worst magnetic hysteresis curve for this scanning strategy. It is observed that its curve is much broader and smaller, with a low slope for a soft magnetic material of this type. The principal magnetic parameters obtained using the M67 hysteresis loops are presented in Table 3.8. The values confirm that the SR is the worst sample, almost duplicating the coercivity and reducing significantly the maximum induction. The sample without heat treatment (as-built) and with the RA heat treatment achieved similar results. The as-built sample has higher inductions and permeability, but the annealed sample shows smaller coercivity, which is important to reduce the hysteresis losses and, consequently, the power losses when used in electric motors. In terms of physical characteristics, every sample is very similar in terms of relative densities and surface roughness.

The Vickers hardness of the samples was measured in the building and scanning directions and Figure 3.21 shows the hardness maps in different directions for different heat treatments. It is seen that some regions present hardness as high as HV260 while in some parts of the border and nearby it, the Vickers hardness drop to around HV210. This smaller hardness near the border of the samples can be due to the proximity of the edge of the sample. This allows a deeper indentation because exists less bulk material underneath the indentation.

The Fe-3.5Si alloy samples were also produced with the Meander 0° scanning strategy and submitted to post-processing heat treatments. Figure 3.22 and 3.23 present the magnetic hysteresis curves and Vickers hardnesses maps, respectively. With this strategy it is observed that none of the samples achieved 1 T of induction, being a possible reason the presence of pores in the cylinders. The production scanning with no angle increment usually leads to an increase in pores compared with other strategies like M67, as seen before in the reduction of relative density. Also, the fact of the microstructure being elongated along the building direction induces

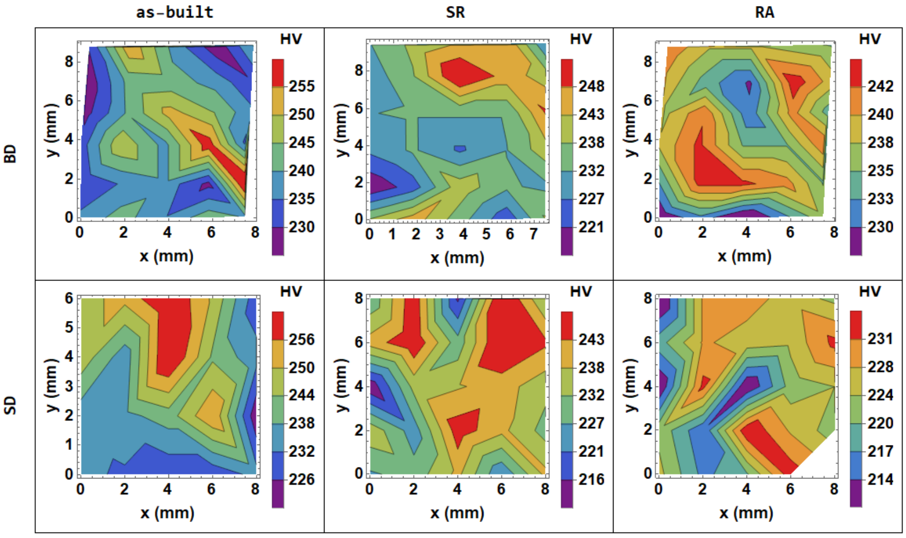

Figure 3.21: Vickers hardness map of cubes of Fe-3.5Si alloy produced by PBF-LB with Meander 67° scanning strategy for different thermal-history conditions (as-built, SR and RA). Top row images are in building direction and bottom row images at scanning direction.

a strong anisotropy and can difficult the magnetisation, because the field direction is perpendicular [66]. No major differences between each condition is observed in the samples, even the slopes of the curves are similar, being only slightly higher in the as-built sample with a slightly greater permeability and, consequently, maximum induction.

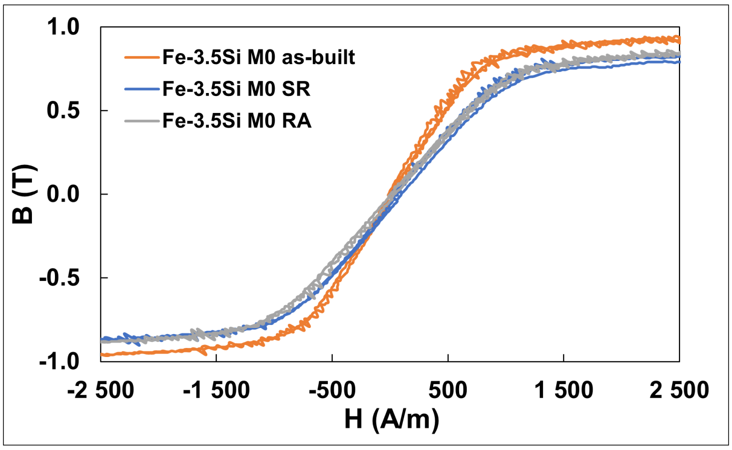

Figure 3.22: Magnetic hysteresis loop of cylinders of Fe-3.5Si alloy produced by PBF-LB with Meander 0° scanning strategy with different thermal-history conditions (as-built, SR and RA).

The hardness maps for the M0 samples in every heat treatment are presented in Figure 3.23 in both cross sections. Different regions of higher and lower hardness are obtained among the M0 samples, being noted in the SR sample in both directions of observation, values higher than predicted due to the stress removal. Like in M67, the smallest hardnesses are measured near the borders of the samples.

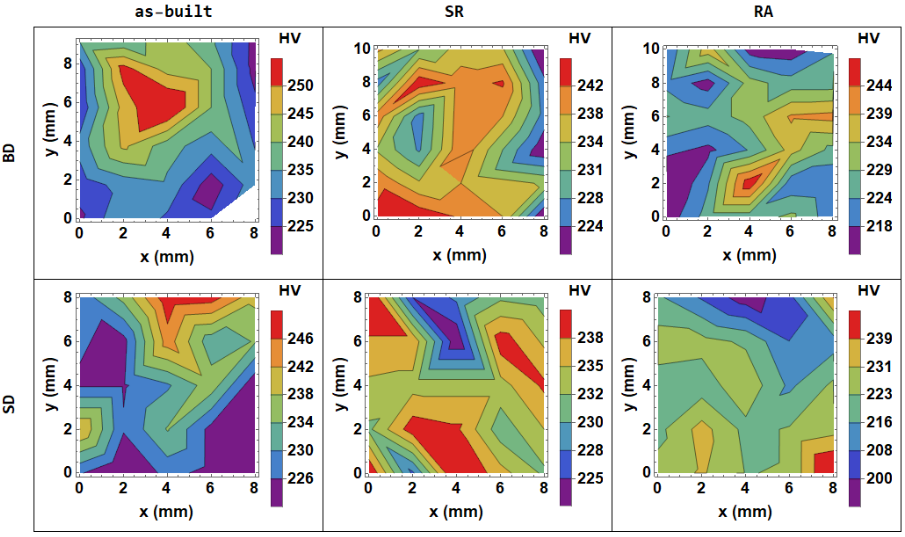

Figure 3.23: Vickers hardness map of cubes of Fe-3.5Si alloy produced by PBF-LB with Meander 0° scanning strategy for different thermal-history conditions (as-built, SR and RA). Top row images are in building direction and bottom row images at scanning direction.

Next, it will be presented the hysteresis curves and Vickers hardness maps of the Fe-3.5Si samples produced with the Meander 90° scanning strategy and the SR and RA post-processing heat treatments. The hysteresis curves obtained are presented in Figure 3.24, showing clear differences related to the thermal-history of the samples. With the M90 scanning strategy it was observed that the RA treatment increased the slope of the curve, allowing a higher magnetisation.

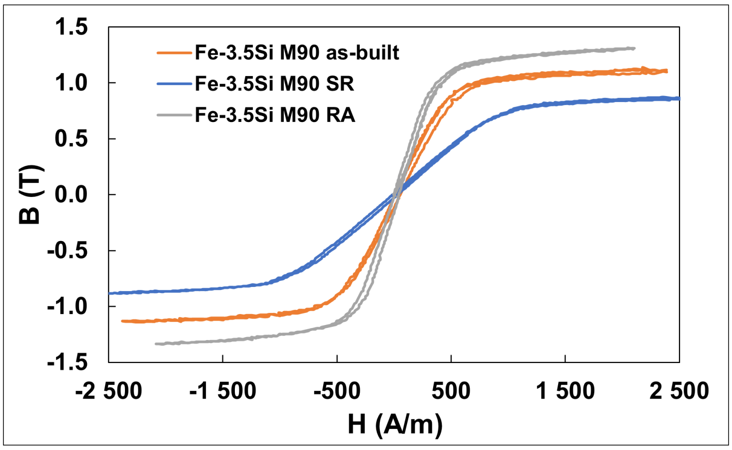

Figure 3.24: Magnetic hysteresis loop of cylinders of Fe-3.5Si alloy produced by PBF-LB with Meander 90° scanning strategy with different thermal-history conditions (as-built, SR and RA).

Figure 3.25 shows the hardness maps of the M90 strategy samples, in different directions and with several heat treatments applied. In those maps there is no preferred direction or zone for the higher or lower hardness. Only in the as-built BD and RA SD samples higher than usual hardness values are measured.

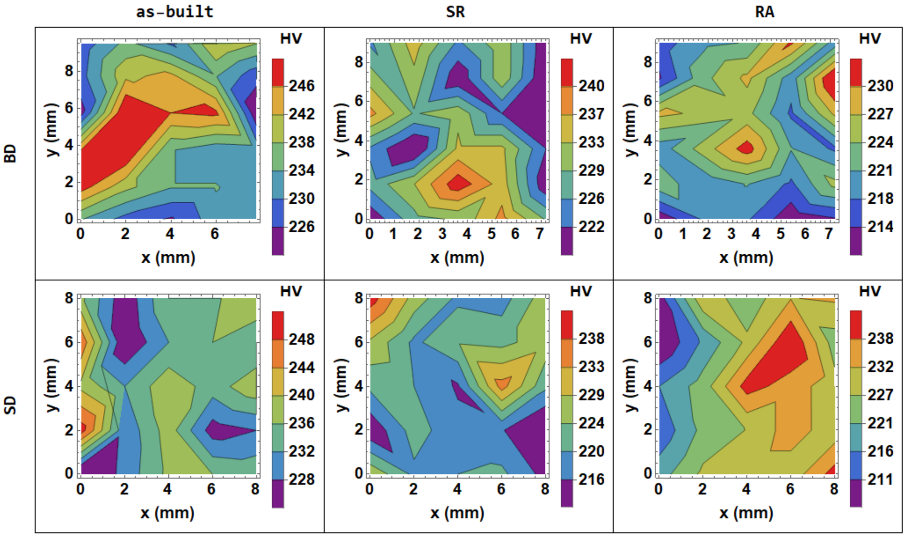

Figure 3.25: Vickers hardness map of cubes of Fe-3.5Si alloy produced by PBF-LB with Meander 90° scanning strategy for different thermal-history conditions (as-built, SR and RA). Top row images are in building direction and bottom row images at scanning direction.

Table 3.8: Magnetic properties of the Fe-3.5Si alloys produced by PBF-LB with the Meander 67°, 0° and 90° scanning strategies. The magnetic parameters are saturation induction B_s, coercivity H_c and relative permeability μ_r. Important physical properties are also presented, such as the relative density ρ_{rel} and average roughness R_a.

Sample	B_s **(T)**	H_c **(A/m)**	μ_r	ρ_{rel} **(%)**	R_a **(μm)**
M67 as-built	1.46	26.1	5350.6	99.75	12.62
M67 SR	0.92	41.2	731.3	99.70	10.44
M67 RA	1.38	23.0	4522.1	99.97	12.50
M0 as-built	0.95	24.6	865.6	99.35	9.38
M0 SR	0.87	49.8	584.2	99.91	12.51
M0 RA	0.89	17.5	539.4	99.95	12.07
M90 as-built	1.14	24.9	1437.4	99.53	14.67
M90 SR	0.88	22.4	662.1	99.94	9.77
M90 RA	1.33	20.2	1635.3	99.92	11.16

The best and worst coercivity values obtained for the Fe-3.5Si alloy produced by PBF-LB is observed in the samples with M0 scanning strategy, with RA and SR, respectively. The fact that the sample with lowest relative density (M0) obtained the smallest coercive field (17.5 A/m) was unexpected. Analysing other magnetic properties, M0 did not reach significantly good results, obtaining smaller inductions and permeability compared to the M67 and M90 scanning strategies.

Considering the reference values of Table 1.2, it is observed that the permeability μ_r reach higher values than expected, only in the SR state lower values below the theoretical, 1000 were achieved. This high μ_r values are not followed by high B_s values. The B_s value are also lower than the expected value of 2 T (considering Table 1.2), being sometimes not even half that value. But it is observed a direct proportionality between those two properties. In the as-built and RA thermal-history condition both values are significantly bigger than in the SR. Because the production parameters are optimised for a cube and not a cylinder, the relative density and surface roughness were not the same, and possibly, reduce the properties measured. The domain alignment is influenced by the relative density, whereas pores difficult this process. High surface roughness may decrease the permeability of the samples.

Fixing the heat treatment and changing the strategy of the samples was also performed to study its effects, Figure 3.26 shows the hysteresis loops. It is possible to see that the RA heat treatment does not improve much the magnetic properties of the samples. It is observed that only the coercivity is decreased with recrystallisation annealing, which could help decreasing the hysteresis area and power losses. But the saturation induction and permeability maintain similar or get smaller values. Observing the figures, it is clear that the M67 scanning strategy shows better results in terms of B_s and μ_r than the M0 and M90, which enables better electric efficiency. Compared with the M67 scanning strategy, the M90 achieve smaller coercivities, representing fewer power losses, even if it is not reaching the same efficiencies as M67.

Hardness Vickers comparison for the Fe-3.5Si alloy

With the average of each Hardness Vickers map the bar chart from Figure 3.27 is obtained, where is presented the hardness in different directions, for several heat treatments and scanning strategies. A decrease is noticed in the hardness of the material, from the most dense material, M67 to the other strategies. It is also understood that from the as-built state to the RA, passing through the SR, the hardness of the material decreases, being independent of the building strategy. This is because the stresses of the production are removed by the heat treatments,

Table 3.9: Average Vickers hardness of the Fe-3.5Si samples produced with Meander 67°, 0° and 90° in several thermal-history conditions, considering both cross sections.

Scanning strategy	**as-built**	**SR**	**RA**
M67	239 ± 10.2	235 ± 9.4	230 ± 9.3
M0	233 ± 9.0	234 ± 6.7	224 ± 10.0
M90	235 ± 7.6	225 ± 7.7	224 ± 8.3

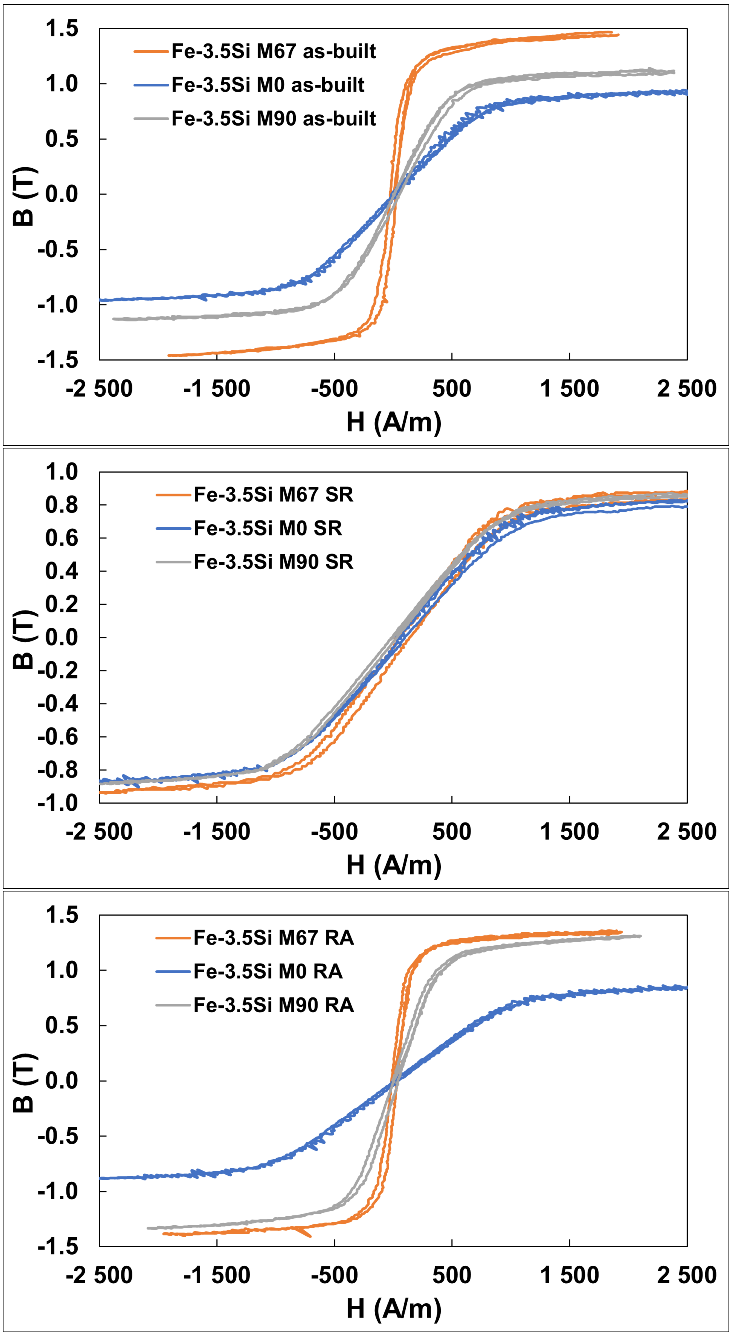

Figure 3.26: Magnetic hysteresis loop of cylinders of Fe-3.5Si alloy produced by PBF-LB with Meander 67°, 0° and 90° scanning strategies divided by thermal-history conditions (as-built, SR and RA).

reducing the hardness of the material.

Unlike the other scanning strategies, an increase in the hardness is observed in the M0 sample after the stress relief heat treatment, instead of the usual decrease. The reason behind this hardening may also explain the increase of the coercive field of this sample of 50 A/m, which is a

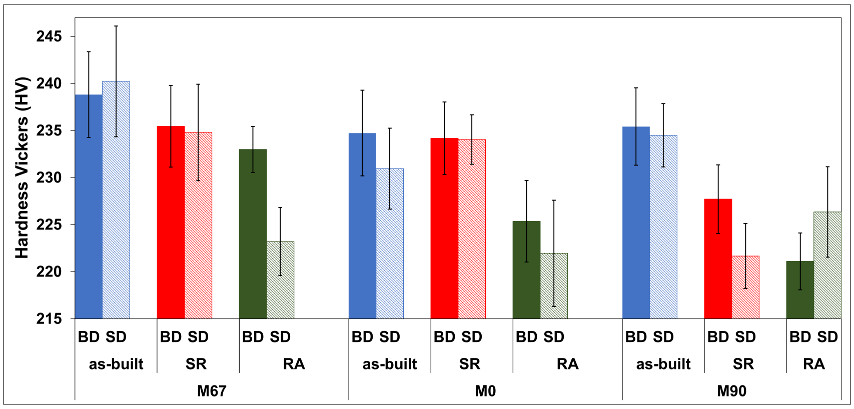

Figure 3.27: Hardness Vickers average values of the Fe-3.5Si samples with Meander 67°, 0° and 90°, divided by thermal-history and direction of analysis.

high value and not usual in soft magnetic materials [1,60]. The mechanism behind this behaviour is not clear. Another characteristic that can be taken from the hardness is the predominance of slightly higher hardnesses in the building direction, only the M67 as-built sample and M90 RA have a higher hardness in the scanning direction, and the M0 SR achieves the same hardness in both analysing directions. It is not completely known why this happen, but the scanning direction with the perpendicular epitaxial grain growth could lead to smaller hardness [130]. It is possible to see the overall decrease in hardness with the heat treatments applied. In each heat treatment, the M67 scanning strategy always reaches the highest hardness, which could be due to its more randomly oriented grains, combined with its high relative densities.

3.4.2 Fe-6.5Si alloy

The hysteresis loops of the two samples of Fe-6.5Si produced with PBF-LB with the pre-alloyed powder (m4p) are presented in Figure 3.28. The magnetic properties extracted from the hysteresis curves are presented in Table 3.10. The analysis also shows the crack density of each sample. The cracks can have an influence in the resistivity of the material, which influences the magnetic properties. A decrease in the minimum coercivity is observed, from the Fe-3.5Si to the Fe-6.5Si

Table 3.10: Magnetic properties of the Fe-6.5Si alloys produced by PBF-LB with the Meander 67° scanning strategy. The magnetic properties are saturation induction B_s, coercivity H_c and relative permeability μ_r. Important physical properties are also presented, such as the relative density ρ_{rel} and crack density ρ_{cracks}.

Sample	B_s **(T)**	H_c **(A/m)**	μ_r	ρ_{rel} **(%)**	ρ_{cracks} **(mm^{-1})**
Fe-6.5Si M67 m4p	0.91	27.5	1179.8	99.99	0.55
Fe-6.5Si-0.05B M67	1.14	15.5	1522.0	99.95	0.41

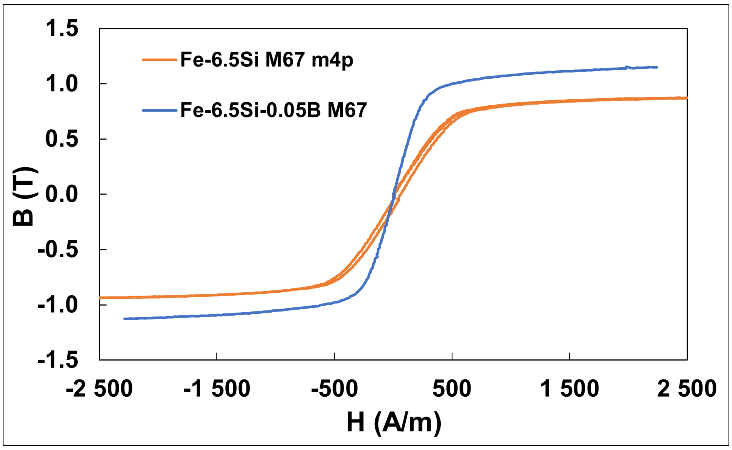

Figure 3.28: Hysteresis loop of Meander 67° cylinders for Fe-6.5Si using the m4p powder and Fe-6.5Si-0.05B using also the m4p powder joined with boron.

alloy, due to the silicon increase, which enhances the electrical resistivity of the material and results in a smaller hysteresis area. Compared with values from the literature [77], 16 A/m, may be considered a small coercive field, and with the Fe-6.5Si-0.05B sample was obtained an even smaller coercivity, which will guide to less hysteresis losses, 15.5 A/m.

Another important observed results is the reduction of the saturation induction: the samples of Fe-3.5Si alloys with lower silicon content presented higher inductions and magnetisations, allowing higher efficiencies. This result shows that this type of material, Fe-6.5Si, has the potential to achieve even greater magnetic values when the cracking susceptibility is overcome. The as-built Fe-6.5Si specimens tested have a crack density as low as 0.41 mm^{-1}, not counting possible micro cracks that are not seen in the optical microscope. The Fe-6.5Si M67 sample show poorer magnetic properties than the Fe-3.5Si M67, with higher coercive field and smaller maximum induction and permeability. The addition of boron in the Fe-6.5Si-0.05B M67 sample improved the magnetic properties and reduced the cracking observed when compared with the Fe-3.5Si M67 and Fe-6.5Si M67 samples. Among these properties, only the permeability of the as-built Fe-3.5Si M67 sample was higher than in the Fe-6.5Si-0.05B M67 sample.

The hardness maps of the Fe-6.5Si samples produced with PBF-LB with Meander 67° scanning strategy are presented in Figure 3.29. For these samples, the Vickers hardness was tested only in the building direction, since it was previously observed that the scanning direction hardness is slightly smaller when compared with the building direction. It is noted in the samples produced with Fe-6.5Si powder mixture a part of the map is not showed due to incorrectly measured indentations. The top corners indentation points were considered outliers. The average hardness of each sample hardness map is presented in Table 3.11. An increase in the hardness is observed in samples produced with the pre-alloyed Fe-6.5Si powder from m4p powder and

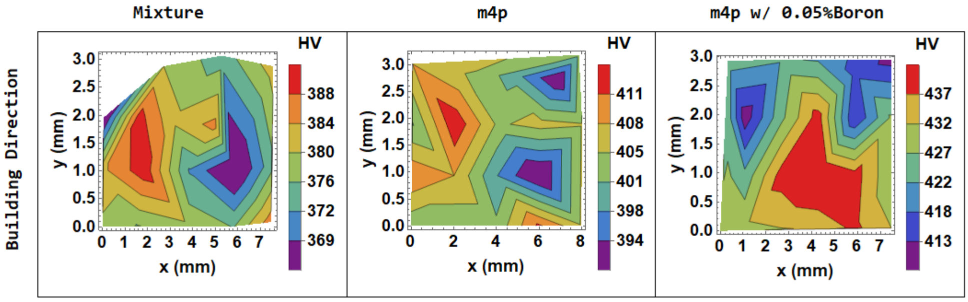

Figure 3.29: Map of Hardness Vickers of Meander 67° cubes with thin walls for different pieces built, Fe-6.5Si mixture, Fe-6.5Si m4p and Fe-6.5Si-0.05B m4p in the building direction.

Table 3.11: Hardness Vickers values for each of the Fe-6.5Si M67 samples built in the as-built state.

	Hardness Vickers (HV)
Fe-6.5Si M67 mixture	378 ± 7.6
Fe-6.5Si M67 m4p	404 ± 6.4
Fe-6.5Si-0.05B M67	428 ± 9.2

with the addition of 0.05 wt.% of boron. Therefore, the small addition of boron increased the hardness of the Fe-6.5Si alloy. The segregation of boron improves the grain boundary cohesion by reducing the grain size, allowing a hardening of iron alloys [114]. Comparing with the Fe-3.5Si samples these Fe-6.5Si samples reach higher hardnesses. The silicon has a known strengthening effect in the ferrite phase [131].

3.5 Influence of grain size

The following analysis is performed in the scanning direction since the grains are very elongated in the building direction and knowing the exact border is difficult. Rotational electric machines require non-orientated grains, especially perpendicular to the rotating axis, the scanning direction. With the optical micrographs of the samples after the chemical etching, the size of the grains was measured and compared between each heat treatment and scanning strategy, in the scanning direction. The average grain area is presented in Figure 3.30.

The grains show a tendency to be bigger in the samples after the recrystallisation annealing heat treatment. Nonetheless, this feature was also dependent on the scanning strategy. The M67 samples show a decrease in the grain size from the as-built state after recrystallisation annealing. The grains in the samples produced with the M0 scanning strategy grains are much coarser than in the other strategies grains. There are no angle increment in the laser scan, forming the grain along the passage of the laser (always in the same 2D position), making the

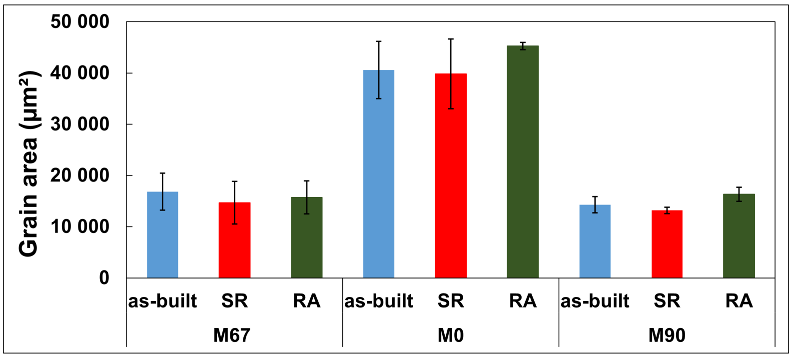

Figure 3.30: Average grain area, given in μm^2, of the etched Fe-3.5Si samples, with all the heat treatments done, measured in the scanning direction.

grains very elongated. The bigger the grains, the harder it is to magnetise the domains of the material. For that reason, this strategy did not reach the best magnetic results. The M90 strategy, as expected, shows a slight grain growth with the RA treatment.

The average aspect ratio of the grains was also measured. The M0 scanning strategy resulted in grains with an aspect ratio of 2.5, whereas the M67 strategy resulted in an aspect ratio of 1.3 and the M90 strategy a grain aspect ratio of 1.1. These values could be easily understandable because the M0 usually results in highly columnar grains, characterised by higher aspect ratios. The M67 samples have the most random grain morphology and size, whereas the M90 form grains with square shapes, which leads to aspect ratios near 1 (case of a perfect square).

3.6 Analysis of power losses

Measuring the area inside the hysteresis curves gives the hysteresis losses. Figure 3.31 shows for each Fe-3.5Si sample the hysteresis loss, given in W/kg. The minimum power losses measured for this type of alloy in the literature is 2.2 W/kg [77] and no hysteresis losses measured are

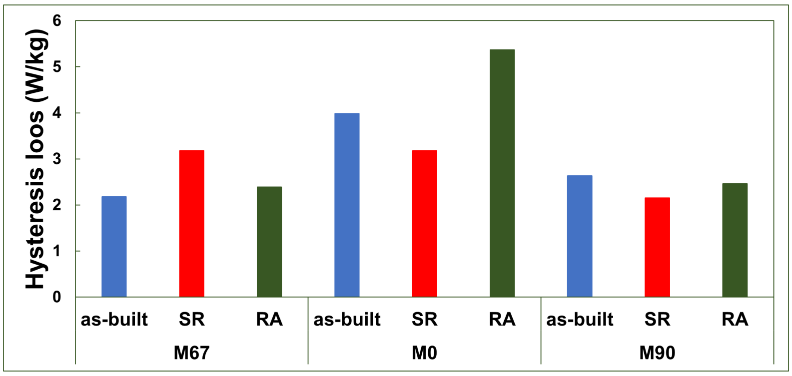

Figure 3.31: Hysteresis losses of the Fe-3.5Si samples, obtained from the area of the hysteresis loops.

significantly lower than this. The lowest values measured are 2.15 W/kg in M90 SR and 2.18 W/kg in M67 as-built, only considering this type of losses, so the power loss of the sample would be slightly higher. Measured from Figure 3.28, the hysteresis losses of the Fe-6.5Si alloys are:

- **Fe-6.5Si M67 m4p:** 1.88 W/kg and **Fe-6.5Si-0.05B M67:** 2.11 W/kg

The addition of boron increases the losses in the hysteresis based losses. This slight increase would not be predicted, especially after the coercivity decreases significantly, but could be enhanced by the higher maximum induction obtained, increasing the hysteresis area. But comparing with the Fe-3.5Si, it is seen that all the losses are smaller for more silicon content in the alloy. Silicon is known to improve the magnetic properties, but there are challenges for manufacturing the high silicon content alloys due to the low ductility and cracking susceptibility. The samples produced from the Fe-6.5Si pre-alloyed powder shows the lowest hysteresis losses of 1.88 W/kg, being significantly smaller than the minimum value observed in the literature.

Comparing the scanning strategies, it is seen that the M0 has much higher losses. This is related to the higher porosity, bigger grains and poor magnetic properties, that enhanced the hysteresis losses. The M67 and M90 scanning strategies, resulted in similar results, near the minimum power losses reported in the literature. Finally, the applied heat treatments do not reduce the losses of the samples and should be further investigated.

4

Conclusions

This work aimed to investigate the powder bed fusion technology metal AM technology to produce iron-silicon-based soft magnetic materials. In addition, the effect of post-processing heat treatments on the microstructure and magnetic properties of the Fe-3.5Si and Fe-6.5Si alloys are considered.

The coercive fields obtained were as low as 15.5 A/m, a relatively small coercive field measured for this type of materials. This value was measured for the high silicon Fe-6.5Si alloy, which gives better magnetic properties, compared to the Fe-3.5Si alloy, which showed a coercivity of 17.5 A/m.

An important characteristic of electric machines is the power losses, which are required to be as small as possible. The hysteresis losses were possible to be measured and compared considering the different laser scanning strategies in PBF-LB and heat treatments. It was seen that there is a relation between the strategy, that results in a higher relative density and better magnetic materials. The M67 and M90 scanning strategies showed the best results in terms of magnetic properties, with higher inductions and lower coercivities, since those strategies resulted almost fully densified samples. In addition, the M67 strategy formed a microstructure with grains showing random morphology, size and without a preferred orientation, which helps with the permeability and domain alignment.

It is observed that the M67 is the strategy that generates the best magnetic properties with the M90 coming close, and in some cases surpassing the M67 scanning, for example, in the as-built state the coercivity is better (24.9 A/m). The recrystallisation treatment also reduces the coercivity, allowing the M67 to reach 23.0 A/m and the M90 20.2 A/m. But the heat treatments have the problem of decreasing the induction, which could reduce the efficiency of electric machines.

The cracking susceptibility of the Fe-6.5Si alloys was once again proved in the present work, even with the addition of 0.05 wt.% of boron. The cracking in this high silicon content alloy occurred in all samples produced by PBF-LB, although crack densities varied with the process parameters and scanning strategy.

Finally, it is seen that the Fe-6.5Si alloy, although highly brittle, shows better magnetic properties and if produced without defects may result in components of electric machines made of a soft magnetic material with small coercivities, and consequently, fewer hysteresis losses, increasing the overall efficiency of the machine.

Analysing the objectives previously presented, it is seen that the majority of them have been achieved. From the understanding of the concepts used to the design of samples to build and optimise the post-processing strategies for those samples, all this objectives have been reached. The preparation and optimisation of the alloys to be produced was only been fully completed with the Fe-3.5Si. But for both alloys, three out of the four major properties for soft magnetic materials were measured, being observed several influences of the production process and heat treatments.

4.1 Future work

Although this thesis achieves some important results, the work in this area is not finished, especially for the iron alloy with higher silicon content. This material is characterised by its cracking susceptibility, being one of the main challenges, to eliminate those cracks. This could be done by a change in the PBF-LB process parameters or in the chemical composition. Elements like copper or nickel are possible candidates to add to the alloy because could theoretically prevent the formation of the brittle $D0_3$ and B_2 ordered phases. Among the changes that could be done in the PBF-LB process parameters, studying different laser beam scanning strategies, and changing the layer thickness and the powder bed temperature could reduce the cracking observed.

Some other properties can still be measured to achieve a better analysis of the alloys. The resistivity and Eddy currents losses would allow better comprehension of the magnetic properties obtained and influence that silicon and the process parameter have in the samples. In addition, X-ray computed tomography can be applied to the sample to understand pore size distribution.

Bibliography

[1] Tiismus, H.; Kallaste, A.; Vaimann, T. and Rassõlkin, A. State of the art of additively manufactured electromagnetic materials for topology optimized electrical machines. Additive Manufacturing 55. 2022.

[2] Boehm, A. and Hahn, I. Comparison of Soft Magnetic Composites (SMCs) and electrical steel. 2022.

[3] Pham, T.Q.; Mellak, C.; Suen, H.; Boehlert, C.J.; Muetze, A.; Kwon, P. and Foster, S.N. Binder Jet Printed Iron Silicon with Low Hysteresis Loss. In Proceedings of the 2019 IEEE International Electric Machines Drives Conference. 2019.

[4] Magnetic Materials: Soft Magnets. University of Birmingham. `https://www.birmingham.ac.uk/Documents/college-eps/metallurgy/research/Magnetic-Materials-Background/Magnetic-Materials-Background-10-Soft-Magnets.pdf`

[5] Gibson, I.; Rosen, D. and Stucker, B. Additive Manufacturing Technologies. New York: Springer. 2015.

[6] ISO/ASTM 52900-2018. Additive manufacturing — General principles Terminology.

[7] Milewski, J.O. Additive Manufacturing of Metals. New York: Springer. 2017.

[8] Linxi, Z.; Quanzhan, Y.; Guirong, Z.; Fangxin, Z.; Gang, S. and Bo, Y. Additive manufacturing technologies of porous metal implants. China Foundry. 2014.

[9] Atzeni, E.; Iuliano, L.; Marchiandi, G.; Minetola, P.; Salmi, A.; Bassoli, E.; Denti, L. and Gatto, A. Additive manufacturing as a cost-effective way to produce metal parts. High Value Manufacturing: Advanced Research in Virtual and Rapid Prototyping. In Proceedings of the 6th International Conference on Advanced Research in Virtual and Rapid Prototyping, Leiria, Portugal, 2013.

[10] Killi, S. Additive Manufacturing: Design, Methods, and Processes. 2017.

[11] Martina, F. Investigation of methods to manipulate geometry, microstructure and mechanical properties in titanium large scale Wire+Arc Additive Manufacturing. PhD. Cranfield University. 2014.

[12] Maiman, T.H. Stimulated optical radiation in ruby. Nature 187. 1960.

[13] Brandt, M. Laser Additive Manufacturing Materials, Design, Technologies, and Applications. Woodhead Publishing Series in Electronic and Optical Materials: Number 88. 2017.

[14] Song, X.; Zhai, W.; Huang, R.; Fu, J.; Fu, M. and Li, F. Metal-Based 3D-Printed micro parts & structures. Materials Science and Materials Engineering, Elsevier. 2020.

[15] Rigo, O. and Engel, C. Selective Laser Melting versus Electron Beam Melting. 2013. http://www.slideshare.net/carstenengel/selective-laser-melting-versus-electron-beam-melting.

[16] DebRoy, T.; Wei, H.L.; Zuback, J.S.; Mukherjee, T.; Elmer, J.W.; Milewski, J.O.; Beese, A.M.; Wilson-Heid, A.; De, A. and Zhang, W. Additive manufacturing of metallic components – process, structure and properties. Progress in Materials Science. 2017.

[17] Oliveira, J.P.; LaLonde, A.D. and Ma, J. Processing parameters in laser powder bed fusion metal additive manufacturing. Materials and Design. 2020.

[18] AM FIELD GUIDE COMPACT. Mesago. Edition Deutsch and English. 2020.

[19] Vock, S.; Klöden, B.; Kirchner, A.; Weißgärber, T. and Kieback, B. Powders for powder bed fusion: a review. Additive Manufacturing. 2019.

[20] Abd-Elaziem, W.; Elkatatny, S.; Abd-Elaziem, A.; Khedr, M.; El-baky, M.A.A.; Hassan, M.A.; Abu-Okail, M.; Mohammed, M.; Järvenpää, A.; Allam, T. and Hamada, A. On the current research progress of metallic materials fabricated by laser powder bed fusion process: a review. Journal of Materials Research and Technology. 2022.

[21] Letenneur, M.; Kreitcberg, A. and Brailovski, V. Optimization of Laser Powder Bed Fusion Processing Using a Combination of Melt Pool Modeling and Design of Experiment Approaches: Density Control. Journal of Manufacturing and Materials Processing. 2019.

[22] Pfaff, A.; Jäcklein, M.; Schlager, M.; Harwick, W.; Hoschke, K. and Balle, F. An Empirical Approach for the Development of Process Parameters for Laser Powder Bed Fusion. Materials. 2020.

[23] Bassoli, B.; Sola, A.; Celesti, M.; Calcagnile, S. and Cavallini, C. Development of Laser-Based Powder Bed Fusion Process Parameters and Scanning Strategy for New Metal Alloy Grades: A Holistic Method Formulation. 2018.

[24] Sames, W.J.; List, F.A.; Pannala, S.; Dehoff, R.R. and Babu, S.S. The metallurgy and processing science of metal additive manufacturing. International Materials Reviews. 2016.

[25] Aboulkhair, N.T.; Everitt, N.M.; Ashcroft, I. and Tuck, C. Reducing porosity in AlSi10Mg parts processed by selective laser melting, Additive Manufacturing 1-4. 2014.

[26] Gong, H.; Rafi, K.; Starr, T. and Stucker, B. The Effects of Processing Parameters on Defect Regularity in Ti-6Al-4 V Parts Fabricated By Selective Laser Melting and Electron Beam Melting. 2013.

[27] Renishaw Material Editor. Renishaw. 2020.

[28] Letenneur, M.; Brailovski, V.; Kreitcberg, A.; Paserin, V. and Bailon-Poujol, I. Laser powder bed fusion of water-atomized iron-based powders: Process optimization. J. Manuf. Mater. Process. 2017.

[29] Yang, K.V.; Rometsch, P.; Jarvis, T.; Rao, J.; Cao, S.; Davies, C. and Wu, X. Porosity formation mechanisms and fatigue response in Al-Si-Mg alloys made by selective laser melting. Mater. Sci. Eng. A 2018.

[30] AlMangour, B.; Grzesiak, D.; Borkar, T. and Yang, J.M. Densification behavior, microstructural evolution, and mechanical properties of TiC/316L stainless steel nanocomposites fabricated by selective laser melting. Mater. Des. 2018.

[31] Sánchez-Amaya, J.M.; Pasang, T.; Amaya-Vazquez, M.R.; Lopez-Castro, J.D.D.; Churiaque, C.; Tao, Y.; Botana Pedemonte, F.J. Microstructure and Mechanical Properties of Ti5553 Butt Welds Performed by LBW under Conduction Regime. Metals. 2017.

[32] Cheng, B.; Shrestha, S. and Chou, K. Stress and deformation evaluations of scanning strategy effect in selective laser melting. Additive Manufacturing 12. 2016.

[33] Kim, S.I. and Hart, A.J. A spiral laser scanning routine for powder bed fusion inspired by natural predator-prey behaviour. Virtual and Physical Prototyping. 2022.

[34] Bean, G.E.; Witkin, D.B.; McLouth, T.D.; Patel, D.N. and Zaldivar, R.J. Effect of laser focus shift on surface quality and density of Inconel 718 parts produced via selective laser melting. Additive Manufacturing 22. 2018.

[35] Cullity, B.D. and Graham, C.D. Introduction to Magnetic Materials. Wiley. 2009.

[36] Purcell, E.M. and Morin, D.J. Electricity and Magnetism. Cambridge University Press. 2013.

[37] Wills, B.A. and Finch, J.A. Magnetic and Electrical Separation. Wills' Mineral Processing Technology. 2016.

[38] Gonano, C.A.; Zich, R.E. and Mussetta, M. Definition for Polarization P and Magnetization M Fully Consistent with Maxwell's Equations. Progress in Electromagnetics Research B. 2015.

[39] Jackson, J.D. Classical Electrodynamics. New York: Wiley. 1998.

[40] Chikazumi, S. Physics of Ferromagnetism. 1997.

[41] Bertotti, G. Hysteresis in Magnetism: For Physicists, Materials Scientists, and Engineers. Elsevier Science. 1998.

[42] Mørup, S.; Hansen, M.F. and Frandsen, C. Magnetic Nanoparticles. Comprehensive Nanoscience and Nanotechnology. 2019.

[43] Feynman, R.P.; Leighton, R.B. and Sands, M. The Feynman Lectures on Physics, Vol. II. US: California Inst. of Technology. 1963.

[44] McHenry, M.E. and Laughlin, D.E. 19 - Magnetic Properties of Metals and Alloys. Physical Metallurgy. 2014.

[45] Zurek, S. Characterisation of Soft Magnetic Materials Under Rotational Magnetisation. 2018.

[46] Indeck, R.S. and Muller, M.W. Magnetic Recording Measurements. Encyclopedia of Materials: Science and Technology. 2002.

[47] Coey, J.M.D. Magnetism and Magnetic Materials. Cambridge. 2009.

[48] Marghussian, V. Magnetic Properties of Nano-Glass Ceramics. Nano-Glass Ceramics. 2015.

[49] Krings, A.; Cossale, M.; Tenconi, A.; Soulard, J.; Cavagnino, A. and Boglietti, A. Characteristics comparison and selection guide for magnetic materials used in electrical machines. In Proceedings of the 2015 IEEE International Electric Machines Drives Conference. 2015.

[50] Chaudharya, V.; Mantri, S.A.; Ramanujan, R.V. and Banerjee, R. Additive manufacturing of magnetic materials. Progress in Materials Science. 2020.

[51] Coey, J.M.D. Hard Magnetic Materials: A Perspective. 2011.

[52] Soft Magnetics Application Guide. *Arnold*. 2003.

[53] Magnetic Materials. *BrainKart*. https://www.brainkart.com/article/Magnetic-Materials_6809/.

[54] Littman, M. Iron and Silicon-Iron Alloys. IEEE Transactions on Magnetics. 1971.

[55] Hendricks, C.R.; Amarakoon, V.W.R. and Sullivan, D. Processing of manganese zinc ferrites for high-frequency switch-mode power supplies. 1991.

[56] Boll, R. Soft Magnetic Materials. Hanau, Germany. 1990.

[57] Schoppa, A. and Delarbre, P. Soft Magnetic Powder Composites and Potential Applications in Modern Electric Machines and Devices. 2014.

[58] Shokrollahi, H. and Janghorban, K. Soft magnetic composite materials (SMCs)

[59] Hultman, L.O. and Jack, A.C. Soft Magnetic Composites - Materials and Applications. Sweden and United Kingdom. 2003.

[60] Tong, C. Introduction to Materials for Advanced Energy Systems. Springer. 2018.

[61] Goll, D.; Schuller, D.; Martinek, G.; Kunert, T.; Schurr, J.; Sinz, C.; Schubert, T.; Bernthaler, T.; Riegel, H. and Schneider, G. Additive manufacturing of soft magnetic materials and components. Additive Manufacturing 27. 2019.

[62] Kittel, C. Introduction to Solid State Physics. John Wiley and Sons. 1986.

[63] Kotnala, R.K. and Jyoti Shah, J. Ferrite Materials. Handbook of Magnetic Materials. 2015.

[64] Bramfitt, B.L. and Benscoter, A.O. The Iron Carbon Phase Diagram. Metallographer's guide: practice and procedures for irons and steels. 2002.

[65] Lide, D.R. Magnetic susceptibility of the elements and inorganic compounds. Handbook of Chemistry and Physics. 2005.

[66] Electrical steels - Iron-Silicon Transformer Steels. Dierk Raabe.

[67] Thang Pham, T.; Kwon, P. and Foster, S. Additive Manufacturing and Topology Optimization of Magnetic Materials for Electrical Machines—A Review. Energies. 2021.

[68] Krings, A.; Boglietti, A.; Cavagnino, A. and Sprague, S. Soft Magnetic Material Status and Trends in Electric Machines. IEEE Trans. Ind. Electron. 2017.

[69] Plotkowski, A.; Pries, J.; List, F.; Nandwana, P.; Stump, B.; Carver, K. and Dehoff, R.R. Influence of scan pattern and geometry on the microstructure and softmagnetic performance of additively manufactured Fe-Si. Additive Manufacturing 29. 2019.

[70] Ashby, M.F. and Jones, D.R.H. Engineering Materials 2. Oxford: Pergamon Press. 1992.

[71] Fichte, R. Ferroalloys. Ullmann's Encyclopedia of Industrial Chemistry. Weinheim: Wiley-VCH.

[72] Lowrie, W. Fundamentals of Geophysics. Cambridge University Press. 2007.

[73] Buschowl, K.H.J. et al. Encyclopedia of Materials:Science and Technology. Elsevier. 2001.

[74] Jang, P.; Lee, B. and Choi, G. Effects of annealing on the magnetic properties of Fe–6.5%Si alloy powder cores. Magnetism and Magnetic Materials. 2008.

[75] Swann, P.R.; Grånäs, L. and Lehtinen, B. The B2 and DO3 Ordering Reactions in Iron-Silicon Alloys in the Vicinity of the Curie Temperature. Metal Sci. 1975.

[76] Garibaldi, M.; Ashcroft, I.; Hillier, N.; Harmon, S.A.C. and Hague, R. Relationship between laser energy input, microstructures and magnetic properties of selective laser melted Fe-6.9%wt Si soft magnets. Mater Charact. 2018.

[77] Garibaldi, M.; Ashcroft, I.; Lemke, J.N.; Simonelli, M. and Hague, R. Effect of annealing on the microstructure and magnetic properties of soft magnetic Fe-Si produced via laser additive manufacturing. Scripta Mater. 2018.

[78] Electrical Steel Market Outlook. Commodity Inside. 2020.

[79] Paltanea, G.; Manescu, V.;Stefanoiu, R.; Nemoianu, I.V. and Gavrila, H. Correlation between Magnetic Properties and Chemical Composition of Non-Oriented Electrical Steels Cut through Different Technologies. 2020.

[80] Sidor, Y. and Kovac, F. Contribution to modeling of decarburization process in electrical steels. 2005.

[81] von Goldbeck, O.K. Fe—Si Iron—Silicon. IRON—Binary Phase Diagrams. Springer, Berlin, Heidelberg. 1982.

[82] Ouyang, G.; Chen, X.; Liang, Y.; Macziewski, C. and Cui, J. Review of Fe-6.5 wt%Si high silicon steel—A promising soft magnetic material for sub-kHz application. Journal of Magnetism and Magnetic Materials. 2019.

[83] Starke, U.; Schardt, J.; Weiss, W.; Meier, W.; Polop, C.; de Andres, P.L. and Heinz, K. Structural and compositional reversible phase transitions on low-index Fe3Si surfaces. Europhysics Letters. 2001.

[84] Kubaschewski, O. Iron Binary Phase Diagrams. Springer. Berlin. 1982.

[85] Gutfleisch, O.; Willard, M.A.; Brück, E.; Chen, C.H.; Sankar, S.G. and Liu, J.P. Magnetic Materials and Devices for the 21st Century: Stronger, Lighter, and More Energy Efficient. Advanced Materials. 2010.

[86] 3D Printing Rotors for Electric Motors. Additive Manufacturing Media. `https://www.youtube.com/watch?v=CuQqNzGQivE&t=1s`.

[87] Huray, P.G. Maxwell's Equations. John Wiley & Sons. 2009.

[88] How The Electric Motor Work ? Where the rotation come from ?. Amrie Muchta. 2021. `https://www.youtube.com/watch?v=IEghoxuFfZw`

[89] How Do All-Electric Cars Work?. Alternative Fuels Data Center. `https://afdc.energy.gov/vehicles/how-do-all-electric-cars-work`.

[90] Hub motor stator dan rotor 10kw. Bossgoo. `https://id.bossgoo.com/product-detail/hub-motor-stator-and-rotor-10kw-53807725.html`.

[91] Electric motors. Explain that stuff. `https://www.explainthatstuff.com/electricmotors.html`.

[92] ISO/ASTM 52907-2019. Additive manufacturing — Feedstock materials — Methods to characterize metallic powders.

[93] Nanakoudis, A. SEM: Types of Electrons and the Information They Provide. ThermoFisher Scientific. 2019.

[94] Williams, H. SEM for conductive and non-conductive specimens. Physics Education. 2021.

[95] Goldstein, J. Scanning Electron Microscopy and X-Ray Microanalysis. Springer. 2003.

[96] Olson, E. Particle Shape Factors And Their Use in Image Analysis – Part 1: Theory. Particle Technology Labs. 2011.

[97] Bodycomb, J. Image Analysis: Evaluating Particle Shape. HORIBA. 2011.

[98] McMillan, P. FIJI/Image J for Beginners, Fundamentals of Image Quantification. Melbourne University. 2011.

[99] Granular Material Flowmeter, GranuFlow *CREA* Particle Science. `https://creaparticlescience.com.au/agencies/granutools/granuflow/`.

[100] Boley, C.D.; Khairallah, S.A. and Rubenchik, A.M. Calculation of laser absorption by metal powders in additive manufacturing. Appl. Optics. 2015.

[101] Vlasea, M.L.; Lane, B.M.; Lopez, F.F.; Mekhontsev, S. and Donmez, M.A. Development of powder bed fusion additive manufacturing test bed for enhanced real time process control. In Proceedings of the International Solid Freeform Fabrication Symposium, Austin, TX, USA. 2015.

[102] Smithells, C.J. Metals Reference Book. Fifth edition. Butterworths: London and Boston. 1976.

[103] Carter, L.N.; Wang, X.; Read, N.; Khan, R.; Aristizabal, M.; Essa, K. and Attallah, M.M. Process optimisation of selective laser melting using energy density model for nickel based superalloys. Mater. Sci. Technol. 2016.

[104] Cheng, B. and Chou, K. Melt pool evolution study in selective laser melting. In Proceedings of the International Solid Freeform Fabrication Symposium, Austin, TX, USA. 2015.

[105] Gürtler, F.-J.; Karg, M.; Leitz, K.-H. and Schmidt, M. Simulation of laser beam melting of steel powders using the three-dimensional volume of fluid method. Phys. Proc. 2013.

[106] Li, L.; Lough, C.; Replogle, A.; Bristow, D.; Landers, R. and Kinzel, E. Thermal modeling of 304L stainless steel selective laser melting. In Proceedings of the ASME 2017 International Mechanical Engineering Congress and Exposition, Advanced Manufacturing, Tampa, FL, USA. 2017.

[107] Thompson, S.M.; Bian, L.; Shamsaei, N. and Yadollahi, A. An overview of Direct Laser Deposition for additive manufacturing; Part I: Transport phenomena, modeling and diagnostics. Addit. Manuf. 2015.

[108] Galba, M.J. and Reischle, M. Additive manufacturing of metals using powder-based technology. USA. 2016.

[109] Jopek, H. and Strek, T. Optimization of the effective thermal conductivity of a composite. In Convection and Conduction Heat Transfer. Philippines. 2011.

[110] Bauereiß, A.; Scharowsky, T. and Körner, C. Defect generation and propagation mechanism during additive manufacturing by selective beam melting. J. Mater. Process. Technol. 2014.

[111] Betz, H. T.; Olsen, O. H.; Schurin, B. D. and Morris, J. C. WADC-TR-56-222 (Part 2). 1957.

[112] Green, M. A. Self-consistent optical parameters of intrinsic silicon at 300 K including temperature coefficients. Solar Energy Materials and Solar Cells. 2008.

[113] Haines, M.P.; List, F.; Carver, K.; Leonard, D.N.; Plotkowski, A.; Fancher, C.M.; Dehoff, R.R. and Babu, S.S. Role of Scan Strategies and Heat Treatment on Grain Structure Evolution in Fe-Si Soft Magnetic Alloys made by Laser – Powder Bed Fusion. 2021.

[114] Kim, K.N.; Pan, L.M.; Lin, J.P.; Wang, Y.L.; Lin, Z. and Chen, G.L. The effect of boron content on the processing for Fe–6.5wt%Si electrical steel sheets. Journal of Magnetism and Magnetic Materials. 2004.

[115] Spierings, A.B.; Schneider, M. and Eggenberger, R. Comparison of density measurement techniques for additive manufactured metallic parts. Rapid Prototypes. 2011.

[116] Butler, D.L. Surface Roughness Measurement. Encyclopedia of Microfluidics and Nanofluidics. 2008.

[117] Roughness Meters. Measurement System Types and Characteristics. Keyence. `https://www.keyence.com/ss/products/measure-sys/measurement-selection/type/roughness.jsp`

[118] Degarmo, E.P.; Black, J. and Kohser, R.A. Materials and Processes in Manufacturing. Wiley. 2003.

[119] Whitehouse, D. Surfaces and their Measurement. Kogan Page Science Paper Edition. 2004.

[120] Wu, J. Chapter 5 - Material Interface of Pantograph and ContactLine. Pantograph and Contact Line System. 2018.

[121] Bradt, R.C. Ceramic Crystals and Polycrystals, Hardness of. Encyclopedia of Materials: Science and Technology. 2001.

[122] Ran, S.K. Gravity Probe B: Exploring Einstein's Universe with Gyroscopes. NASA. 2004.

[123] SWT Physics Department. Vibrating Sample Magnetometer. 2006.

[124] Srinivasan, K. L1(0) iron-platinum on nanocrystalline HITPERM soft magnetic underlayers for perpendicular recording media. 2004.

[125] Crabtree, G.W. Demagnetising fields in the de Haas-van Alphen effect. Argonne National Laboratory, Argonne, Illinois. 1977.

[126] Hysteresis Losses Causes & Calculations. Frenetic. `https://frenetic.ai/magnetic-notes/hysteresis-losses`.

[127] Bragg, W.H. and Bragg, W.L. The Reflexion of X-rays by Crystals. 1913.

[128] Koçak, A. Thin Film Preparation,Particle Size and Thickness Analysis. Materials Science and Engineering. 2018.

[129] Raudsepp, M. Recent advances in the electron-probe micro-analysis of minerals for the light elements. The Canadian Mineralogist. 1995.

[130] Tekumalla, S.; Selvarajou, B.; Raman, S.; Gao, S. and Seita, M. The role of the solidification structure on orientation-dependent hardness in stainless steel 316L produced by laser powder bed fusion. Materials Science and Engineering: A. 2022.

[131] Arshad, W.; Mehmood, A.; Hashmi, M.F. Rauf, O. The Effect of Increasing Silicon on Mechanical Properties of Ductile Iron. 2018.

A

Appendix A

Technical drawing designs, with all the dimension of the pieces build with the PBF-LB machine using the drawing software from *SolidWorks*. The cube, cube with thin walls, boundary piece and cylinder are presented the this appendix.

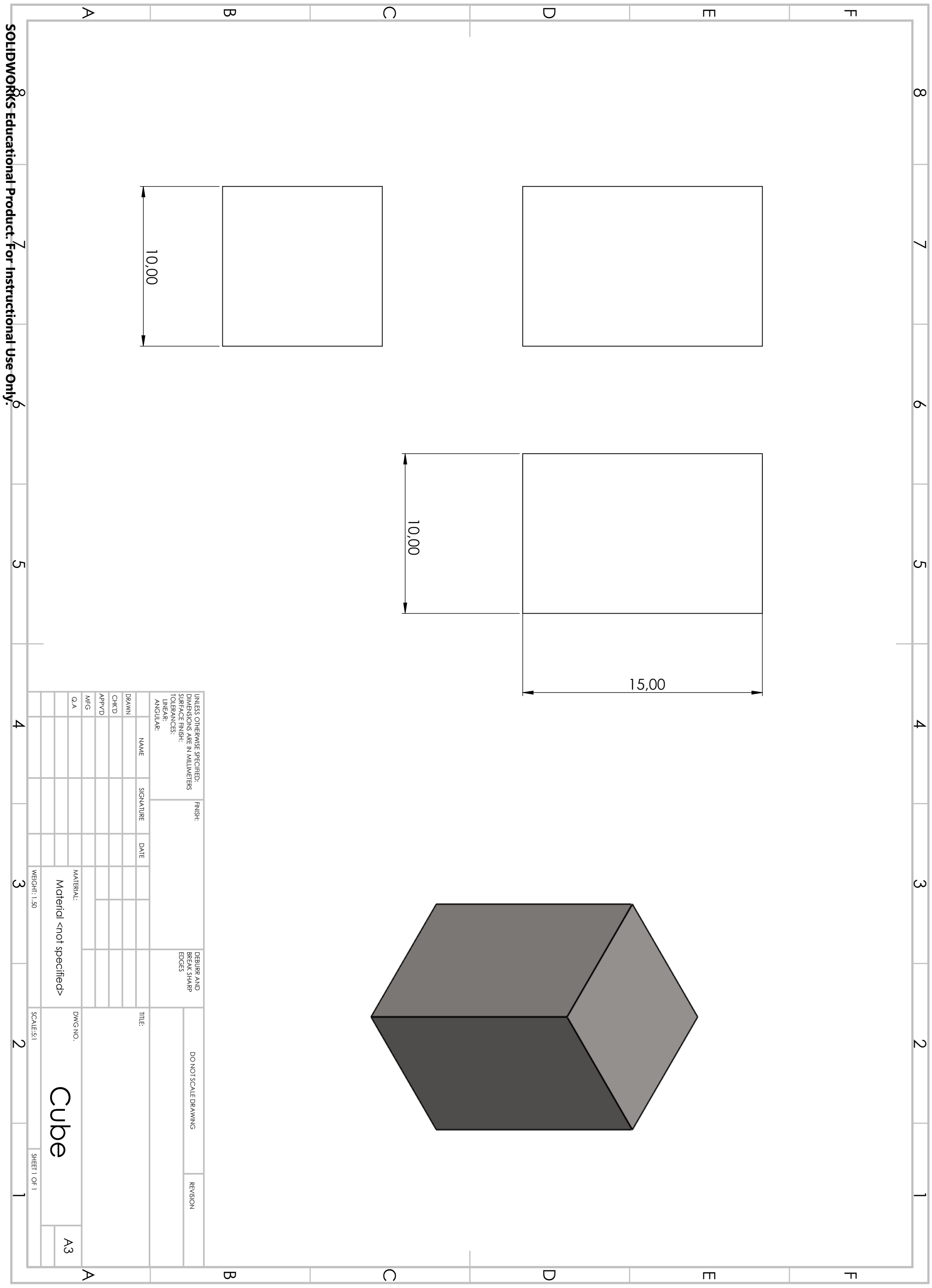

Figure A.1: Technical drawing design of the cube CAD designed *SolidWorks*.

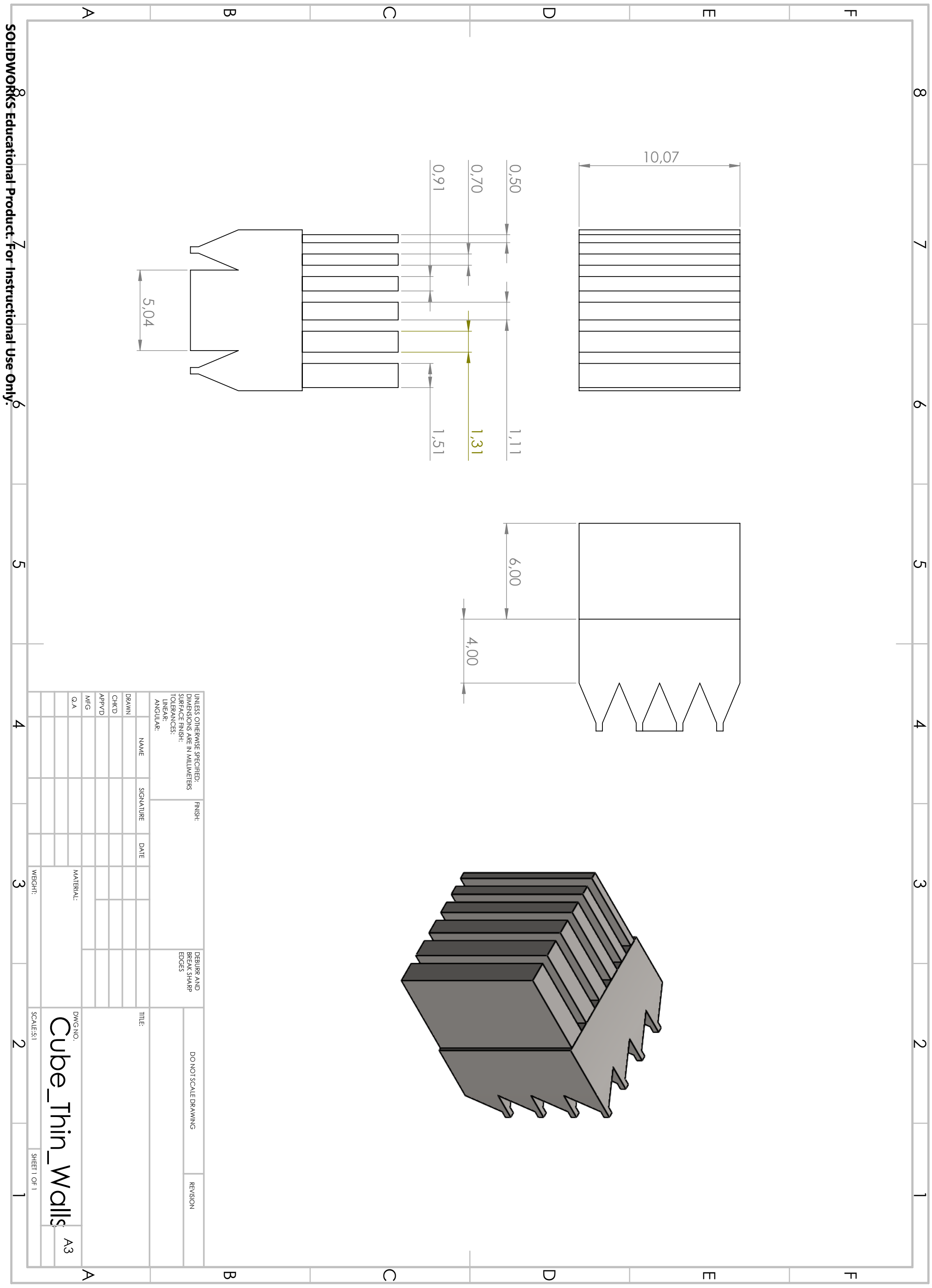

Figure A.2: Technical drawing design of the cube with thin walls CAD designed *SolidWorks*.

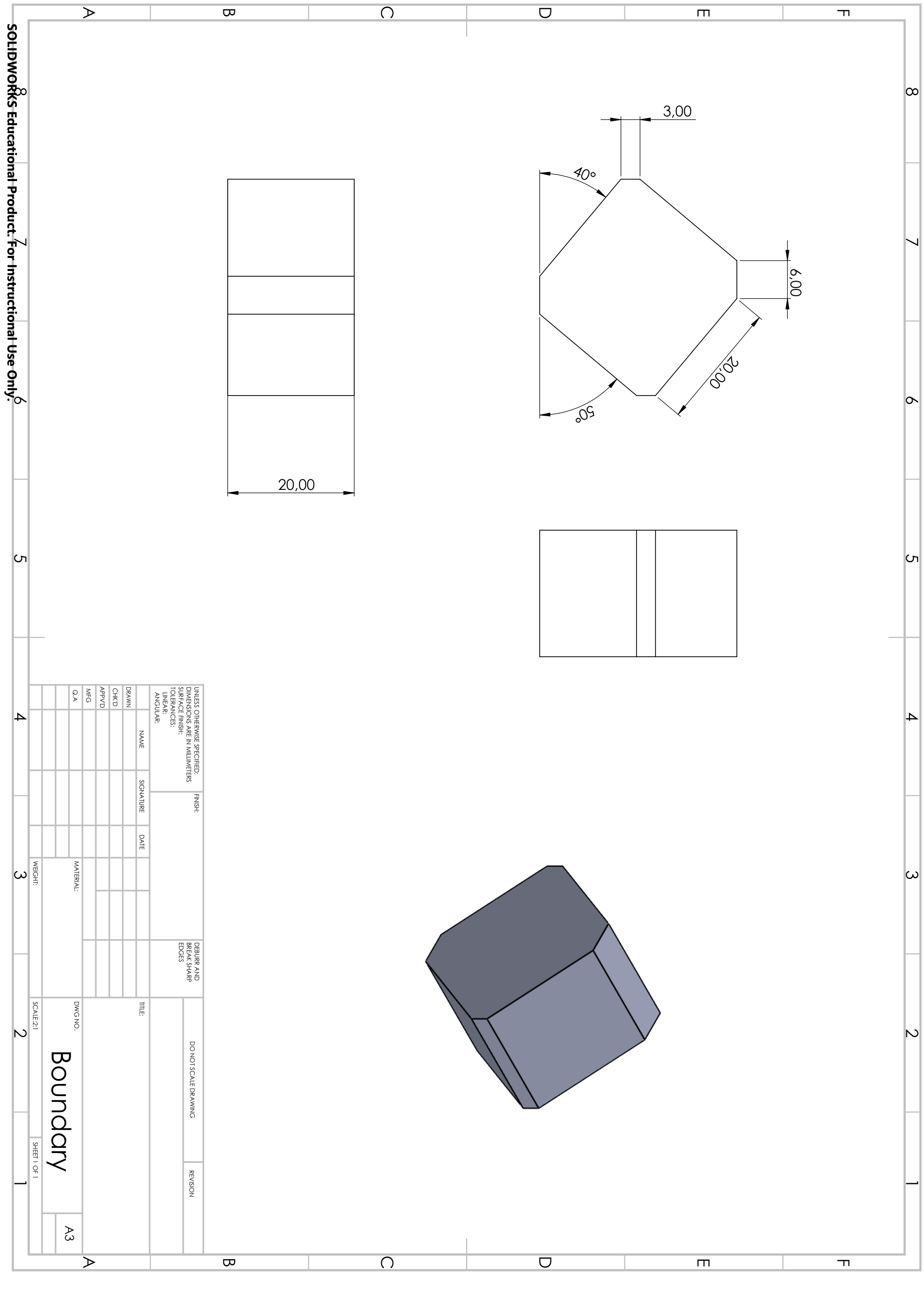

Figure A.3: Technical drawing design of the boundary piece CAD designed *SolidWorks*.

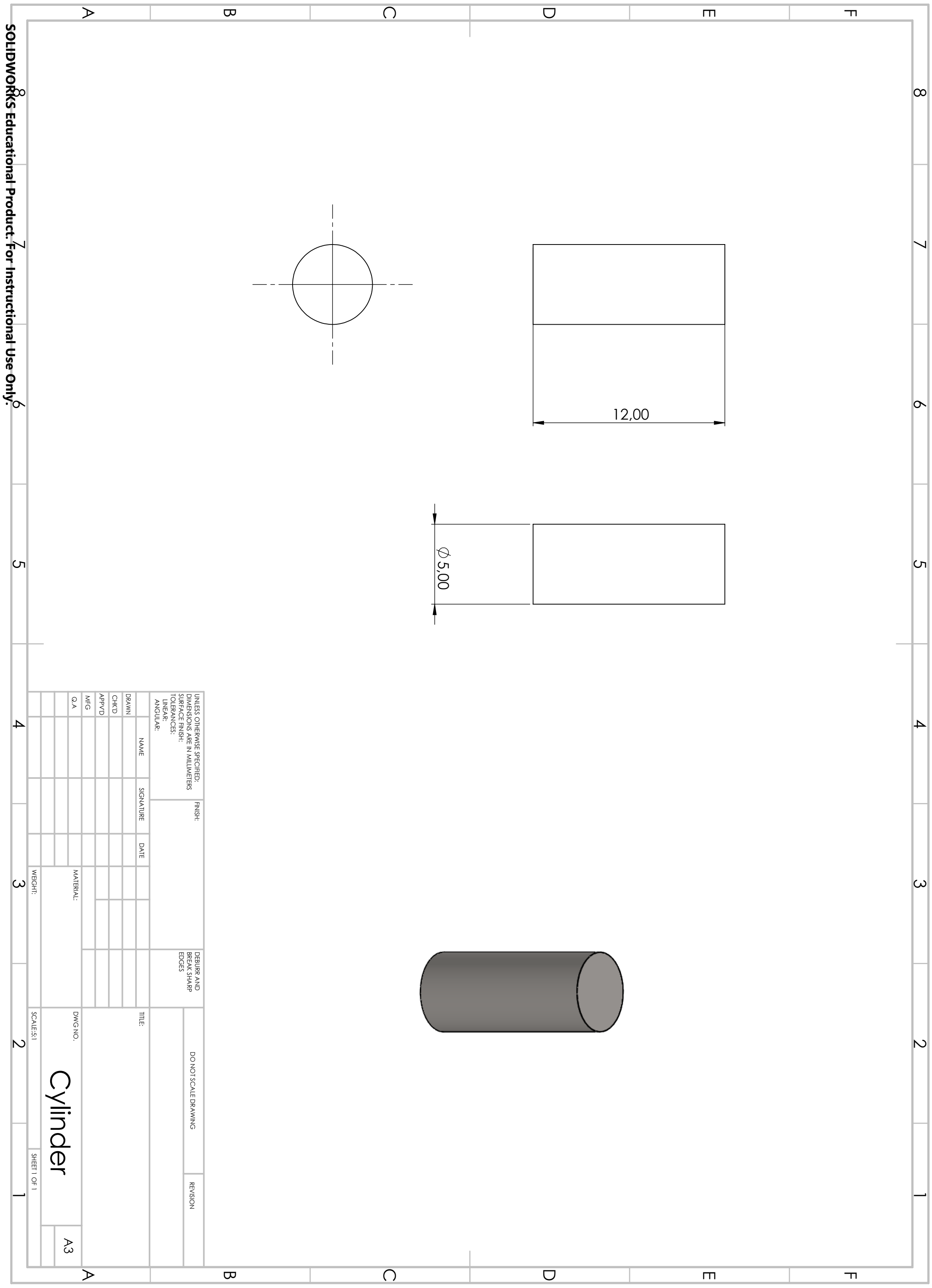

Figure A.4: Technical drawing design of the cylinder CAD designed *SolidWorks*.

B

Appendix B

Some more photos and images from the optical and SEM microscope, also with the EDS technology are shown in this appendix chapter, for the samples built of the both alloys used, Fe-3.5Si and Fe-6.5Si.

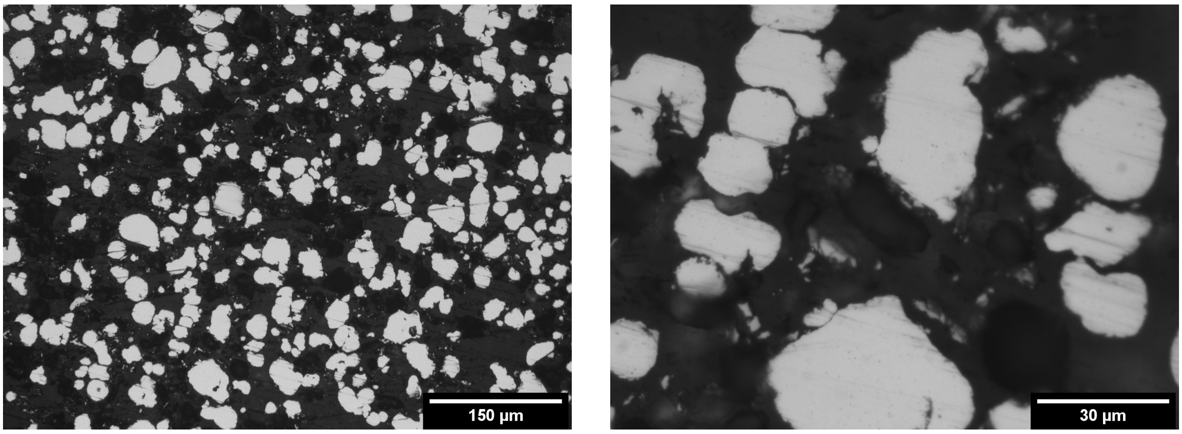

Figure B.1: Optical microscope images of the Fe-3.5Si powder, at different magnifications, 200× and 1000×, respectively, from left to right.

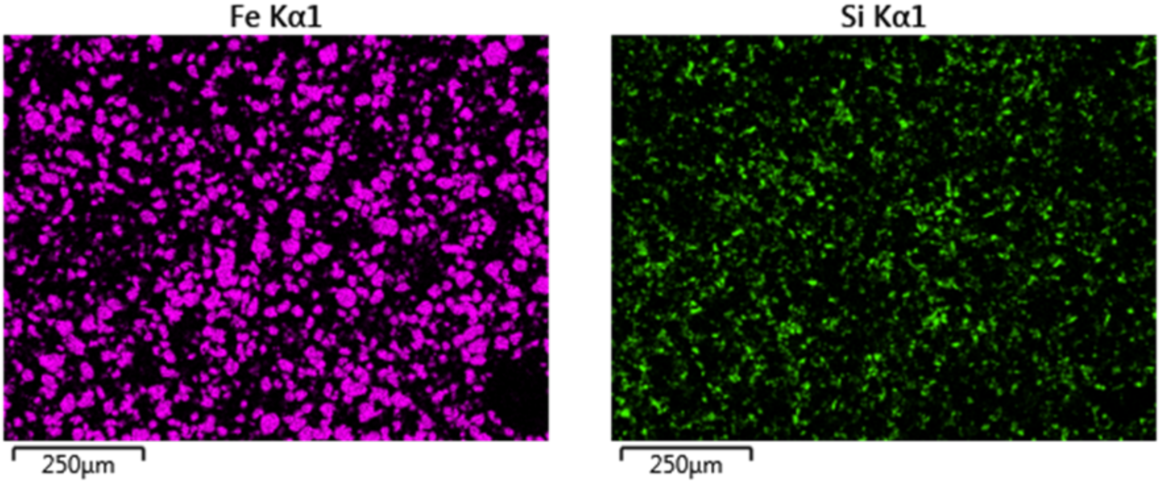

Figure B.2: EDS map of each element of the powder Fe-3.5Si mixture with the position of the iron **(Pink)** and silicon **(Green)**.

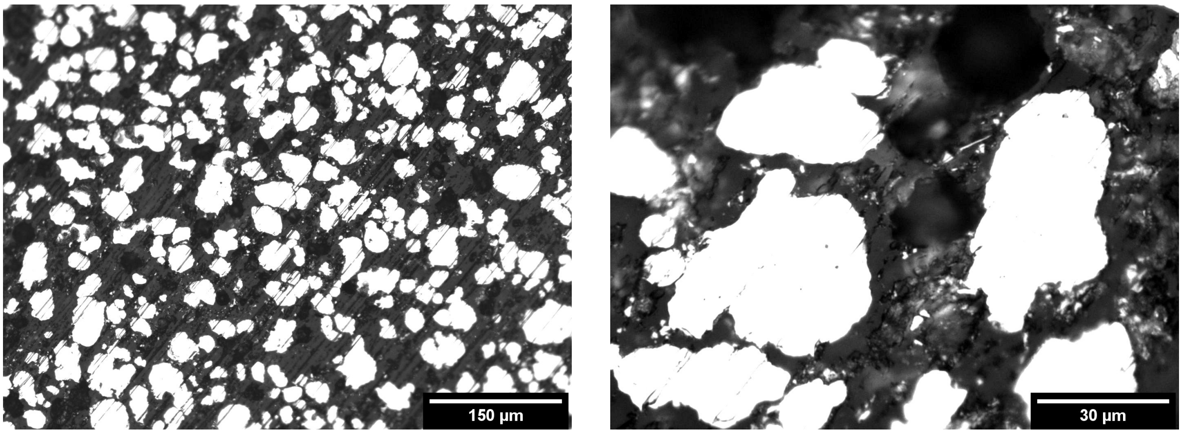

Figure B.3: Optical microscope images of the Fe-6.5Si powder mixture, at different magnifications, 200× and 1000×, respectively, from left to right.

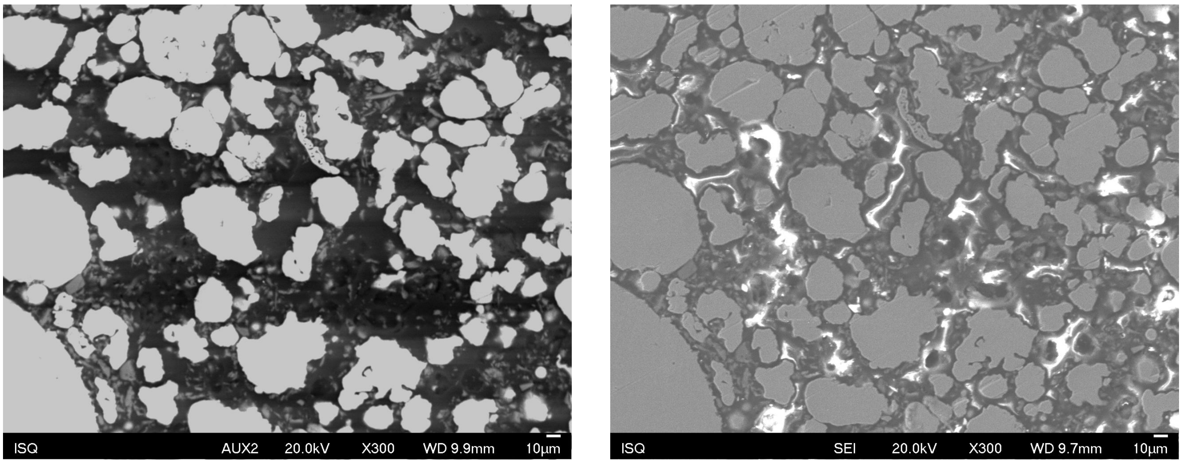

Figure B.4: SEM microscope BSE **(left)** and SE **(right)** image of the Fe-6.5Si powder mixture with 300× magnification.

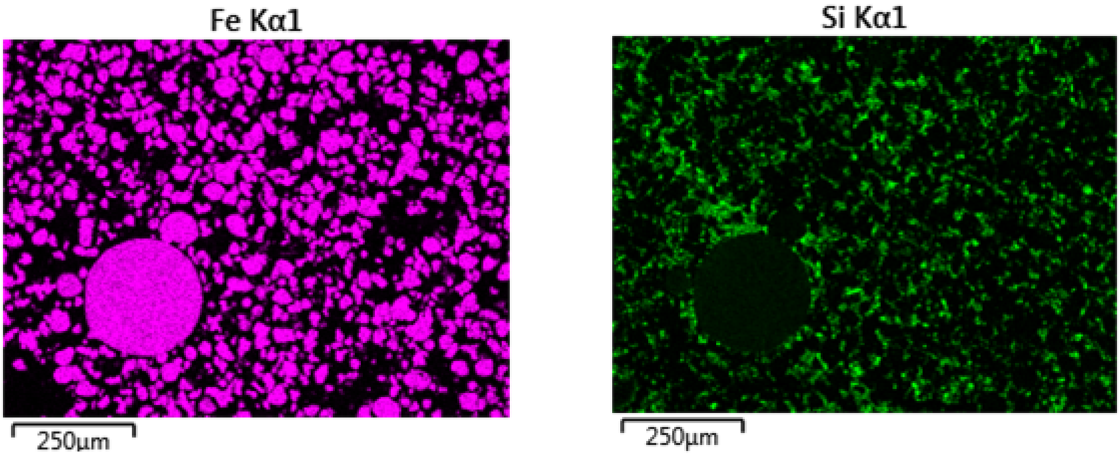

Figure B.5: EDS map of each element of the powder Fe-6.5Si mixture with the position of the iron **(Pink)** and silicon **(Green)**.

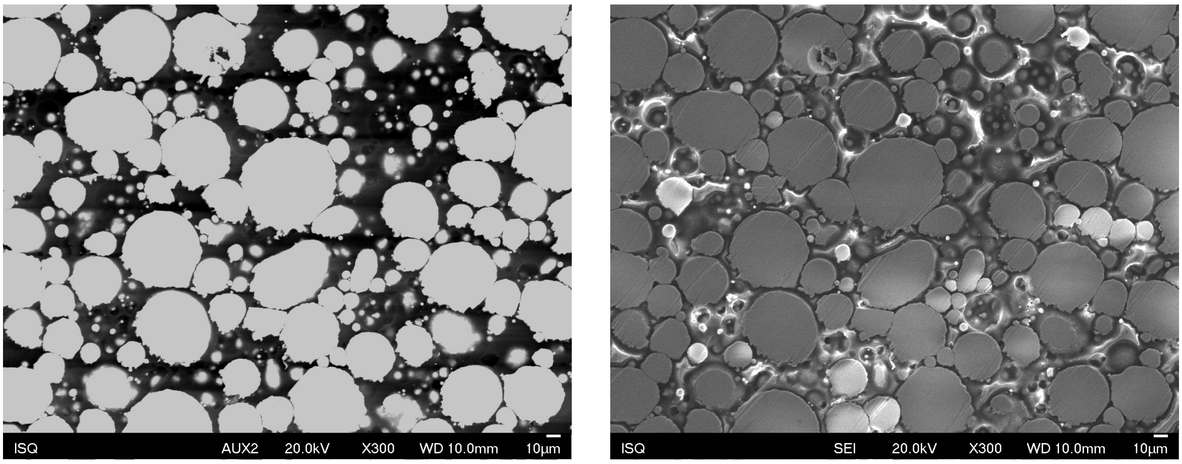

Figure B.6: SEM microscope BSE **(left)** and SE **(right)** image of the Fe-6.5Si m4p powder with 300× magnification.

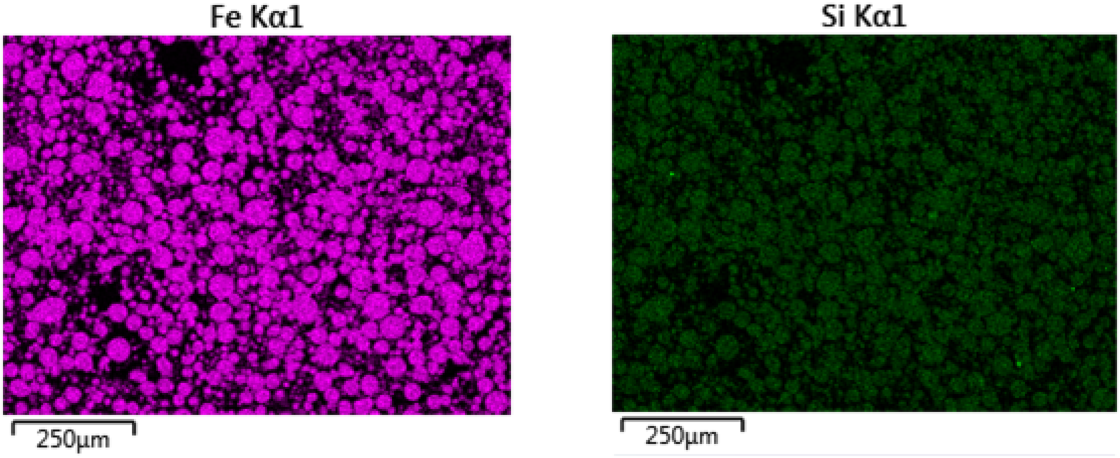

Figure B.7: EDS map of each element of the powder Fe-6.5Si m4p with the position of the iron **(Pink)** and silicon **(Green)**.

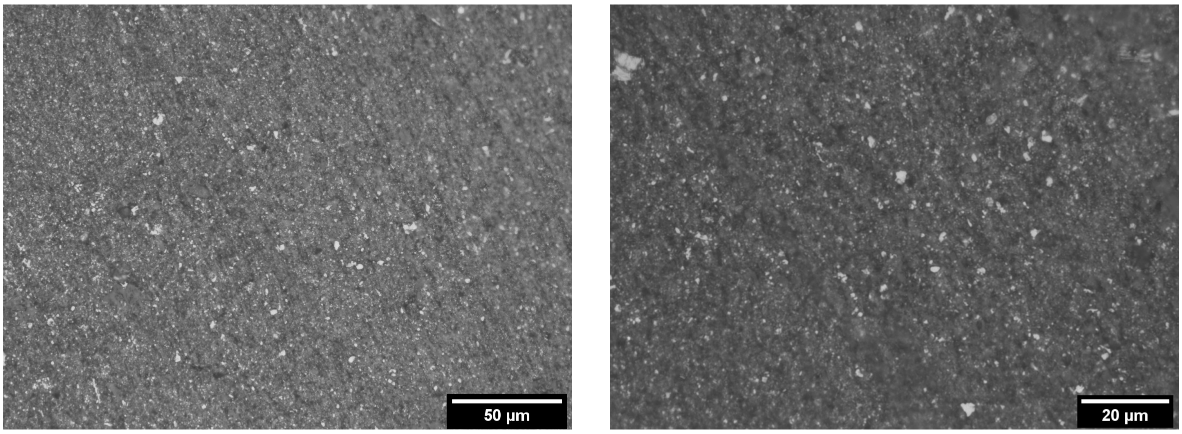

Figure B.8: Optical microscope images of the boron powder, at different magnifications, 500× and 1000×, respectively, from left to right.

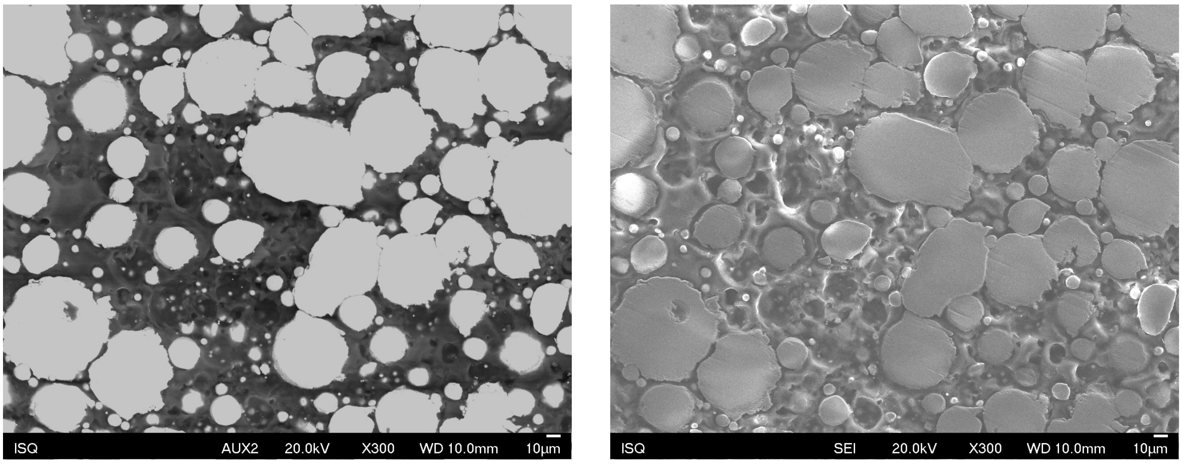

Figure B.9: SEM microscope BSE **(left)** and SE **(right)** image of the Fe-6.5Si m4p + 0.05B powder mixture with 300× magnification.

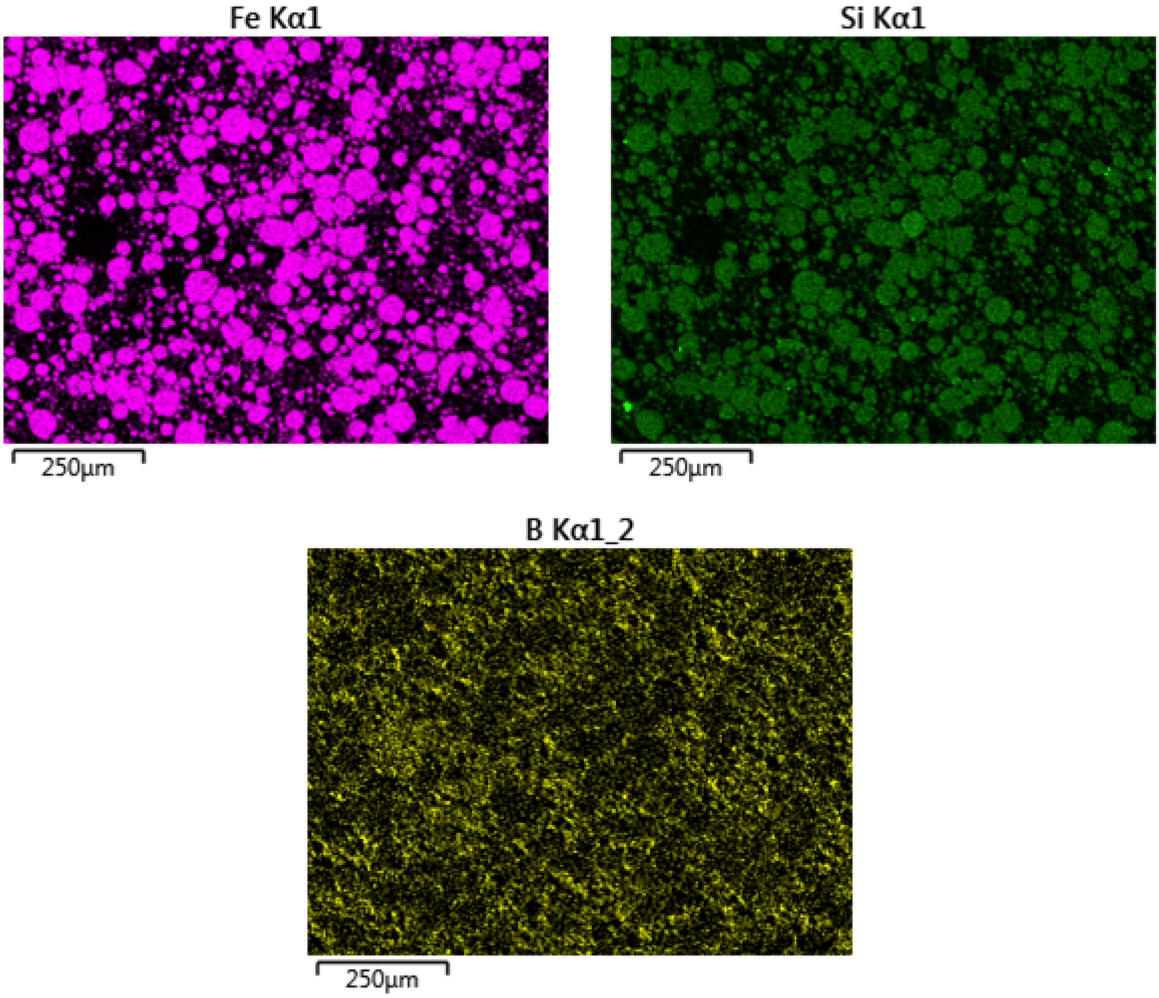

Figure B.10: EDS map of each element of the Fe-6.5Si m4p + 0.05B powder mixture with the position of the iron **(Pink)**, silicon **(Green)** and boron **(Yellow)**.

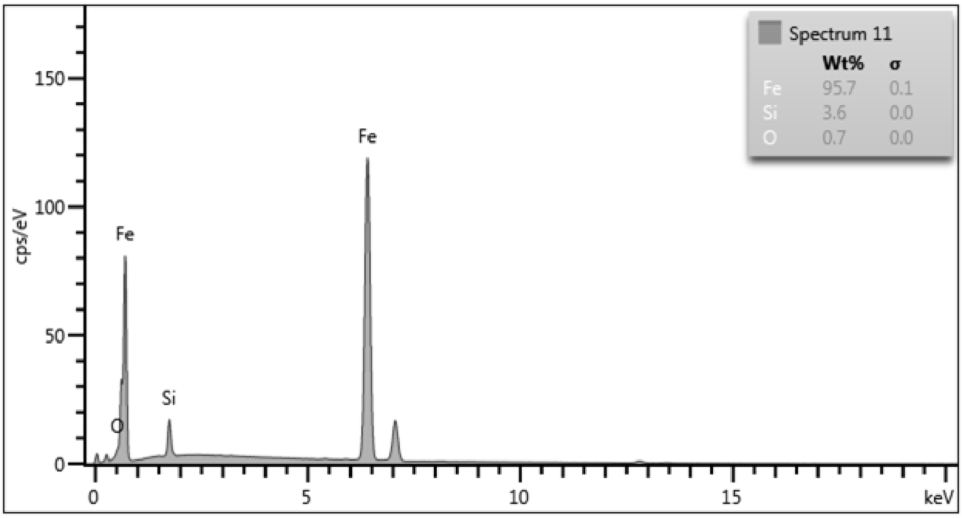

Figure B.11: EDS spectrum of the Fe-3.5Si M67 sample, with the percentages of each element considered.

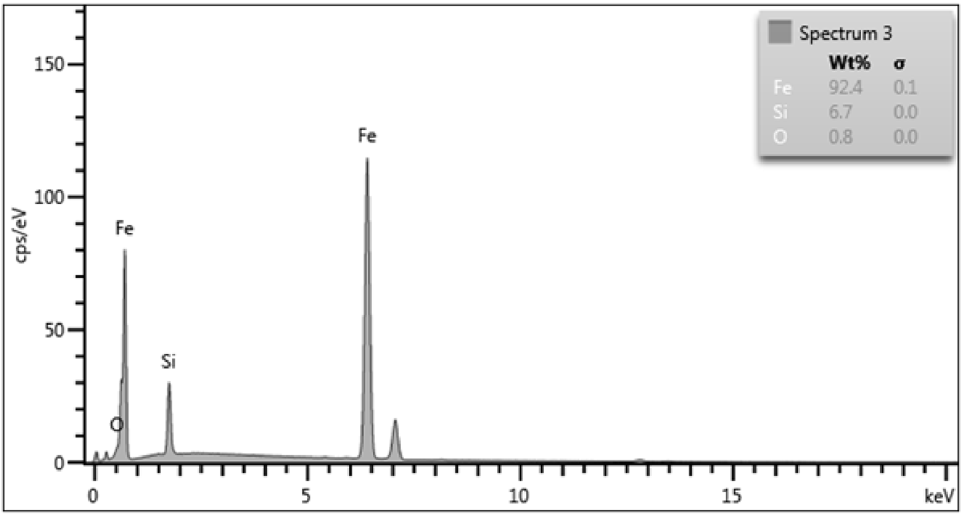

Figure B.12: EDS spectrum of the Fe-6.5Si M67 mix sample, with the percentages of each element considered.

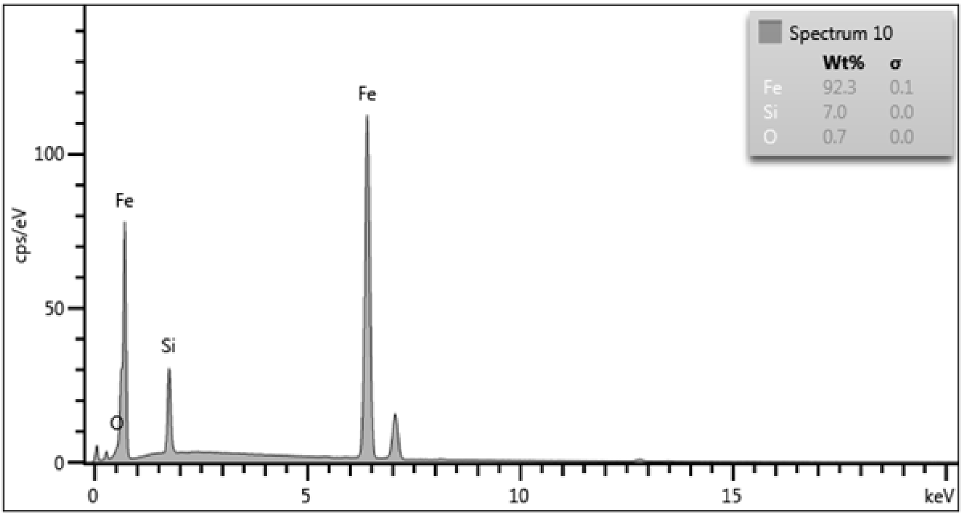

Figure B.13: EDS spectrum of the Fe-6.5Si M67 m4p sample, with the percentages of each element considered.

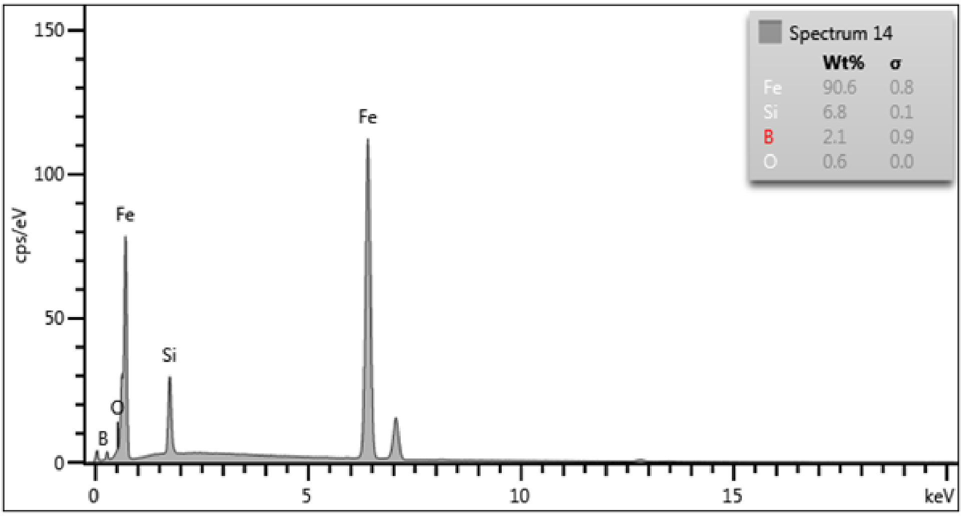

Figure B.14: EDS spectrum of the Fe-3.5Si M67 sample, with the percentages of each element considered.

C

Appendix C

Some extra figures of equipments and products used during the work that were not possible to place in the text.

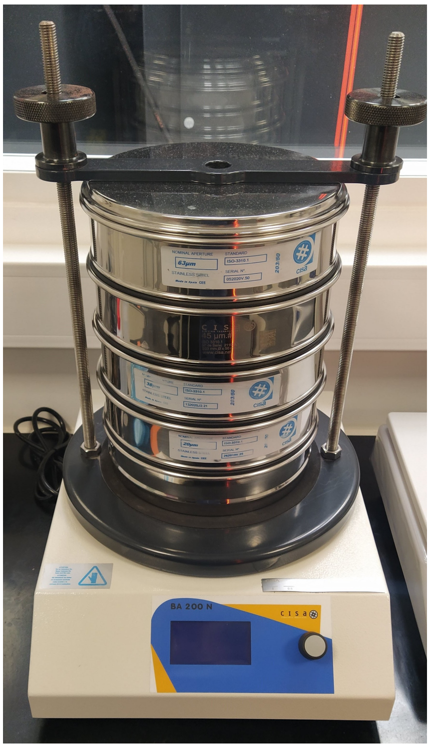

Figure C.1: Sieve shaker *CISA Cedaceria Industrial 200 N Compact* with the sieves selected for the procedure (63, 45, 38 and 20 μm of grid aperture).

Figure C.2: Vacuum oven *Thermo Scientific Vacutherm Vacuum Oven VT 6060 M.*

Figure C.3: Equipment used for making epoxy samples. The three liquids observed are the *Buehler* Epoxy Resin, Epoxy Hardener, and Epoxy Release Agent, respectively from the bigger to the smaller recipient. At the right is shown the balance used to weight the liquids in the right proportions. In blue are shown the cups to fill with the epoxy mixture.

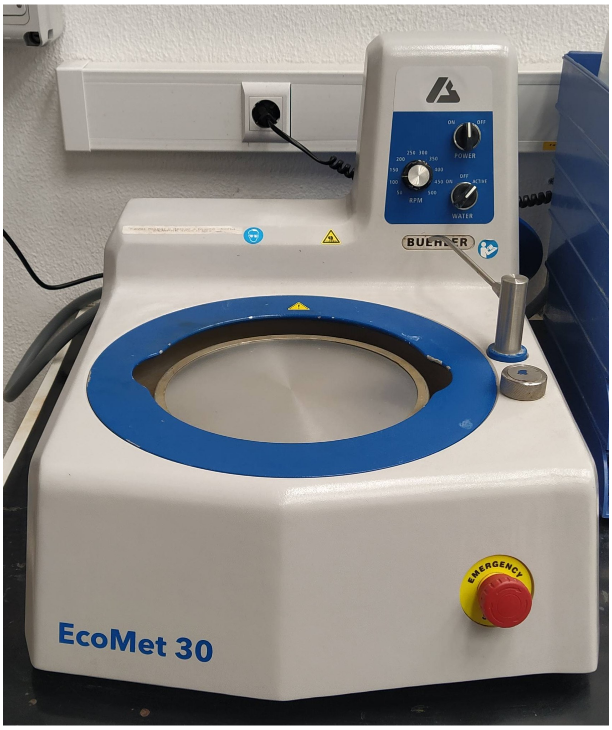

Figure C.4: Rotating polisher *Buehler EcoMet 30*.

Figure C.5: *MetaDi Supreme Crystalline Diamond Suspension* for 6 and 1 μm mats **(left)** and *MasterMet Colloidal Silica Polishing Suspension* **(right)**, both from *Buehler*.

Figure C.6: Setup with optical microscope *ZEISS Axiotech 100* and detail from the analysis area with a mounted sample being observed.

Figure C.7: Chamber furnace LH 30/14 from *Nabertherm*. Could heat up to 1400°C.

Figure C.8: Injector blast cabinet *Normfinish DI12* using glass beads.

Figure C.9: Balance used for density measurements, *Kern ABS 220-4N* **(a)**, mass measurement of one sample in air **(b)** and inside water **(c)**, using the same balance.

Figure C.10: SEM microscope *JEOL JSM-6500F* and detail from the EDS *Oxford Instruments X-Max*^{N}.

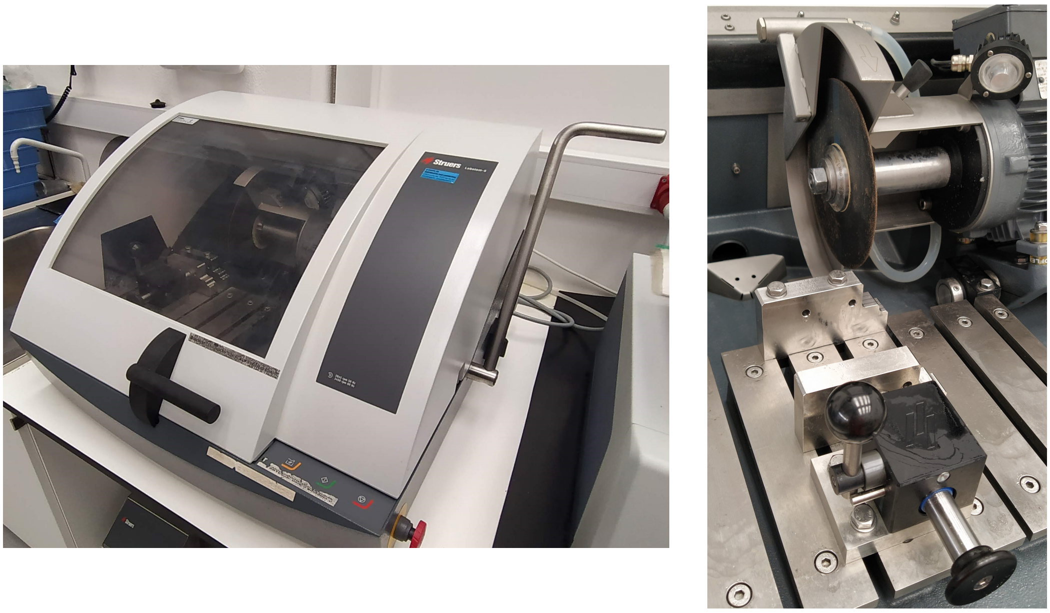

Figure C.11: *Struers Labotom-5* cutting machine and detail from the disk and sample holder.

Figure C.12: Mounting machine *SimpliMetTM 4000 Compression Mounting System* from *Buehler*.

Figure C.13: *Mitutoyo SJ-210* portable surface roughness tester and detail from the cantilever of the machine doing a calibration process.

Figure C.14: Hardness measuring machine *EMCOTEST DuraScan 70 G5*. Possible to measure Hardness Vickers and Brinell.

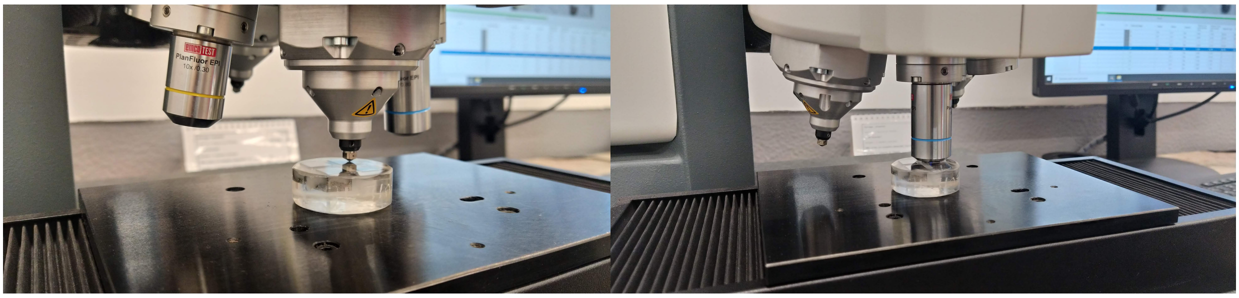

Figure C.15: *EMCOTEST DuraScan 70 G5* indentation with HV **(left)** and optical microscope **(right)**.